Ultrathin Films of Tin Halide Perovskite on Gold Single Crystals

DISSERTATION

zur Erlangung des Grades eines Doktors

der Naturwissenschaften

vorgelegt von

Madad Abbasli

eingereicht bei der Naturwissenschaftlich-Technischen Fakultät

der Universität Siegen

Siegen 2025

Erster Gutachter:
Prof. Dr. Carsten Busse
Universität Siegen

Zweiter Gutachter:
Prof. Alex Redinger
University of Luxembourg

Tag der mündlichen Prüfung:
10.04.2025

Abstract

This thesis investigates the growth, structural characteristics, and stability of ultrathin films of the lead-free perovskite $CsSnBr_3$ (cesium tin bromide) on Au(111) and Au(100) substrates under ultra-high vacuum (UHV) conditions. Motivated by the need for environmentally friendly alternatives to lead-based perovskites in optoelectronic applications, this work employs a combination of scanning tunneling microscopy (STM), low-energy electron diffraction (LEED), and X-ray photoelectron spectroscopy (XPS) to explore the fundamental properties of $CsSnBr_3$ films.

The study examines the behavior of precursor molecules, CsBr and $SnBr_2$, on both gold surfaces, revealing distinct growth patterns and the influence of substrate symmetry on adsorption and subsequent film formation. Co-deposition of these precursors leads to the formation of $CsSnBr_3$ films, the structure of which is analyzed in detail. A tetramer phase on the (001) surface of $CsSnBr_3$ is confirmed through atomically resolved STM imaging and supported by density functional theory (DFT) calculations. Furthermore, XPS analysis provides insights into the chemical composition of the films and elucidates the degradation mechanisms upon exposure to air, highlighting the critical role of Sn^{4+} formation in the degradation process.

The findings demonstrate that UHV-grown $CsSnBr_3$ films initially exhibit a favorable Sn^{2+} oxidation state but degrade rapidly to include Sn^{4+} states upon air exposure, underscoring the importance of encapsulation for maintaining stability. This research advances the understanding of lead-free perovskite film growth and stability while offering valuable insights for the development of stable, efficient, and environmentally friendly optoelectronic devices.

Zusammenfassung

Diese Arbeit untersucht das Wachstum, die strukturellen Eigenschaften und die Stabilität ultradünner Schichten des bleifreien Perowskits $CsSnBr_3$ (Cäsium-Zinn-Bromid) auf Au(111)- und Au(100)-Substraten unter Ultrahochvakuum (UHV)-Bedingungen. Motiviert durch den Bedarf an umweltfreundlichen Alternativen zu bleibasierten Perowskiten in optoelektronischen Anwendungen, kombiniert diese Arbeit Rastertunnelmikroskopie (STM), Niederenergie - Elektronenbeugung (LEED) und Röntgenphotoelektronenspektroskopie (XPS), um die grundlegenden Eigenschaften von $CsSnBr_3$-Filmen zu erforschen.

Die Studie beginnt mit der Untersuchung des Verhaltens der Vorläufermoleküle CsBr und $SnBr_2$ auf beiden Goldoberflächen und zeigt unterschiedliche Wachstumsmuster sowie den Einfluss der Substratsymmetrie auf deren Adsorption und anschließende Filmbildung. Die Co-Deposition dieser Moleküle führt zur Bildung von $CsSnBr_3$-Filmen, deren Struktur im Detail analysiert wird. Insbesondere wird die Bildung einer Tetramerphase auf der (001)-Oberfläche von $CsSnBr_3$ durch atomar aufgelöste STM-Aufnahmen bestätigt und durch Dichtefunktionaltheorie (DFT)-Berechnungen gestützt. Darüber hinaus liefert die XPS-Analyse Einblicke in die chemische Zusammensetzung der Filme und klärt die Abbaumechanismen bei Luftkontakt auf, wobei die entscheidende Rolle der Sn^{4+}-Bildung im Abbauprozess hervorgehoben wird.

Die Ergebnisse zeigen, dass UHV-gewachsene $CsSnBr_3$-Filme anfänglich einen günstigen Sn^{2+}-Oxidationszustand aufweisen, aber bei Luftkontakt schnell zu Sn^{4+}-Zuständen abgebaut werden, was die Bedeutung der Verkapselung zur Aufrechterhaltung der Stabilität unterstreicht. Diese Forschung trägt nicht nur zum Verständnis des Wachstums und der Stabilität bleifreier Perowskitfilme bei, sondern liefert auch wertvolle Erkenntnisse für die Entwicklung stabiler, effizienter und umweltfreundlicher optoelektronischer Bauelemente.

Contents

1 Introduction **6**

2 Background **10**
2.1 Metal halide perovskites 10
2.1.1 Shockley–Queisser limit 11
2.2 STM (Scanning Tunneling Microscopy) 14
2.3 LEED (Low-Energy Electron Diffraction) 18
2.4 XPS (X-ray Photoelectron Spectroscopy) 20
2.5 DFT (Density functional theory) 22

3 Experimental Setup **25**
3.1 VT-STM (Variable Temperature - Scanning Tunneling Microscope) 25
3.2 X-ray Photoelectron Spectrometer 26
3.3 Preparation of single crystals 28
3.4 MBE (Molecular beam epitaxy) 29

4 CsBr on gold surfaces **31**
4.1 CsBr on Au(111) 31
4.2 CsBr on Au(100) 34

5 $SnBr_2$ on gold surfaces **37**
5.1 $SnBr_2$ on Au(111) 37
5.2 $SnBr_2$ on Au(100) 43

6 $CsSnBr_3$ on Au(111) **46**
6.1 Submonolayer coverage and more 46
6.2 Few monolayer coverage 54

7 $CsSnBr_3$ on Au(100) **62**
7.1 Submonolayer coverage 62
7.2 Few monolayer coverage 66
7.2.1 Sequential deposition 66
7.2.2 Codeposition 71

8 XPS measurement of the precursor molecules and tin halide perovskite samples **74**
8.1 Precursors 74
8.1.1 CsBr on Au(111) 74
8.1.2 $SnBr_2$ on Au(111) 77
8.2 Perovskite samples 80
8.2.1 $CsSnBr_3$ on Au(100) 80
8.2.2 $CsSnBr_3$ on Au(111) 86
8.2.3 $CsSnBr_3$ on Au(111) with excess of CsBr 91
8.2.4 $CsSnBr_3$ on Au(111) with excess of $SnBr_2$ 96
8.3 Summary of the XPS results 101

9 Conclusion and outlook **106**

Bibliography **108**

Chapter 1

Introduction

Perovskites were first discovered in 1839 by Gustav Rose, who identified the mineral calcium titanate (Figure 1.1 a), later named after the Russian mineralogist Lev Perovski. Over time the name perovskite has been extended to describe a broad family of materials that share the same crystal structure as the mineral. The perovskite structure would later play a crucial role in the development of advanced materials and renewable energy technologies. This structure is characterized by the general formula ABX_3, where A and B represent cations of differing sizes, and X is an anion, typically oxygen or a halide. These materials exhibit a wide range of interesting physical and chemical properties, making them important in various fields such as photovoltaics, catalysis, and electronics.

The burning of fossil fuels for energy is the largest contributor to global greenhouse gas emissions, driving climate change and environmental degradation. Transitioning to renewable energy sources like solar power is critical to meet global carbon reduction targets, such as those outlined in the Paris Agreement. Solar cells harness an abundant and inexhaustible resource—sunlight—making them one of the most sustainable energy solutions available [1].

A solar cell is a device designed to absorb photons from sunlight, leading to the generation of free electron–hole pairs. These pairs are extracted and driven through an external load that maintains a positive voltage, resulting in the delivery of electrical power to an external circuit. This is achieved solely through the absorption of photons, without causing any other changes to the device. The process of converting light into electricity is known as the photovoltaic effect, which is discussed in detail in [2]. When radiation interacts with the electron–hole system within the semiconductor light absorber, energy is transferred from the incident photons to the electron–hole gas. This energy transfer modifies the Fermi levels, enabling the system to perform useful work on an external circuit. Conversely, the electron–hole system can also lose energy by emitting photons outward [2].

Solar cells can provide energy to regions without access to centralized power grids, especially in remote or underdeveloped areas. They promote energy independence and resilience, reducing reliance on imported fossil fuels and making energy accessible to billions of people worldwide.

Interestingly, the breakthrough that eventually led to the development of perovskite solar cells came somewhat by accident. In 2009, researchers working on dye-sensitized solar cells

experimented with lead halide perovskites (specifically $CH_3NH_3PbI_3$ and $CH_3NH_3PbBr_3$) as sensitizers [3]. To their surprise, they discovered that these materials performed unexpectedly well, as light-absorbing layers, capable of converting sunlight into electricity.

One of the key advantages of metal halide perovskites is their compositional flexibility. The A-site cation can be organic or inorganic, such as methylammonium (MA), formamidinium (FA), or cesium (Cs). The B-site cation is typically a divalent metal like lead (Pb) or tin (Sn), while the X-site anion is a halide such as iodine (I), bromine (Br), or chlorine (Cl). This vast compositional space allows for fine-tuning of the perovskite's properties, including its bandgap, which is crucial for maximizing light absorption and, consequently, the power conversion efficiency (PCE) of solar cells.

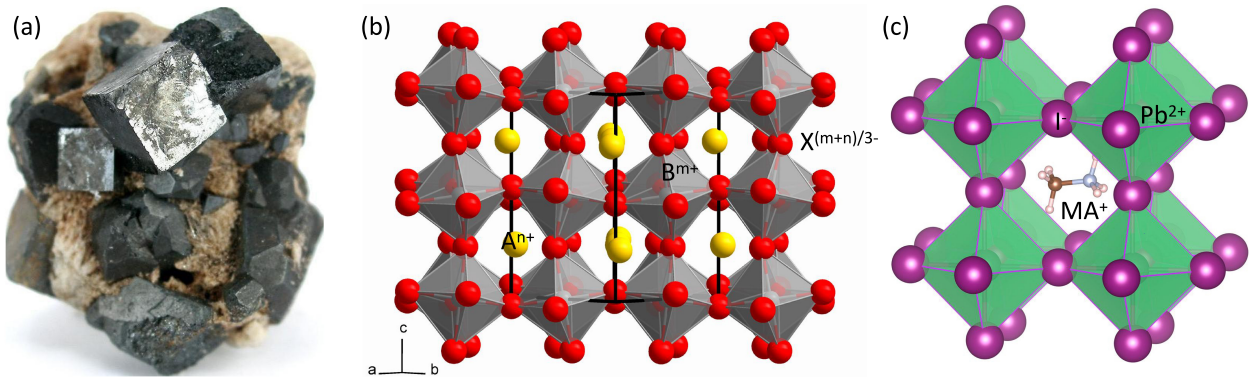


Figure 1.1: (a) First ever discovered perovskite - $CaTiO_3$ [4]. (b) Typical ABX_3 perovskite [5]. (c) Organic-inorganic perovskite - $CH_3NH_3PbBr_3$ [6].

As seen in Figure 1.1, the perovskite structure can vary from oxides like $CaTiO_3$ to the organic-inorganic halide perovskites that are relevant to this work. The adaptability of the ABX_3 framework enables a wide range of chemical compositions and functionalities, making perovskites a versatile material in research.

The main challenge is the toxicity of lead, a common B-site cation in high-performance perovskite solar cells. The use of lead raises environmental and health concerns, thus necessitating the development of lead-free alternatives that can match or exceed the performance of lead-based counterparts.

To overcome these challenges, various strategies have been explored, including compositional engineering, interface modification, and encapsulation techniques. Compositional engineering involves substituting lead with alternative B-site cations, such as tin (Sn), germanium (Ge), or bismuth (Bi). However, lead-free perovskites typically suffer from lower PCEs and stability issues compared to lead-based counterparts.

Despite their promise, perovskites face challenges such as stability under environmental conditions (moisture, heat, and ultraviolet (UV) light) and scalability for commercial production. Addressing these issues is an active area of research.

Beyond solar cells, perovskites have diverse applications due to their versatile properties. They can be used in highly efficient and tunable LEDs for lighting and displays. Their excellent light absorption makes them suitable for detecting light in cameras and optical

communication devices. Some perovskite materials are being studied for their catalytic activity and ability to sense gases. Integration of perovskites with batteries or supercapacitors is also being explored to develop hybrid energy systems.

Given the urgent need for sustainable energy solutions and the rapid advancement of perovskite-based technologies, their development could revolutionize not just solar power but also other optoelectronic applications. This aligns with the global goal of achieving a sustainable future and mitigating climate change [7].

In this thesis, the fascinating world of metal halide perovskites is studied, with a focus on the growth, characterization, and stability of ultrathin films of $CsSnBr_3$ prepared under ultra-high vacuum (UHV) conditions. A multi-faceted approach is employed, combining advanced microscopy techniques, such as scanning tunneling microscopy (STM) and low-energy electron diffraction (LEED), with chemical analysis using X-ray photoelectron spectroscopy (XPS).

The atomic-scale structure and properties of $CsSnBr_3$ perovskite films grown on two distinct gold substrates, Au(111) and Au(100), are investigated. The influence of substrate symmetry on film formation is analyzed to gain a deeper understanding of the growth mechanisms and the resulting film morphology.

Furthermore, XPS is utilized to probe the chemical composition of the $CsSnBr_3$ films and to monitor their degradation upon exposure to air. Through this analysis, the chemical species formed during degradation are identified, and the underlying degradation mechanisms are elucidated. By understanding these degradation pathways, effective strategies to mitigate these processes and enhance the air stability of tin perovskite films can be developed.

In this thesis, several key aspects of metal halide perovskites, particularly $CsSnBr_3$, grown on gold substrates under ultra-high vacuum conditions, are explored. Below is a brief outline of what each chapter covers:

Chapter 2 explains the background, exploring metal halide perovskites structure, particularly focusing on tin-based alternatives to lead. It also discusses the ongoing challenges of stabilizing Sn^{2+} and introduces the Shockley-Queisser limit as a theoretical benchmark for solar cell efficiency. Additionally, Chapter 2 describes the principles behind STM, LEED and XPS as characterization methods, along with DFT as a method for ground state energy calculations.

Chapter 3 describes the experimental setup, detailing the variable temperature - scanning tunneling microscope (VT-STM) system with its two UHV chambers and quartz crystal microbalance (QCM), as well as the UHV suitcase used for sample transport between preparation and measurement. It also outlines the methods for preparing gold substrates, and the use of an evaporator for molecular beam epitaxy (MBE).

Chapter 4 investigates CsBr growth on gold surfaces. On Au(111), a square structure is observed corresponding to rock-salt CsBr, which modifies the herringbone reconstruction into a stripe pattern underneath the film. For CsBr on Au(100), a square pattern originating from the (001) face of CsBr is also observed, however modulated by a superstructure with larger unit cell.

Chapter 5 describes the deposition of $SnBr_2$ on Au(111) and Au(100). On Au(111), the surface reconstruction is lifted, with differing morphologies observed depending on the deposition duration. On Au(100), $SnBr_2$ also caused lifting of the surface reconstruction and an overall disordered appearance with local order is observed.

Chapter 6 reveals that instead of $CsSnBr_3$ co-deposition of CsBr and $SnBr_2$ resulted in structures such as flower, stripes, honeycomb, ladder, and square. Chapter 5 further explains few monolayer depositions resulting in a $CsSnBr_3$ thin film with a similar symmetry to the substrate. Atomic-resolved images revealed the presence of Br anions, confirmed by DFT calculations, as well as surface defects.

Chapter 7 explains the snythesis and characterization of $CsSnBr_3$ ultrathin films on Au(100). Further, submonolayer structures are examined and sequential deposition is explored showing atomic mobility.

Chapter 8 details the XPS results for the precursor molecules CsBr and $SnBr_2$ as well as the ultrathin $CsSnBr_3$ films on Au(100) and Au(111). Further, the influence of air on the perovskite, especially the Sn oxidation state, is investigated. Perovskite samples showed oxidation of Sn^{2+} to Sn^{4+} upon air exposure, with Sn^0 vanishing, reduced amounts of Cs and Br after air exposure.

Chapter 9 concludes the study, summarizing the key findings about lead-free perovskites, substrate symmetry, and material stability, as well as future research, such as encapsulation and compositional engineering for improved perovskite devices.

Chapter 2

Background

2.1 Metal halide perovskites

Metal halide perovskites have emerged as a highly promising class of materials with diverse applications [8]. This is due to their tunable properties [9] and high efficiency at converting sunlight into electricity [10]. Additionally, perovskites for photovoltaic (PV) applications have a low energy consumption during production and are expected to be cost-competitive compared to current PV technologies [11], making them a promising material for renewable energy technology. Metal halide perovskites possess the ABX_3 formula, where A represents an organic or alkali metal cation (i.e., $CH_3NH_3^+$, Cs^+), B represents a metal cation (i.e., Pb^{2+}, Sn^{2+}), and X represents a halide anion (i.e., I^-, Br^-, Cl^-).

Currently, the record power conversion efficiency of single junction perovskite solar cells lies at 26.1% [12], which is achieved with a perovskite containing only lead (Pb) at the B-site. Theoretically, Sn-containing perovskites should be able to reach a higher power conversion efficiency than any lead-containing perovskite, as their band gap lies at the maximum of the Shockley-Queisser limit [13]. Using Sn instead of Pb is further recommended due to environmental concerns with respect to the toxicity of lead [14]. However, the record power efficiency of Sn-based halide perovskites is at the moment only close to 15% [15]. The main challenge is the stabilization of the Sn^{2+} state enabling the desired perovskite structure. Sn^{2+} has a lower energy threshold to undergo oxidation than Pb^{2+} [16, 17]. Tin oxidation (i.e., $Sn^{2+} \rightarrow Sn^{4+} + 2e^-$) in tin perovskites is associated with the degradation of the material that can lead to unfavorable *p*-type doping, vacancies, non-stoichiometry, and chemical decomposition [18]. When tin is oxidized, the degradation process can continue in a cyclic fashion [19]. Thereby, intrinsic and extrinsic factors such as oxygen, water, solvents, superoxide, and light could chemically transform the perovskite [20]. Therefore, controlling the oxidation state of tin-based perovskite is the key to unlocking the high stability of lead-free perovskite [21]. During conventional preparation using solvents, a small portion of tin is already in the Sn^{4+} state right from the beginning [22]. There are several strategies to suppress the oxidation such as the addition of SnF_2 [20], adding reducing agents [23, 24], or adding a metal Sn layer in between the perovskite and the electrodes [25]. However, Sn^{4+} always remains to some

extent. A very promising route is the growth of tin halide perovskites in ultra-high vacuum conditions [26].

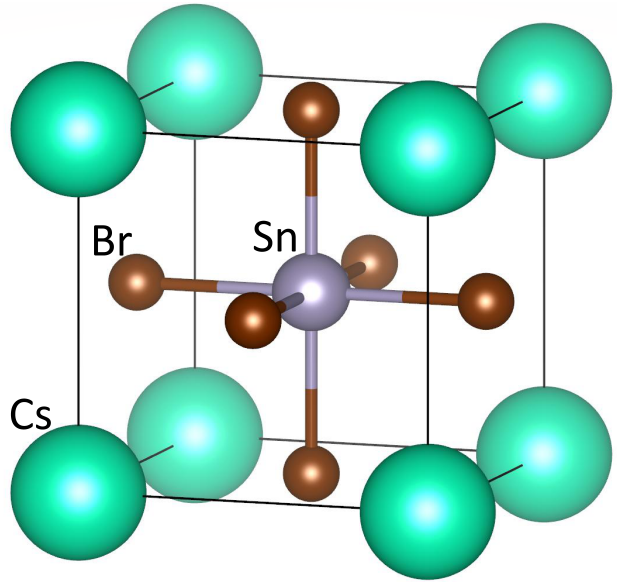


Figure 2.1: $CsSnBr_3$ perovskite crystal structure [27].

The surface structure of perovskite films is considered crucial for understanding their interfacial and electrical properties [28]. In this thesis, the all-inorganic tin perovskite $CsSnBr_3$ is studied as a model system. Cesium (Cs) occupies the A-site cation, tin (Sn) the B-site cation, and bromine (Br) the X-site anion (Figure 2.1). At room temperature, $CsSnBr_3$ is observed to adopt a cubic crystal structure with a lattice constant of 5.8196(7) Å, as determined by X-ray diffraction [29–31]. A suitable band gap for tandem solar cells with silicon is attributed to $CsSnBr_3$, along with an exciton binding energy below the thermal energy [32]. Superior thermal stability and moisture resistance are exhibited by $CsSnBr_3$ compared to its organic counterparts, making it highly suitable for applications such as direct X-ray detectors and solar cells [32, 33].

2.1.1 Shockley–Queisser limit

The Shockley-Queisser (SQ) limit is a theoretical framework used to estimate the maximum efficiency of a single-junction solar cell under 6000 K black-body radiation. First published by William Shockley and Hans-Joachim Queisser in 1961 [13], the SQ limit is derived from the principle of detailed balance, which states that at thermal equilibrium, the rate of photon absorption equals the rate of photon emission in a solar cell. This limit represents a thermodynamic upper bound on solar cell efficiency, considering the balance between incoming solar radiation and outgoing thermal radiation. Specifically applying to solar cells with a single p-n junction, the SQ limit is a function of the bandgap E_g of the semiconductor absorber material. The maximum SQ limit is achieved for a bandgap of approximately 1.34 eV, corresponding to a theoretical efficiency of about 33.7%. The efficiency curve of the

SQ limit forms a peak around 1.34 eV and decreases for both wider and narrower bandgaps (Figure 2.2).

The provided graph (Figure 2.2) depicts the PCE versus bandgap for various solar cell technologies, including perovskite solar cells (PSCs). The Shockley-Queisser limit is illustrated as a curve showing the theoretical maximum efficiency for single-junction solar cells based on their bandgap.

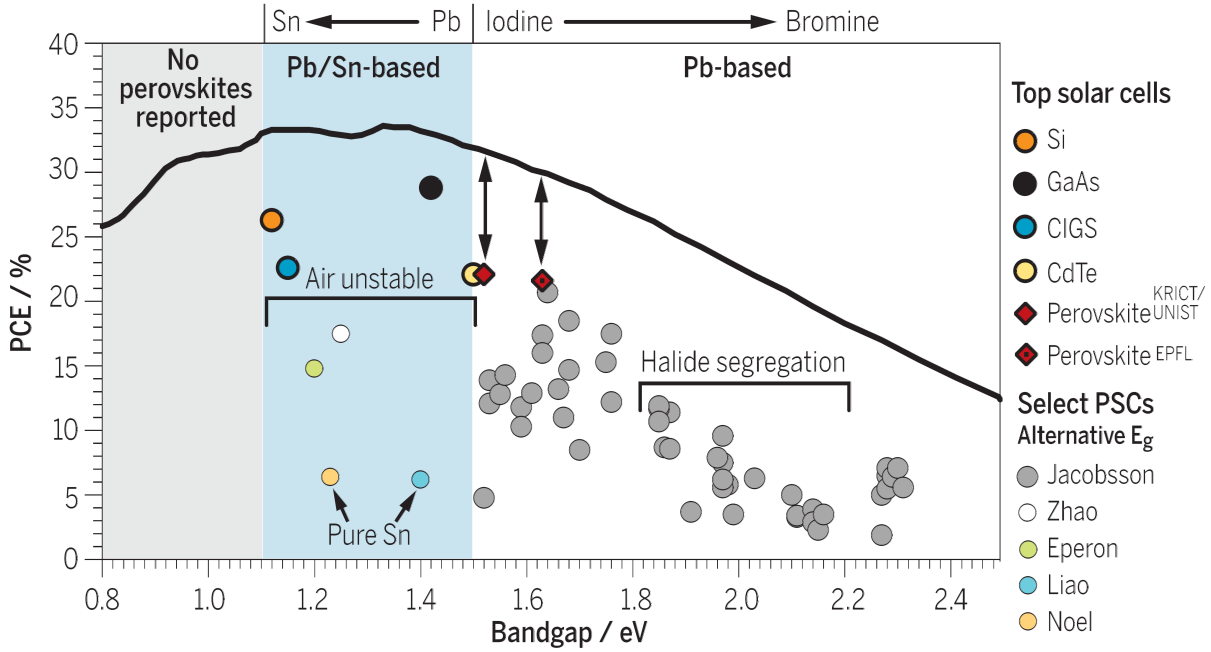


Figure 2.2: Shockley-Queisser limit graph showing PCE vs. bandgap for different solar cell technologies [34].

The SQ model makes several simplifying assumptions, including an infinitely thick absorber layer, complete absorption of photons with energy above the bandgap, no non-radiative recombination, no parasitic absorption losses, and single electron-hole pair generation per absorbed photon [35]. Due to these idealized assumptions, the SQ limit is not practically achievable. However, it serves as a benchmark for comparing the performance of different solar cell technologies and guiding research towards higher efficiencies. Real solar cells experience efficiency losses due to deviations from the idealized assumptions of the SQ model. The SQ limit considers only radiative recombination, where the absorbed photon energy is re-emitted as light, but real cells experience non-radiative recombination through defects and impurities, converting absorbed energy into heat. Reflection losses, parasitic absorption, thermalization losses, voltage loss, current loss, and fill factor loss are other factors that contribute to the lower efficiency of real solar cells.

Mathematically, the SQ model uses the Shockley diode equation to describe the current-voltage (J-V) characteristics of a solar cell. The J-V curve is a plot of current density (J) versus voltage (V) and is used to determine solar cell parameters, including the short-circuit

current (J_{sc}), open-circuit voltage (V_{oc}), fill factor (FF), maximum power point (MPP), efficiency (η), saturation current density (J_0), radiative recombination current ($J_{0,rad}$), and non-radiative recombination current ($J_{0,nonrad}$). The model assumes the solar cell is in thermal equilibrium with a blackbody at 300 K, which emits radiation that contributes to $J_{0,rad}$. Planck's law describes the spectral distribution of blackbody radiation as a function of temperature and wavelength. The J_0 calculation involves integrating the blackbody radiation spectrum over all incident angles and wavelengths. The J_{sc} is calculated by integrating the product of the external quantum efficiency (EQE) and the solar photon flux over all wavelengths, while the $J_{0,rad}$ is calculated by integrating the product of the EQE and the blackbody radiation spectrum over all wavelengths. Due to the complexity of these integrals, the SQ limit is typically calculated numerically.

In practical terms, the SQ limit assumes an infinitely thick absorber, which is not realistic for thin-film solar cells. A more realistic efficiency limit for thin-film solar cells considers the finite thickness and optical properties of the absorber layer. Light trapping techniques, such as texturing, can be used to increase the effective path length of light in thin-film absorbers. Parasitic absorption in non-active layers, such as transparent conductive oxides (TCOs) and contacts, reduces the number of photons reaching the absorber. Reflection from the front surface of the solar cell can be minimized using anti-reflection coatings. Defects and impurities in the absorber layer lead to non-radiative recombination, reducing V_{oc} and FF. Resistance in the contacts and interconnections and leakage currents through the solar cell reduce the FF. The SQ limit is calculated at a specific temperature (usually 25°C), but solar cell performance varies with temperature. The solar spectrum varies with location, time of day, and weather conditions, affecting the actual efficiency of a solar cell. The angle at which sunlight strikes the solar cell also affects its performance. Real solar cells exhibit non-ideal diode behavior, with ideality factors greater than 1, leading to further efficiency losses.

Perovskite solar cells have demonstrated high efficiencies due to their strong light absorption, long carrier diffusion lengths, and tunable bandgaps. However, their efficiency is still below the SQ limit, indicating room for further improvement. One of the main limitations in perovskite solar cells is the V_{oc} loss due to non-radiative recombination at interfaces and within the bulk. The FF of perovskite solar cells is also limited by series and shunt resistances, as well as non-ideal diode behavior. Perovskite solar cells are typically fabricated as thin films, making the thin-film efficiency limit more relevant than the SQ limit. The bandgap of perovskite materials can be tuned by varying the composition, allowing for optimization of the SQ limit for specific applications. Mixed halide perovskites (e.g., $MAPb(I_{1-x}Br_x)_3$) offer a way to tune the bandgap, but they can suffer from phase segregation, which reduces efficiency. Tandem and multi-junction perovskite solar cells can exceed the SQ limit by using multiple absorber layers with different bandgaps. Perovskite/silicon tandem cells have shown great promise, with efficiencies exceeding 29% [36].

Perovskite solar cells exhibit varying performance depending on their composition. Pb-based perovskites, with bandgaps ranging from 1.5 to 2.3 eV, have achieved efficiencies close to 22%, competing with top technologies like silicon (Si) and gallium arsenide (GaAs).

Pb/Sn mixed perovskites, with lower bandgaps (1.0–1.5 eV), face limitations due to air instability and halide segregation, which reduce their efficiency. Pure Sn-based perovskites, with bandgaps around 1.2 eV, show efficiencies below 10% due to material instability. The optimal bandgap for perovskites, around 1.3 eV, balances photon absorption and thermalization losses, maximizing energy conversion efficiency.

2.2 STM (Scanning Tunneling Microscopy)

The STM was invented in 1981 by Gerd Binnig and Heinrich Rohrer, two physicists at IBM Zurich in Switzerland [37]. For this invention, they were awarded the half of the Nobel Prize in Physics in 1986 [38]. The invention of the STM changed the course of surface science and engineering. It also has proven to be an essential instrument for probing a wide range of fundamental aspects related to surface properties, which are critical in technological realms. As well as making possible the imaging of localized bonding arrangements and defects, the STM has been pivotal in revealing the presence of non-periodic structures and the simultaneous existence of various nanoscale phases. It has the unique capability of being sensitive to the local electronic structure of a surface down to the atomic scale without averaging over many unit cells. This allows the STM to be used as a spectroscopic tool at low temperatures to determine the superconducting energy gap on a local scale, which is very advantageous, particularly for sintered materials, where the grain size hardly exceeds several microns. The STM has opened the door for the other scanning probe microscopy techniques including atomic force microscopy (AFM), magnetic force microscopy (MFM), electrostatic force microscopy (EFM).

The working principle of the STM cannot be explained by classical physics since it is based on the tunneling effect which is a purely quantum mechanical phenomena. When the sharp metallic tip, which in the ideal case is terminated by a single atom, comes closer (a few Å) to the conductive surface (let us assume it is a metal for simplicity), the applied bias causes electrons to tunnel from the tip to the surface (or vice versa depending on the polarity).

To understand the tunneling process, consider a simple one-dimensional case where an electron with total energy of E has to pass through the barrier of height $\Phi > E$. In classical physics, such a process is prohibited since we deal with particles. Quantum mechanics, however, allows for a description of the particle by a wave function $\psi(z)$, which can penetrate finite barriers, continuing on the other side with a smaller amplitude but unchanged wave number (Figure 2.3). Consequently, electrons can tunnel between two closely spaced metals without physical contact. When one metal is a finely pointed tip, ideally monoatomic, positioned above the other metal's surface, tunneling is spatially confined to the immediate vicinity of the tip. This is the fundamental principle of the STM.

The process also depends on the fundamental principle of quantum mechanics called Pauli exclusion principle: an electron can tunnel only if vacant quantum states exist on the opposite side of the barrier, as shown in Figure 2.4. When the Fermi levels (E_{F}) of the metals align, in other words when there is no voltage applied, $U_B = 0$, all states below E_{F}

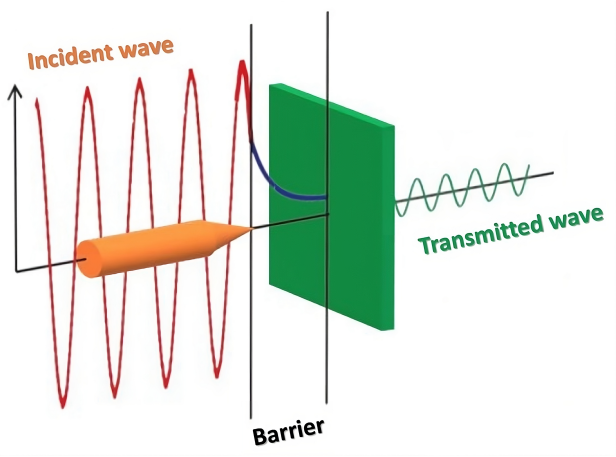


Figure 2.3: Tunneling process of the electron wave from the tip to the sample.

are filled. In this scenario, tunneling from one metal to the other is a matter of probability on a corresponding state becoming available. A detectable current arises only when there is a net directional electron flow. Such flow can be induced by a small voltage $U_B \neq 0$.

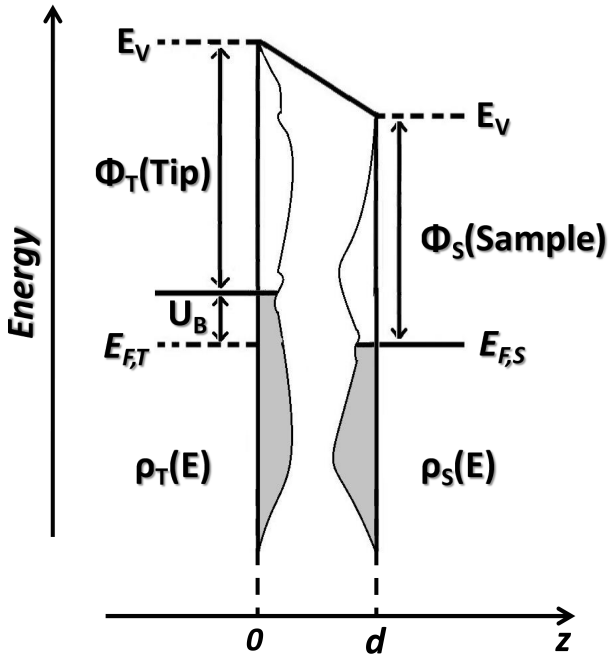


Figure 2.4: Energy diagram of the tunneling process involving the tip (T) and the sample (S). E_{V} - vacuum level, E_{F} - Fermi level, Φ - work function, z - direction of the tunneling, U_B - applied bias, $\rho(E)$ - local density of states.

Now let us write the equation for this tunneling current [39–42]. When the tip is far away from the sample, the wave function of the electron in the sample satisfies the Schrödinger equation:

$$i\hbar\frac{\partial}{\partial t}\psi_S = \left(-\frac{\hbar^2}{2m}\frac{\partial^2}{\partial z^2} + U_S\right)\psi_S, \tag{2.1}$$

where U_S is the potential function of the sample, and the wavefunction ψ_S depends on both time and spatial coordinates. The stationary states are $\psi_S = \psi_{S\mu}e^{-iE_{S\mu}t/\hbar}$, with

$$\left(-\frac{\hbar^2}{2m}\frac{\partial^2}{\partial z^2} + U_S\right)\psi_{S\mu} = E_{S\mu}\psi_{S\mu}. \tag{2.2}$$

Once the tip and the sample get closer, the electron in the sample feels the potential from the tip thus the Schrödinger equation for the system becomes:

$$i\hbar\frac{\partial}{\partial t}\psi = \left(-\frac{\hbar^2}{2m}\frac{\partial^2}{\partial x^2} + U_T + U_S\right)\psi \tag{2.3}$$

At $t \to -\infty$, the tip is far away from the substrate and the electrons in both tip and sample are in the eigenstates the Schrödinger equation 2.3 describes, and will evolve as stationary states. The potential of the tip will be present slowly while the tip approaching the sample. We assume this as a perturbation potential. We also assume that the tip approaches the sample surface slowly, thereby the tip potential is turned on adiabatically. We can describe the potential as

$$U_T(t) = e^{\eta t/\hbar}U_T, \tag{2.4}$$

to satisfy the assumption. Here U_T is independent on t and η is small positive quantity.

Switching on the perturbation ($t \to 0$), the final state of the electron will include both the tip and the sample stationary states:

$$\psi = a_\mu(t)\psi_\mu^S e^{-iE_\mu^S t/\hbar} + \sum_\nu c_\nu\psi_\nu^T e^{-iE_\nu^T t/\hbar}. \tag{2.5}$$

From our ansatz, $a_\mu(-\infty) = 1$ and $c_\nu(-\infty) = 0$.

The basic assumption of Bardeen's model [42] is that the two sets of wave functions are approximately orthogonal, i.e.,

$$\int \psi_\mu^*\psi_\nu\, d^3r = 0.$$

Inserting 2.5 into the time-dependent Schrödinger equation (2.3), we obtain

$$i\hbar\frac{dc_\nu(t)}{dt} = \langle\psi_\nu|U_T|\psi_\mu\rangle e^{-i(E_\mu - E_\nu + i\eta)t/\hbar} + \sum_\lambda c_\lambda(t)\langle\psi_\nu|U_S|\psi_\lambda\rangle e^{-i(E_\lambda - E_\nu + i\eta)t/\hbar}. \tag{2.6}$$

This equation can be solved iteratively, and as a good approximation we focus only on the first order of time-dependent perturbation theory and neglect the second term on the right hand side. Then we obtain:

$$c_\mu(t) = \frac{M_{\mu\nu}}{E_{S\mu} - E_{T\nu} + i\eta}e^{-i(E_{S\mu} - E_{T\nu})t/\hbar}, \tag{2.7}$$

with $M_{\mu\nu} = \langle \psi_\mu^S | U_T | \psi_\nu^T \rangle$ being the tunneling matrix element describing the projection of the initial state ψ_μ^S perturbed by the potential U_T onto the final state ψ_ν^T.

The term $|c_\mu(t)|^2$ describes the probability that an electron which sits in the initial state ψ_μ^S at $t = -\infty$ populates a state ψ_ν^T at time t:

$$|c_\mu(t)|^2 = \frac{|M_{\mu\nu}|^2}{(E_{S\mu} - E_{T\nu})^2 + \eta^2} e^{2\eta t/\hbar}, \tag{2.8}$$

which leads to the tunneling probability per unit time

$$P_{\mu\nu} = \frac{d}{dt}|c_\mu(t)|^2 = \frac{2\eta}{(E_{S\mu} - E_{T\nu})^2 + \eta^2} \frac{1}{\hbar} e^{2\eta t/\hbar} |M_{\mu\nu}|^2. \tag{2.9}$$

Now we set η to 0. In the recognition of the delta function, i.e., $\delta(x) = \frac{1}{\pi} \lim_{\eta \to 0} \frac{\eta}{x^2 + \eta^2}$, we have the famous Fermi's golden rule:

$$P_{\mu\nu} = \frac{d}{dt}|c_\mu(t)|^2 = \frac{2\pi}{\hbar} \delta(E_{S\mu} - E_{T\nu}) |M_{\mu\nu}|^2. \tag{2.10}$$

The tunneling probability $P_{\mu\nu}$ connects the initial state ψ_μ^S and the final state ψ_ν^T. However, in both the tip and the sample, electrons sit in a lot of different states. So the tunneling current is proportional to the sum of all the tunneling probabilities between different states in tip and sample. Furthermore, at finite temperature, we also have to include the thermal effect, which means the occupation probability of a state with eigenenergy E is described by the Fermi-Dirac distribution

$$f(E - E_F) = \frac{1}{e^{(E - E_F)/k_B T} + 1}. \tag{2.11}$$

Accounting for the occupation in this distribution, two spin directions in one state and assuming a bias voltage eU_B, the tunneling current in thermal equilibrium from the sample to the tip, $I_{S \to T}$, and from the tip to the sample, $I_{T \to S}$, can be expressed as:

$$I_{S \to T} = \frac{4\pi e}{\hbar} \sum_{\mu\nu} \left[f(E_\mu^S - E_F^S) \left[1 - f(E_\nu^T - E_F^T) \right] \right] |M_{\mu\nu}|^2 \delta(E_\nu^T - E_\mu^S - eU_B), \tag{2.12}$$

and

$$I_{T \to S} = \frac{4\pi e}{\hbar} \sum_{\mu\nu} \left[f(E_\mu^T - E_F^T) \left[1 - f(E_\nu^S - E_F^S) \right] \right] |M_{\mu\nu}|^2 \delta(E_\nu^S - E_\mu^T - eU_B), \tag{2.13}$$

The difference between two directions is the net total tunneling current:

$$I = \frac{4\pi e}{\hbar} \sum_{\mu\nu} \left[f(E_\mu^S - E_F^S) - f(E_\mu^T - E_F^T) \right] |M_{\mu\nu}|^2 \delta(E_\mu^T - E_\mu^S - eV). \tag{2.14}$$

The finite summation over the discrete states can be replaced by an integral over energies using the density of states $n(E) : \sum_\mu \to \int n(E) dE$. We can also get rid of the delta function using $\int \delta(x) dx = 1$. After appropriate change of variables, we have:

$$I = \frac{4\pi e}{\hbar} \int d\epsilon \left[f(E_F^T - eV + \epsilon) - f(E_F^S + \epsilon) \right] \times \rho_T(E_F^T - eV + \epsilon) \times \rho_S(E_F^S + \epsilon) |M(E_F^S + \epsilon, E_F^T - eV + \epsilon)|^2, \tag{2.15}$$

where ρ^S and ρ^T are the density of states (DOS) of the substrate and of the tip. At zero temperature or if $k_B T$ is smaller than the energy resolution required in the measurement, the Fermi distribution function can be approximated by a step function and the current simplifies to

$$I = \frac{4\pi e}{\hbar} \int_0^{eU_B} d\epsilon \, \rho_T(E_f^T - eU_B + \epsilon) \rho_S(E_f^S + \epsilon) |M|^2. \tag{2.16}$$

We see that the tunneling current is the convolution of the density of states of the tip and the sample. Then the differential conductivity is given by (for a small tunneling voltage):

$$\frac{dI}{dV} = \frac{4\pi e}{\hbar} \rho^T(E_F^T) \rho^S(E_F^S + eU_B) |M(E_F^S + eU_B, E_F^T)|^2. \tag{2.17}$$

This explains the unique power of STM to be able to access the occupied and unoccupied electronic states of the substrate. Indeed this can be achieved by changing the sign of the bias voltage.

There are two modes for imaging the surface morphology. The constant-current mode, which was used in this work, can be derived from the above equations. Rearranging equations to solve for z, we get:

$$z(V, x, y) = z_0 + \frac{1}{2\sqrt{\frac{m_e}{\hbar^2}(\phi^T + \phi^S(x, y))}} \cdot \ln \left(\frac{\int_0^{eU_B} dE \, \rho^T(E - eU_B) \rho^S(E, x, y)}{I_0} \right) \tag{2.18}$$

here, ϕ^T and ϕ^S are the work functions of the tip and the sample. For constant current measurements, the apparent height z primarily depends on the local density of states (LDOS) of the sample. Variations in the work function across the sample have only a minor impact on the observed height. The LDOS is influenced by the atomic arrangement on the surface, enabling atomic-resolution imaging. Additionally, the LDOS is affected by the chemical properties of the atoms, surface states, and other electronic effects, which must be considered when interpreting STM images. When imaging adsorbates, such as adatoms or molecules, their interaction with the surface can alter the electronic structure. Therefore, the interpretation requires considering not only the electronic properties of the isolated adsorbate but also the combined adsorbate-surface system.

2.3 LEED (Low-Energy Electron Diffraction)

LEED is a widely employed technique for studying surface structures. In this process, electrons are accelerated toward the sample, and structural information is extracted from the

analysis of elastically scattered electrons. The electrons' energy typically ranges from 30 eV to 200 eV, corresponding to wavelengths between 1 Å and 2 Å, which match atomic distances. Due to the short mean free path of electrons at these energies, most elastic scattering occurs in the uppermost atomic layers, allowing surface-sensitive structural investigation [43].

The LEED setup, as shown in Figure 2.5, allows direct visualization of the diffraction pattern. The electron gun produces a collimated low-energy electron beam that passes through a hemispherical fluorescent screen and four grids, allowing for the analysis of diffraction patterns from the scattered electrons.

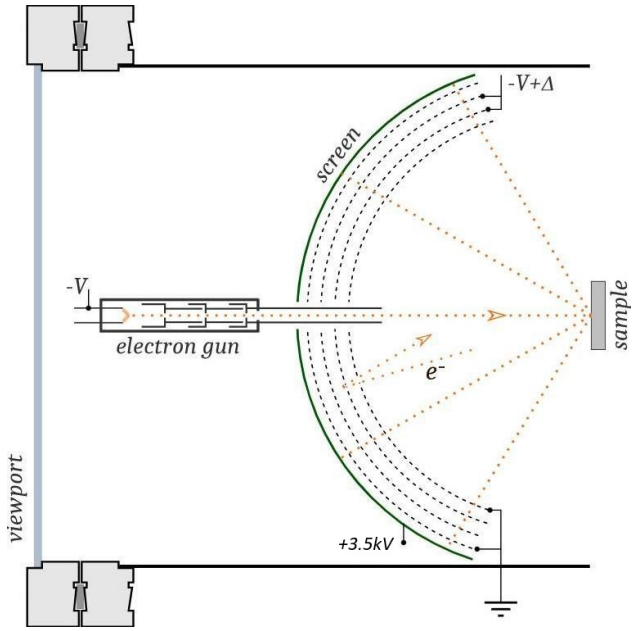


Figure 2.5: Schematic of a rear-view LEED instrument adapted from [45].

In this setup, the electron beam is generated by the cathode filament within the electron gun. A Wehnelt cylinder and electrostatic lenses focus the beam onto the sample. While the cathode is held at a negative potential ($-V$), the last lens aperture, the sample, and the first grid are grounded. This accelerates the electron beam toward the sample with energy $e \cdot V$. After interaction with the sample, the scattered electrons pass through a field-free region. The second and third grids are set at a slightly lower potential ($-(V - \Delta V)$) to filter out inelastically scattered electrons. As ΔV increases, the brightness of the LEED pattern improves, though background intensity also increases. Thus, the voltage must be adjusted carefully to obtain optimal patterns. The fourth grid is grounded to shield the other grids from the fluorescent screen, which is biased at approximately 3.5 kV. This reaccelerates the diffracted electrons to create fluorescence, which visualizes the pattern. The electron gun is visible in the LEED pattern, as seen in the figures.

To understand the LEED pattern, reciprocal space must be considered, as the diffraction pattern corresponds directly to the crystal's reciprocal lattice by Laue's condition:

$$\vec{k_f} - \vec{k_i} = \vec{G_{hkl}},$$

where $\vec{k_f}$ and $\vec{k_i}$ represent the scattered and incident wave vectors, respectively, and $\vec{G_{hkl}}$ is the reciprocal lattice vector. Constructive interference occurs when the difference between $\vec{k_f}$ and $\vec{k_i}$ is equal to a reciprocal lattice vector. The Ewald construction is a geometric tool that helps visualize how diffraction patterns are generated. The Ewald sphere resides in reciprocal space, and its radius is defined by the incident wave vector $|\vec{k_i}|$. As the electron beam energy increases, the Ewald sphere's radius expands, intersecting more reciprocal lattice points, which manifest as diffraction spots.

In LEED, because electrons have a shallow penetration depth, only the components of the wave vector parallel to the surface are significant. This leads to a rod-like structure in reciprocal space, rather than discrete points. When the Ewald sphere intersects these reciprocal lattice rods, Laue's diffraction condition is met, and diffraction spots are observed.

These diffraction patterns provide vital information about the sample's reciprocal lattice, allowing insights into the real-space atomic structure. Furthermore, surface superstructures can also be observed in the diffraction pattern. A well-ordered surface will result in sharp, bright diffraction spots with minimal background noise.

2.4 XPS (X-ray Photoelectron Spectroscopy)

XPS is a technique used to explore the electronic structure of atoms and molecules. It is based on the photoelectric effect, first explained by Albert Einstein in 1905 [46]. Photoelectron spectroscopy (PES) works by shining high-energy radiation, like ultraviolet (UV) or X-rays, onto a sample. This energy causes electrons to be ejected from the material. By measuring the kinetic energy (E_{kin}) of these electrons, XPS can determine their binding energy (E_{B}) within the material [44].

The results of an XPS experiment are typically presented as a spectrum, with the x-axis representing the binding energy and the y-axis depicting the number of photoelectrons detected at the specific energy level. This spectrum resembles a fingerprint, with distinct peaks corresponding to electrons occupying different energy levels (subshells) within the atoms of the sample. Electrons residing closer to the nucleus, known as core electrons, exhibit higher binding energies. Conversely, valence electrons, located further from the nucleus and more loosely bound, manifest as peaks at lower binding energies.

In XPS, the sample is irradiated with X-ray photons typically in the energy range of 200–1500 eV, causing electrons to be ejected from the material. After being ejected from the sample, the electrons travel to an energy analyzer. This instrument sorts them based on their kinetic energy. At the end a detector counts the number of photoelectrons at each energy level, as illustrated in Figure 2.6.

XPS, stands as a cornerstone technique for analyzing the elemental composition of a material's surface. XPS is particularly useful because it's very surface sensitive, meaning it provides information only from the top few nanometers of a material. It has a poor spatial resolution, meaning it can't distinguish features smaller than about 5 microns. Additionally, while its surface sensitivity is an advantage for many applications, it can be a disadvantage if you're interested in the bulk composition of a material. XPS also has limitations in

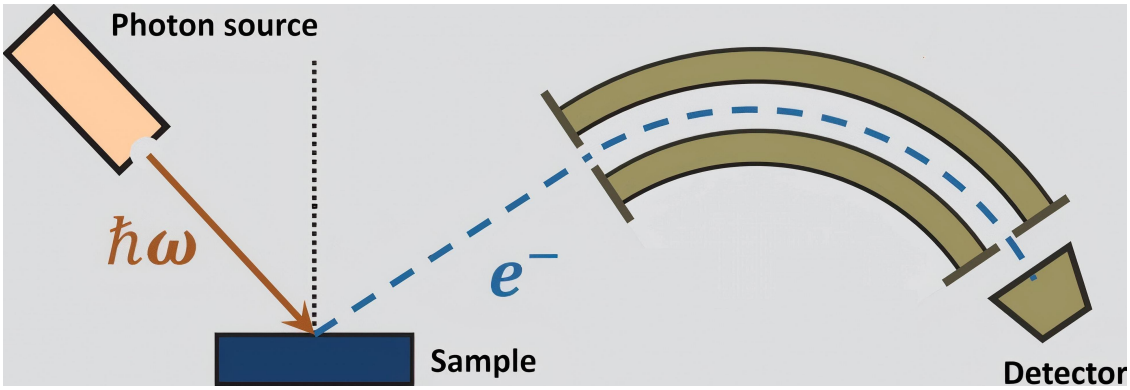


Figure 2.6: A sample is irradiated with photons of energy $\hbar\omega$, causing electrons to be emitted and detected. Image taken from [47].

its detection limits, typically only reaching around 0.1% for most elements, and it cannot detect hydrogen at all, unless specific conditions are met such as ambient pressures and using high intensity photon sources (synchrotrons) [48]. Despite these drawbacks, XPS remains a valuable tool for researchers who need to understand the chemical composition of a material's surface.

In XPS, the incident radiation consists of soft X-rays, typically ranging from 0.1 keV to 10 keV. These X-rays, often generated from aluminium or magnesium anodes due to their suitable properties, possess enough energy to eject core electrons from the sample. The following equation captures the energy conservation principle in XPS [47]:

$$\hbar\omega = \Phi + E_{\text{kin}} + E_B \tag{2.19}$$

This equation, illustrated in Figure 2.7, highlights the relation between the incident X-ray energy ($\hbar\omega$), the work function of the sample and spectrometer combined (Φ), the kinetic energy of the ejected electron (E_{kin}), and the binding energy of the electron within the atom (E_B). By measuring the kinetic energy of the photoelectrons and knowing the X-ray energy and work function, we can calculate the binding energy of the electrons in the sample.

The binding energy of a photoelectron peak is a fingerprint, uniquely identifying the specific orbital from which the electron originated. This allows XPS to perform a chemical analysis of the sample's surface, revealing the elements present and their relative abundance. Additionally, XPS sheds light on the oxidation state of each element. Higher oxidation states typically correspond to tighter binding of electrons, resulting in a slight increase in binding energy compared to lower oxidation states. This phenomenon, known as a chemical shift, allows XPS to distinguish between different oxidation states of the same element.

Beyond this, spin-orbit coupling further complicates the picture by splitting emission lines in the spectrum. These splittings exhibit characteristic intensity ratios that depend on the electron orbital involved. The ratios are as follows: $\mathrm{p}_{3/2} : \mathrm{p}_{1/2} = 2 : 1$, $\mathrm{d}_{5/2} : \mathrm{d}_{3/2} = 3 : 2$ and $\mathrm{f}_{7/2} : \mathrm{f}_{5/2} = 4 : 3$.

While X-rays have the ability to penetrate several micrometers into a sample, only electrons residing near the surface contribute significantly to the XPS signal. This limitation

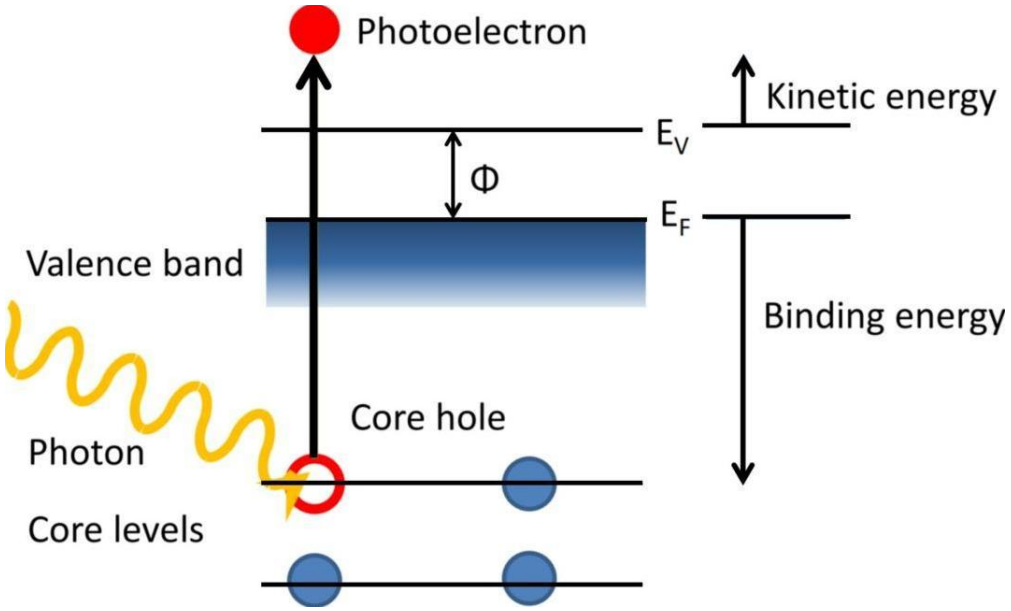


Figure 2.7: Conservation law of energy in the photoemission process. Electrons can be excited to the vacuum level E_V by the energy $\hbar\omega$ of the X-ray radiation if this energy exceeds the binding energy E_B and the work function Φ. The emitted electrons move with kinetic energy E_{kin}.

arises due to the short mean free path of electrons at these characteristic energies in solids. Electrons originating from deeper layers can undergo inelastic scattering events, losing energy and contributing to a broad background signal in the spectrum. This background must be meticulously removed during data analysis to isolate the true photoelectron peaks.

2.5 DFT (Density functional theory)

Density functional theory (DFT) is a powerful quantum mechanical method used to study electronic structures of matter, commonly applied in chemistry and physics. It simplifies the many-electron Schrödinger equation by focusing on electron density $n(\mathbf{r})$ rather than the wave function. Based on the Hohenberg-Kohn theorem [49] and the Kohn-Sham equations [50], it provides computational efficiency while maintaining accuracy in predicting properties like binding energies and band structures.

In quantum mechanics, a system's wave function, Ψ, depends on electronic coordinates and is computed using the Schrödinger equation. For many-body systems, the time-independent Schrödinger equation is:

$$\hat{H}\Psi = \left[\hat{T} + \hat{V} + \hat{U}\right]\Psi = E\Psi, \tag{2.20}$$

where $\hat{H}$ is the Hamiltonian, E is the total energy, $\hat{T}$ is kinetic energy, $\hat{V}$ is the external potential from nuclei, and $\hat{U}$ represents electron-electron interactions. However, solving this equation directly is computationally demanding due to the electron interaction term.

To simplify the treatment of nuclei and electrons in molecular systems, the Born-Oppenheimer approximation [51] is used. It separates nuclear and electronic motions by treating nuclei as fixed while electrons move in the potential created by these stationary nuclei. This reduces the complexity of the Hamiltonian and is a standard approximation used in many quantum mechanical models.

DFT bypasses the complexity of the many-body Schrödinger equation by focusing on electron density $n(\mathbf{r})$. The Hohenberg-Kohn (HK) theorem [49] asserts that ground-state properties are determined by $n(\mathbf{r})$, implying that the energy functional $F[n]$ depends only on $n(\mathbf{r})$. The Kohn-Sham approach [50] introduces non-interacting particles with the same electron density as the interacting system, reducing the problem to a simpler, single-particle system.

The Kohn-Sham equation is given by:

$$\left(-\frac{1}{2}\nabla^2 + V_{\text{eff}}(\mathbf{r})\right)\phi_i(\mathbf{r}) = \epsilon_i\phi_i(\mathbf{r}), \tag{2.21}$$

where $V_{\text{eff}}(\mathbf{r})$ is the effective potential, and $\phi_i(\mathbf{r})$ are single-particle orbitals. The electron density is calculated by summing over all orbitals:

$$n(\mathbf{r}) = \sum_{i=1}^{N} |\phi_i(\mathbf{r})|^2. \tag{2.22}$$

The effective potential V_{eff} includes contributions from the external potential, electron-electron interaction, and the exchange-correlation term:

$$V_{\text{eff}}(\mathbf{r}) = V(\mathbf{r}) + \int \frac{n(\mathbf{r}')}{|\mathbf{r} - \mathbf{r}'|} d^3r' + V_{\text{XC}}(n(\mathbf{r})), \tag{2.23}$$

where $V_{\text{XC}}(n(\mathbf{r}))$ is the exchange-correlation potential, which requires careful approximation. Two widely used approximations are the local density approximation (LDA) [52, 53]:

$$V_{\text{XC}}(n(\mathbf{r})) = \int \epsilon_{\text{XC}}(n(\mathbf{r}))n(\mathbf{r})d^3r, \tag{2.24}$$

and the generalized gradient approximation (GGA), which includes the density gradient [54]:

$$V_{\text{XC}}(n(\mathbf{r})) = \int \epsilon_{\text{XC}}(n(\mathbf{r}), \nabla n(\mathbf{r}))n(\mathbf{r})d^3r. \tag{2.25}$$

The local density approximation is the core of DFT. It is the simplest, being derived from conditions on the uniform gas. Though it is too inaccurate for quantum chemistry (being off by about 1 eV or 30 kcal/mol), it is useful in solids and other bulk materials where the electrons almost look like a uniform gas. The generalized gradient approximation came from trial and error when energies were allowed to depend on the gradient of the density. While more accurate than the LDA (getting errors down to 5 or 6 kcal/mol), and thus useful for quantum chemistry applications, there is no uniquely-defined GGA. Becke 88 exchange [55] with LYP correlation (BLYP) is an empirical GGA that was designed to

minimize the error in a particular data set. Perdew-Burke-Ernzerhof (PBE) [54] is a non-empirical GGA designed to satisfy exact conditions [56]. Despite several approximations in DFT, the method remains a computationally efficient tool for predicting ground-state properties of multi-electron systems. For our experimental results, the electron exchange-correlation interactions were modelled in the generalized gradient approximation using the (PBE) functional.

Chapter 3

Experimental Setup

3.1 VT-STM (Variable Temperature - Scanning Tunneling Microscope)

A Scienta Omicron variable temperature scanning tunneling microscope (VT-STM) system was utilized in this thesis for the preparation and analysis of the precursor molecules and perovskite samples. A schematic of the system is shown in Figure 3.1.

The system comprised two separate ultra-high vacuum (UHV) chambers: the analysis chamber and the deposition chamber. The base pressure in the analysis chamber was maintained at 1×10^{-10} mbar. A gate valve provided a connection between the analysis chamber and the fast entry lock (FEL), allowing samples and STM tips to be introduced into the system and stored in the carousel without venting the entire chamber. The wobblestick was used to transfer samples from the carousel to either the manipulator or the STM.

The STM was cooled down to 118 K using the nitrogen bath cryostate when needed. The four-axis manipulator in the system was equipped with an e-beam heater for sample heating, while a pyrometer located outside the vacuum chamber remotely measured the sample temperature through a viewport.

Sample cleaning was accomplished using an ion gun, which was attached to the analysis chamber along with a gas doser for argon ions. Structural characterization of the sample surface was performed using a low-energy electron diffraction/auger electron spectroscopy (LEED/AES) equipment.

Pressure in the analysis chamber was further improved using a titanium sublimation pump (TSP) and a cooling trap. The analysis and deposition chambers were isolated by a gate valve, and the base pressure in the deposition chamber was kept at 5×10^{-10} mbar. A transfer arm moved the sample from the manipulator in the analysis chamber to the heater stage in the deposition chamber. The 3-cell TCE-BSC evaporator from Kentax GmbH was attached to the system for precise ultrathin film depositions for this thesis (Figure3.1 (11)). The evaporator had two valves attached to it. One was to seperate it from the deposition chamber when needed and the other was used to isolate it from air when transferring from glovebox to the chamber. More details about the evaporator can be found in Chapter 3.4.

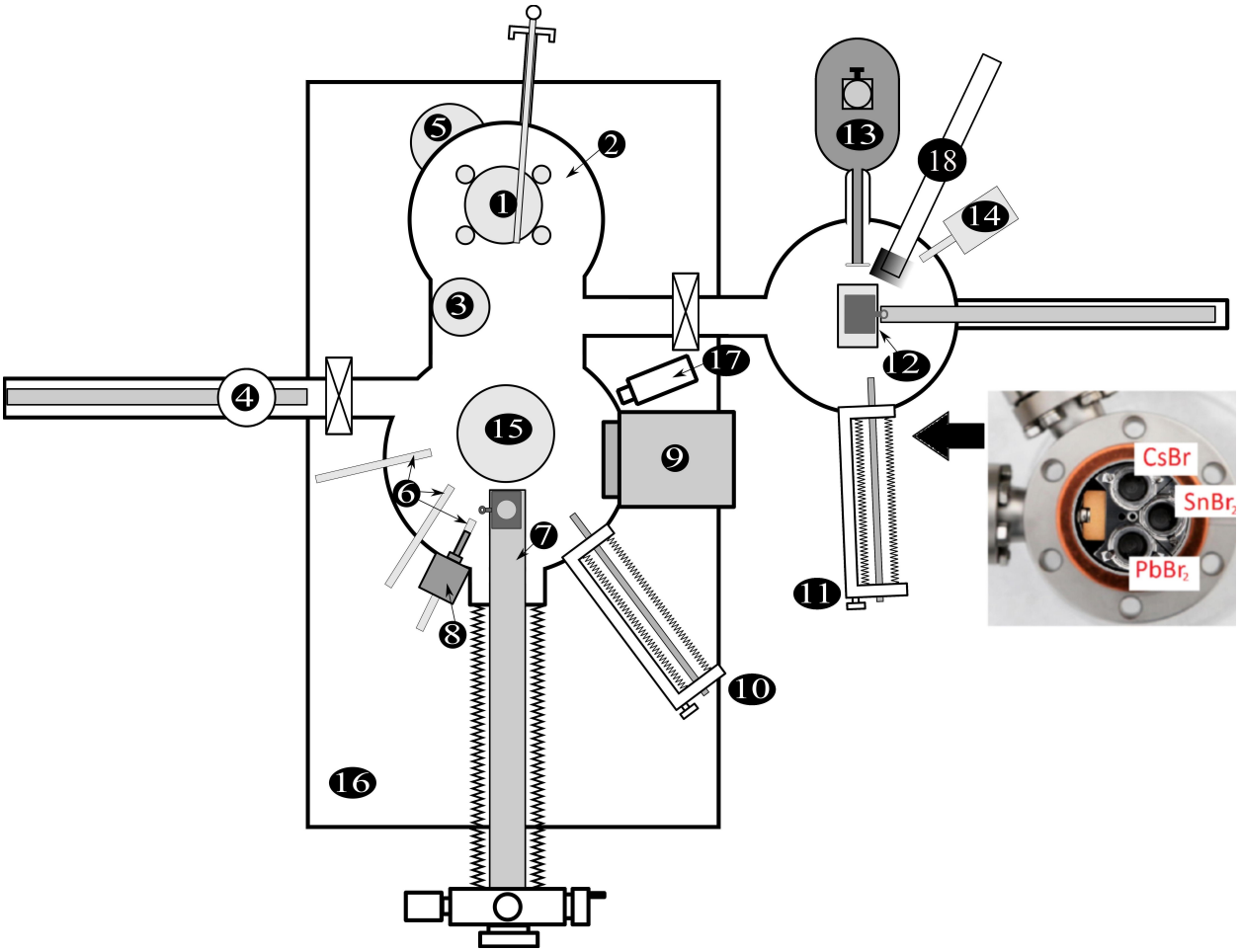


Figure 3.1: Schematic of VT-STM system from the top adopted from [57]. (1) STM, (2) wobblestick, (3) carousel, (4) FEL with transfer arm, (5) cooling reservoir, (6) gas dosers, (7) manipulator with e-beam heater and sample, (8) ion gun, (9) LEED/AES, (10) molecule evaporator, (11) molecule evaporator (photograph of the crucibles of the evaporator that were used for the experiment in this thesis), (12) heater stage, (13) valved selenium/sulfur source (VSS), (14) e-beam evaporator, (15) titanium sublimation pump (TSP) and cooling trap, (16) table, (17) pyrometer, (18) quartz crystal microbalance (QCM) . Both chambers are pumped with a turbo-pump and an ion getter pump (not shown).

3.2 X-ray Photoelectron Spectrometer

The XPS measurements were conducted under ultra-high vacuum (UHV) conditions to minimize surface contamination and ensure the accuracy of the analysis. The base pressure within the chamber was maintained around 10^{-10} mbar, providing a clean environment for the samples.

To prevent air exposure during transport between the preparation chamber (University of Siegen) and the XPS chamber (University of Luxembourg), a dedicated UHV suitcase from Scienta Omicron was employed. This suitcase maintained a vacuum level of approximately

3×10^{-10} mbar, ensuring the samples remained under UHV conditions throughout the transfer process. Inside its small chamber, there is a sample garage with six spring-loaded slots compatible with flag-style sample holders. The vacuum suitcase is pumped with an ion getter pump and a non-evaporatable getter pump (NEG pump). The latter runs without power and thus even if the ion pump is turned off the vacuum suitcase maintains UHV. More details about this vacuum suitcase can be found in [58]. A photograph of the UHV suitcase and its connection to the UHV microscopy systems at both universities is provided in Figure 3.2.

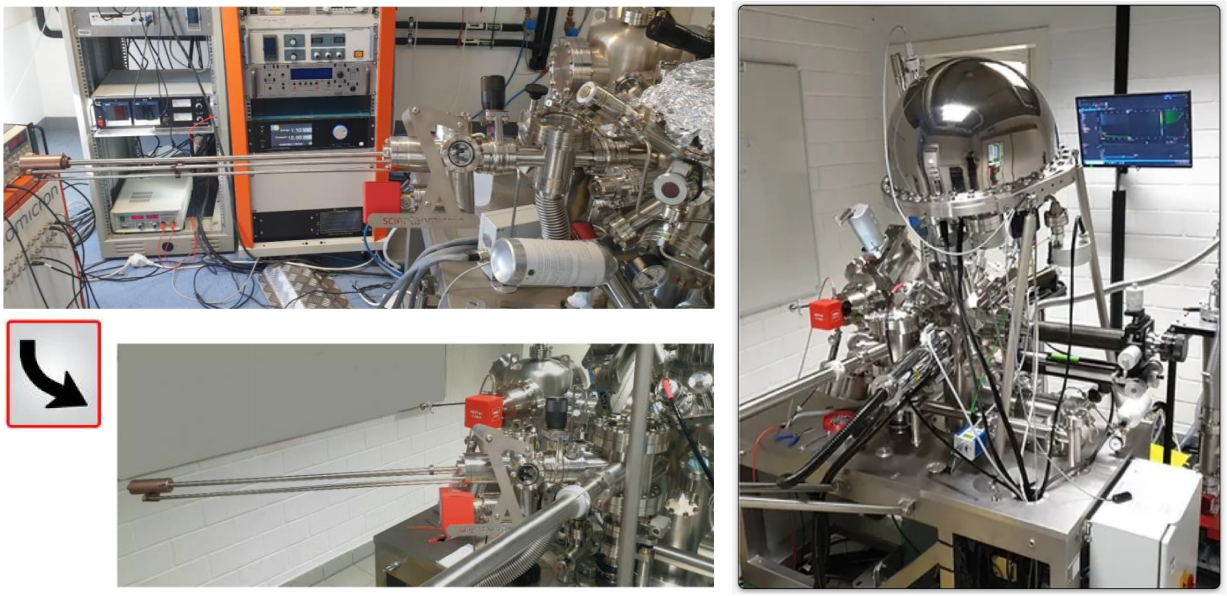


Figure 3.2: Transport and measurement of samples using a vacuum suitcase. The top left image shows the vacuum suitcase attached to the VT-STM (Variable Temperature Scanning Tunneling Microscope) at the University of Siegen. The bottom left image depicts the VT-AFM (variable temperature- atomic force microscope) with the vacuum suitcase attached at the University of Luxembourg. The right image shows the XPS analyzer (PREVAC XPS) without the vacuum suitcase at the University of Luxembourg.

XPS data were acquired using a Prevac EA15 spectrometer equipped with a non-monochromatic Mg K-α X-ray source (1253.4 eV) at the University of Luxembourg. The energy resolution of the spectrometer was 0.15 eV, offering a high degree of detail in the XPS spectra. To optimize the signal-to-noise ratio and balance measurement time with potential beam damage, an emission current of 25 mA and an anode voltage of 12 kV were used. These parameters ensured sufficient signal intensity for accurate peak identification while minimizing the X-ray dose received by the samples. The overall measurement time for each sample set was kept below 1 hour to further mitigate potential beam-induced degradation.

The acquired XPS data were analyzed using CasaXPS software [59], a comprehensive suite of tools for processing and interpreting XPS spectra. To account for the background signal arising from inelastic scattering of photoelectrons within the sample, a Spline Shirley

background function was employed. Subtracting this background component allows for more accurate determination of peak intensities and a clearer representation of the core-level electron energy distribution. Finally, the XPS peaks were fitted with a combination of Gaussian and Lorentzian functions to model their line shapes and extract precise peak positions and intensities for further analysis.

3.3 Preparation of single crystals

The gold crystals, Au(111) and Au(100), shown in Figure 3.3 and Figure 3.4 respectively, were cleaned in UHV with a base pressure of 10^{-10} mbar. After several cycles of sputtering with argon (10^{-5} mbar) and annealing in UHV, the desired surface reconstructions were observed. For Au(111), the characteristic herringbone reconstruction (Figure 3.3) became visible in the STM images and was confirmed using LEED [60, 61]. For Au(100) [62], the 26×5 reconstruction (Figure 3.4) was observed, also confirmed by LEED.

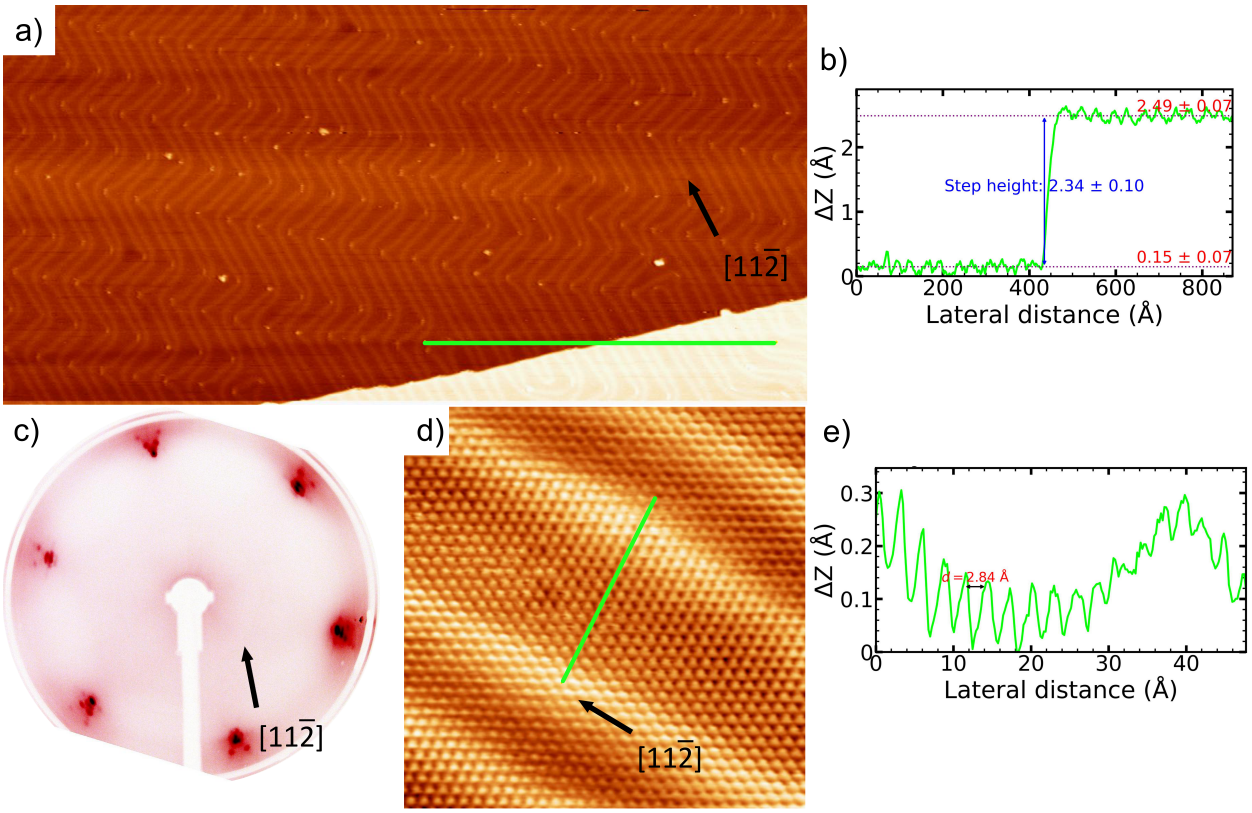


Figure 3.3: a) STM image of clean Au(111), $U_{\text{Bias}} = 0.1$ V, $I = 0.3$ nA (200×100 nm^2), b) line profile drawn in (a), c) LEED image of Au(111) at 63 eV, d) STM image of herringbone reconstruction lines and atoms of Au(111), $U_{\text{Bias}} = 0.1$ V, $I = 0.3$ nA (9.3×9.3 nm^2), e) line profile drawn in (d).

Scanning the clean gold surfaces with STM allows to define the crystal high-symmetry directions. For Au(111), a step height of 2.34 ± 0.10 Å and an atomic displacement of

approximately 2.90 Å were measured. For Au(100), a step height of 2.08 ± 0.17 Å was measured. During scanning, the STM images of clean Au(100) were rotated 45 degrees in the software to distinguish the reconstruction lines from the noise, which can often appear in STM measurements (Figure 3.4).

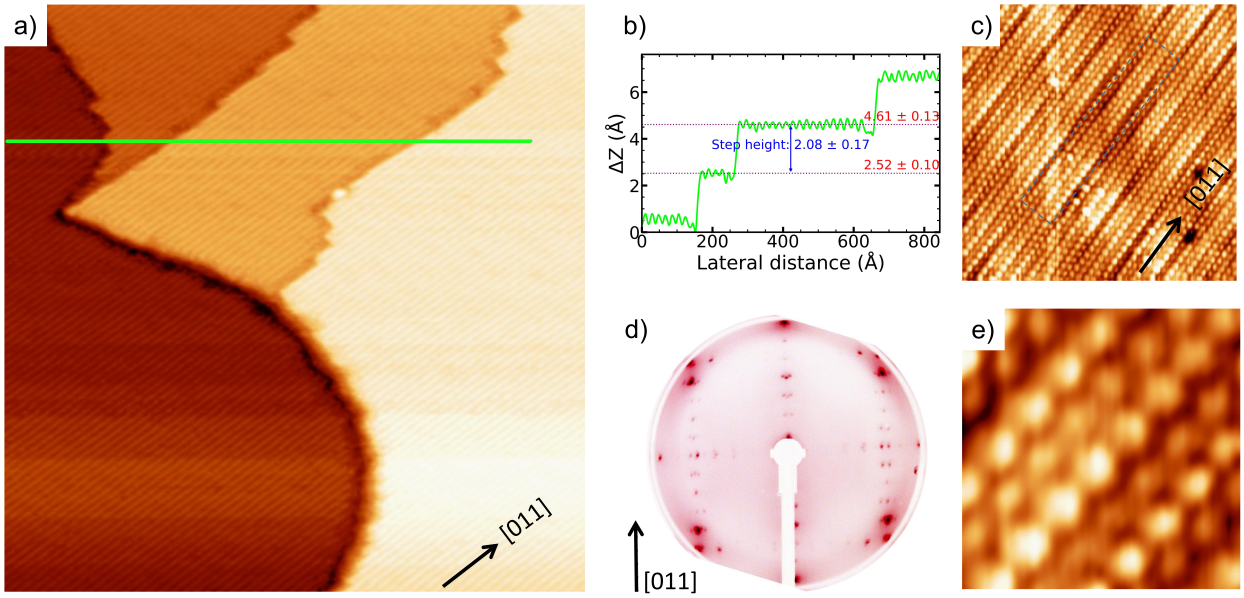


Figure 3.4: a) STM image of clean Au(100), $U_{\text{Bias}} = 0.1$ V, $I = 0.3$ nA (100×100 nm^2), b) Line profile drawn in (a), c) 26×5 reconstruction of Au(100) surface, $U_{\text{Bias}} = 0.1$ V, $I = 0.3$ nA (10×10 nm^2), d) LEED image of Au(100) at 63 eV, e) Hexagonal structure of the topmost layer of Au(100).

3.4 MBE (Molecular beam epitaxy)

In our experiments, we employed the TCE-BSC evaporator from Kentax GmbH [63] for the deposition of thin films using low sublimation temperature precursors. The evaporator, equipped with three crucibles, enables simultaneous deposition of multiple materials. Heating is provided by tungsten coils. The crucibles, each filled with a 40 mm^3 cube of precursor material, are mounted on a retractable mechanism. This mechanism enables the extension and retraction of the crucibles within the UHV environment, facilitating the exchange or replacement of crucibles without breaking the vacuum. Additionally, this setup provides precise control over the distance between the crucibles and the substrate, ensuring accurate film growth from sub-monolayer to multilayer regimes.

To fill the precursor molecules CsBr, $SnBr_2$ and $PbBr_2$ into the crucibles the entire evaporator was inserted into a glovebox under argon atmosphere (Micro- and Nanoanalytics Facility (MNaF)). This procedure prevents exposure to air or moisture of the sensitive molecules. Clean handling was ensured by using capillary funnels or folded aluminum foil, preventing contamination on the exterior surfaces of the crucibles. During crucible exchange,

care was taken to prevent damage to the quartz crucibles by applying only minimal force. A manually rotatable shutter was employed to control the exposure of the crucibles during deposition, allowing for the opening of one, two, or three crucibles as required for the specific experiment. Proper documentation of the crucible and shutter orientation was made to ensure repeatability in future runs.

After mounting the evaporator to the UHV system and completing the electrical connections according to the external connection diagram, K-type thermocouples were used to monitor the temperature of each crucible. During the initial start-up, a controlled temperature ramp was applied to avoid thermal shocks, ensuring the gradual sublimation of CsBr, $SnBr_2$, and $PbBr_2$ under vacuum conditions.

Cooling of the evaporator was achieved using a low-pressure water cooling system. A small bucket of water with approximately 3 liters was connected to the evaporator using silicon pipes. A small pump, operating at $U = 4\,\mathrm{V}$ and $I = 1\,\mathrm{A}$, circulated the water from the bucket through the evaporator. This setup ensured that the crucibles, which were not heated, did not exceed a temperature of 40 °C. The evaporator temperatures were controlled between 160 °C and 430 °C to match the sublimation temperatures of the precursors. Specifically, $SnBr_2$ was evaporated at 160 °C to 170 °C, while CsBr was evaporated at 420 °C to 430 °C. Heating was applied gradually to prevent sudden material expulsion. During the evaporation process, the pressure in the system increased to 1 to 2×10^{-9} mbar. The cooling system effectively prevented overheating of adjacent crucibles, especially when using materials with different sublimation temperatures.

Chapter 4

CsBr on gold surfaces

To synthesize $CsSnBr_3$ perovskite, molecular beam epitaxy is employed to deposit the precursor molecules CsBr and $SnBr_2$ onto a substrate maintained under ultra-high vacuum conditions. This technique has been widely used for lead-based perovskites, such as $CsPbBr_3$ [23], formed by co-depositing CsBr and $PbBr_2$. Investigating the growth behavior of individual precursor molecules is crucial for optimizing deposition parameters and is also scientifically intriguing in its own turn.

4.1 CsBr on Au(111)

The precise determination of the deposition rates on Au(111) is essential for the accurate interpretation of our experimental data. Given the scarcity of prior studies on this system, our investigation offers also valuable insights into the growth and epitaxial relationships between CsBr and the Au(111) substrate.

The growth of CsBr on the Au(111) surface was examined using STM and LEED. To prepare the Au(111) single crystal, it underwent sputtering with argon ions (1.5 keV, 10^{-5} mbar) followed by annealing at 500°C in a 10^{-10} mbar vacuum until the formation of a reconstructed Au(111)-$(22 \times \sqrt{3})$ surface was confirmed using LEED, after which the Au(111) crystal was transferred to the deposition chamber for CsBr deposition.

CsBr was sublimated at the temperature of 425°C onto the cleaned Au(111) substrate held at room temperature for 1, 2, and 5 minute durations. QCM showed a deposition rate of (0.065 ± 0.012)Å/min. The QCM sensor was not placed directly in front of the sample, in order to measure the flux during deposition. Through the correlation of the observed coverage and measured flux, the correct deposition rate can be determined.

Figure 4.1 a) shows an STM image of CsBr deposited on Au(111) after 1 minute. CsBr islands can be distinguished by their edges, which form 90° angles, in contrast to the less regular edges of the Au(111) surface. These structures predominantly appear near the step edges, showing that growth starts from the step edges. Additionally, the herringbone reconstruction of the Au(111) surface is modified, forming a stripe pattern beneath the CsBr

islands, which is attributed to the strain exerted on the gold surface by, in this case, the CsBr islands, as noted in previous studies for Au(111) [64–66].

Figure 4.1 d) displays a line profile indicating the distinct heights of CsBr and gold steps, with CsBr step heights measuring d_1 and d_3 as (1.6±0.1)Å and gold steps measuring d_1+d_2 as (2.6 ± 0.1)Å. The LEED image (Figure 4.1 g) shows faint middle spots corresponding to the CsBr domains and outer hexagonal spots are from the gold substrate with the reconstruction still visible.

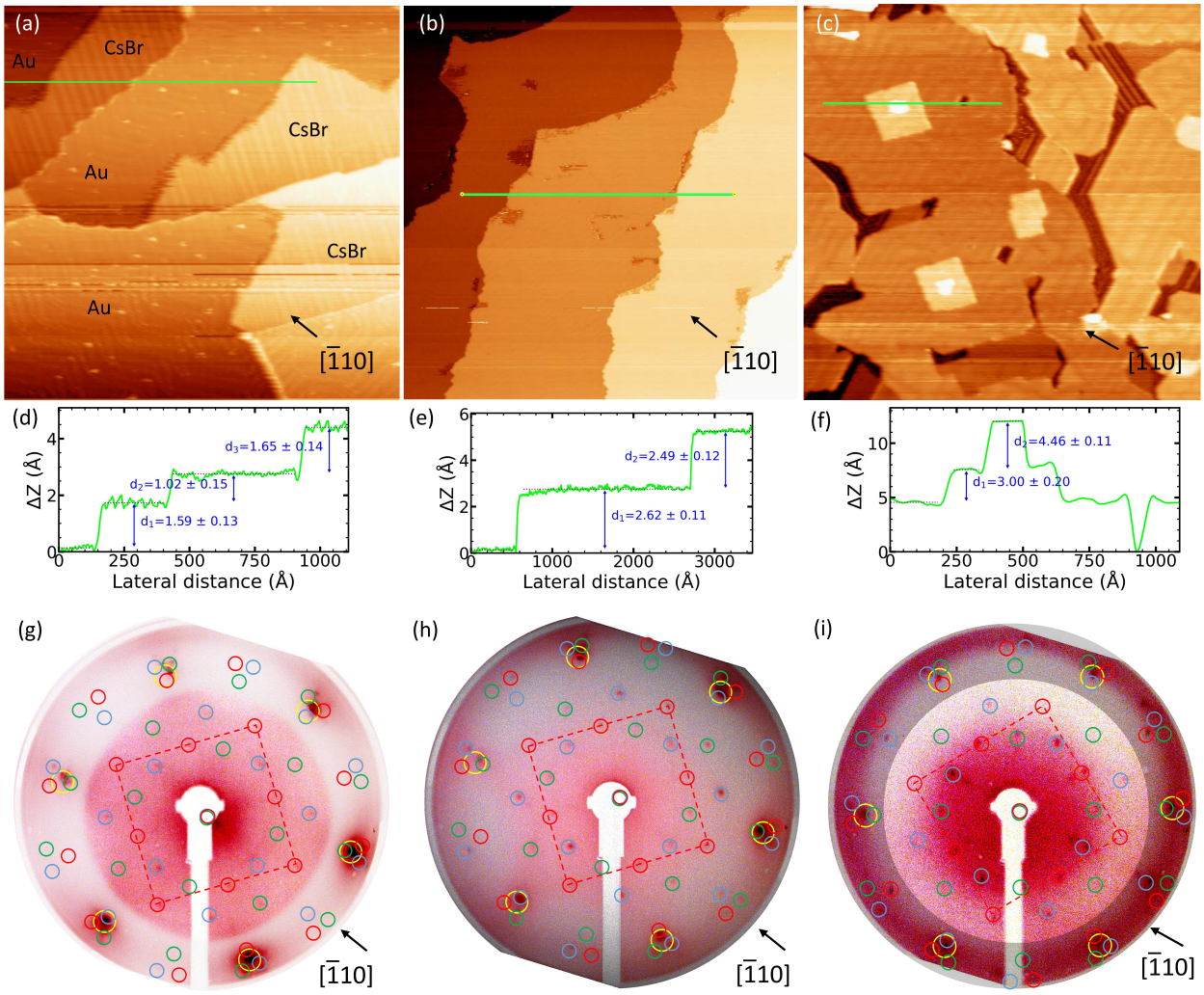


Figure 4.1: (a) STM image of 0.5 ML CsBr on Au(100) ($U_{\text{bias}} = 2$ V, $I = 0.02$ nA, 125×125 nm^2). (b) STM image of ≈ 1 ML CsBr on Au(111) ($U_{\text{bias}} = 2$ V, $I = 0.06$ nA, 500 × 500 nm^2). (c) STM image of 2.5 ML CsBr on Au(111) ($U_{\text{bias}} = 5$ V, $I = 0.01$ nA, 250 × 250 nm^2). (d-f) Line profiles corresponding to the drawn profiles in (a-c). (g-i) LEED images corresponding to (a-c) at 57 eV. The black arrow indicates the crystallographic direction of the underlying Au(111) substrate, specifically the [1̄10] direction. In LEED images (g) and (i) the contrast has been partially enhanced, allowing the weaker CsBr spots to be more visible.

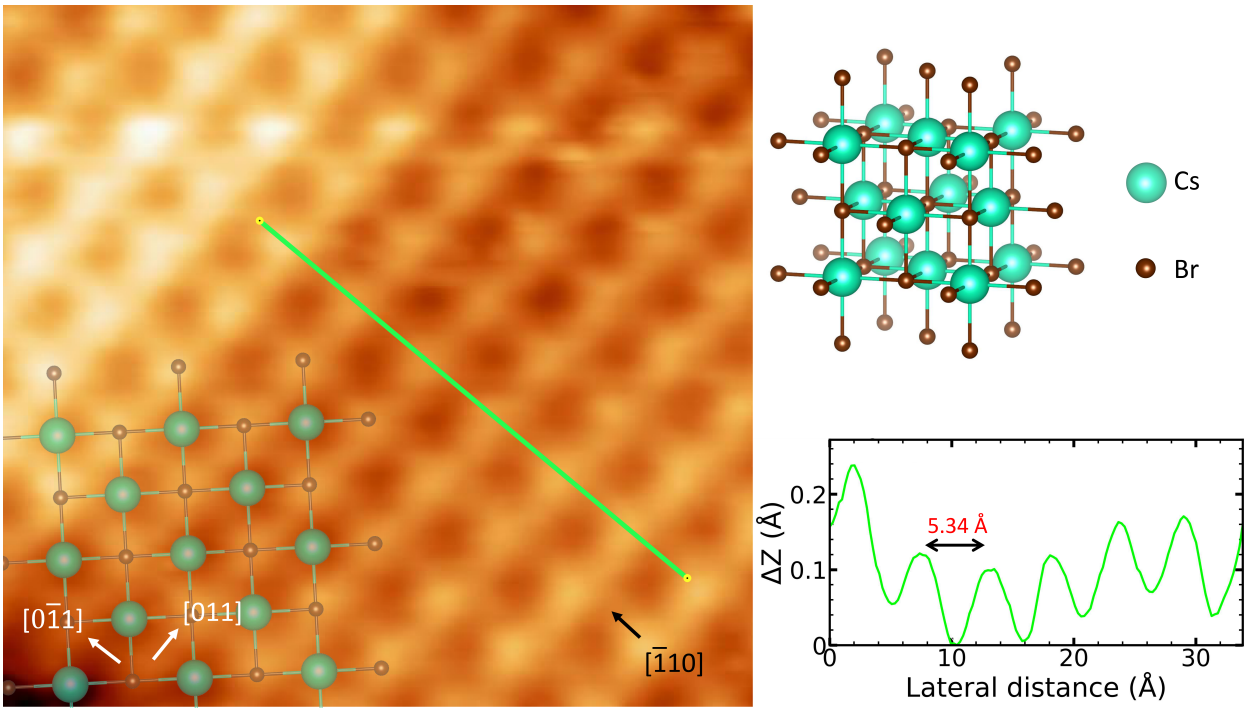


Figure 4.2: Left panel: STM image of CsBr on Au(111) ($U_{\text{bias}} = 2$ V, $I = 0.02$ nA, 5×5 nm^2). The image shows periodic protrusions representing Br atom positions. The overlaid lattice shows Cs (green) and Br (brown) atoms. The black arrow marks the [$\bar{1}$10] crystallographic direction of the gold substrate. The white arrows marks the [011] and [0$\bar{1}$1] crystallographic direction of CsBr. Right panel: Ball-and-stick model of CsBr showing Cs and Br atom positions [27]. Below, a line profile graph along the green line in the STM image shows height (ΔZ) vs. distance, with periodic peaks corresponding to Br atom positions and atomic spacing.

Figure 4.1 b) shows an STM image of CsBr deposited on Au(111) after a 2-minute deposition. Unlike the shorter deposition duration, where CsBr islands were visible, this image reveals the formation of a full monolayer of CsBr, with no discernible islands present. The uniform growth indicates that the deposition conditions for this duration favor layer-by-layer growth rather than pyramids. Additionally, the LEED pattern for the 2-minute deposition, shown in Figure 4.1 h), displays clearer evidence of the three distinct domains of CsBr. One of these domains is marked with a red square in the figure, further confirming the ordered epitaxial growth of CsBr on the Au(111) substrate. The lattice constant of CsBr can be found as (5.3 ± 0.2)Å from this LEED image which matches with rock-salt CsBr [67].

Figure 4.1 c) shows an STM image of CsBr deposited on Au(111) for 5 minutes. The results indicate multilayer growth of CsBr on the Au(111) surface, with clear evidence of stacked layers. The LEED pattern corresponding to this deposition, shown in Figure 4.1 i), further confirms the structure. The step heights of the top CsBr layers appear to be larger and are more consistent with the step height of the rock-salt structure, as expected for thicker CsBr films.

The 1-minute deposition resulted in the formation of approximately 0.5 monolayers of CsBr on the Au(111) substrate. The 2-minute deposition produced nearly a complete monolayer, while the 5-minute deposition, based on this calibration, can be estimated to have resulted in the growth of approximately 2.5 monolayers.

While CsBr in bulk adopts a CsCl structure, as previously reported [68], thin films of CsBr preferentially form a rock-salt structure, consistent with earlier findings [69, 70]. This rock-salt CsBr is an ionic crystal with cubic symmetry, composed of positively charged cesium ions (Cs^+) and negatively charged bromide ions (Br^-) . Each Cs^+ ion is surrounded by six Br^- ions and vice versa, optimizing the contact between opposite charges (Figure 4.2 right panel).

Figure 4.2 provides a detailed atomic-level view of CsBr on the Au(111) substrate. In the left panel, an STM image of CsBr on Au(111) is shown. It shows square pattern as expected for (100) plane of interpenetrating fcc structure of CsBr. Periodic protrusions correspond to the positions of bromine (Br) atoms [71]. The overlaid lattice in the image highlights the positions of cesium (Cs) atoms in green and bromine (Br) atoms in brown. In the right panel, a ball-and-stick model of rock-salt CsBr shows the atomic positions of Cs and Br. Below this, a line profile graph, taken along the green line in the STM image, presents the height (ΔZ) versus distance. The top left of the STM image appears to be higher which is due to the stripe reconstruction line of the gold substrate. The periodic peaks in the line profile are consistent with the Br atom positions (5.3 ± 0.2Å), providing further confirmation of the atomic spacing. This detailed view confirms the epitaxial relationship between the CsBr thin film and the Au(111) substrate, and illustrates the atomic arrangement of CsBr in this configuration. For the calibration factor we can estimate $6 \pm 2\,\mathrm{ML/Å}$ which means multiplication of this value with the QCM reading gives the number of monolayers per minute as the deposition rate.

4.2 CsBr on Au(100)

Introducing CsBr on Au(100) is from a structural perspective due to the complex reconstruction of the Au(100) surface. The Au(100) surface presents a hexagonal topmost layer with quasi-one-dimensional (1D) features confined within the reconstruction fringes [62]. The periodicity of the reconstructed Au(100) surface could affect the growth and arrangement of CsBr, potentially leading to new superstructures or altered surface characteristics. Studying such a system could enhance our understanding of how adsorbates like CsBr interact with complex surface reconstructions, showing the way for tunable material properties.

Studying the growth of CsBr is also the starting point for understanding perovskite growth on Au(100). As mentioned earlier, bulk CsBr crystals have the CsCl structure, but thin films can adopt the rock salt structure on various substrates. Understanding interfaces is crucial for nanoelectronics device development.

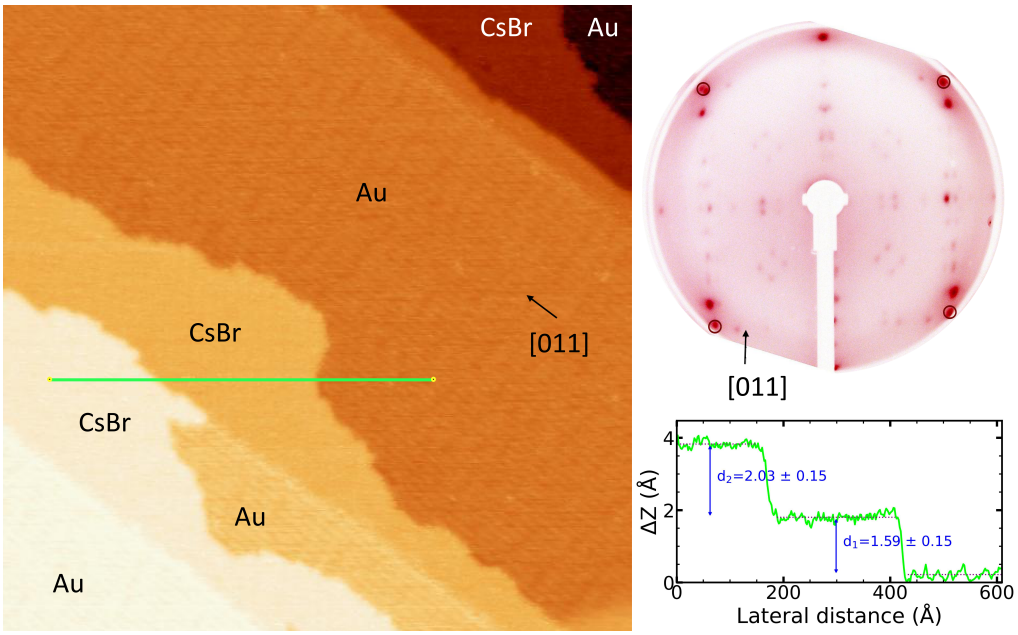


Figure 4.3: (a) STM image of 0.5 monolayer (ML) of CsBr on Au(100), with $U_{\text{bias}} = 2$ V and $I = 0.02$ nA, 100×100 nm^2. (b) LEED image of CsBr on Au(100) taken at an energy of 57 eV.

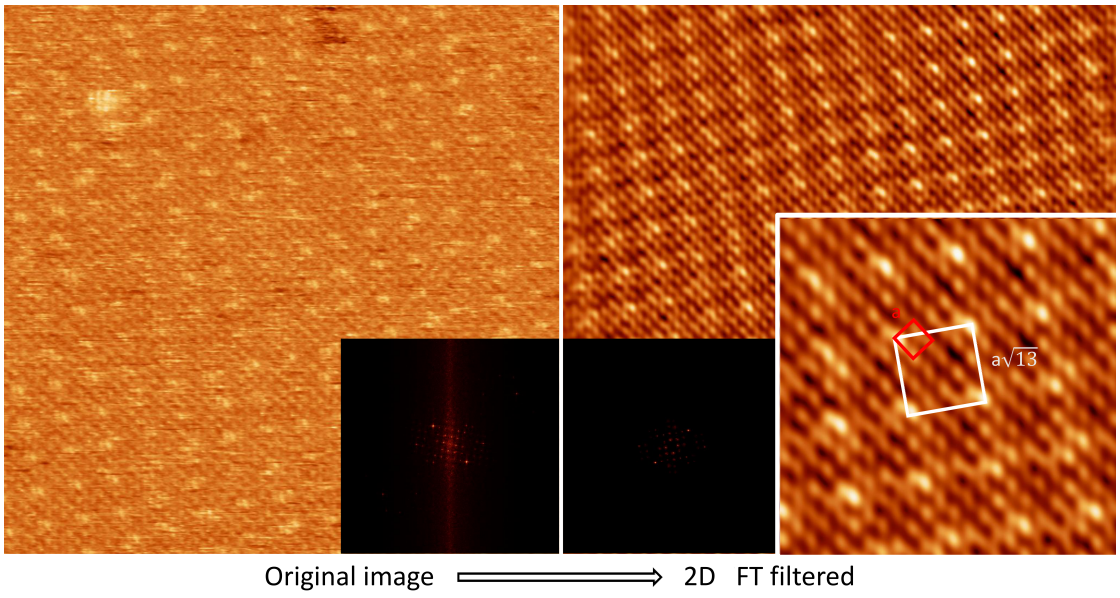


Figure 4.4: Left image: STM image of 0.5 monolayers (ML) of CsBr on Au(100), $U_{\text{bias}} = 2\,\text{V}$ and $I = 0.02\,\text{nA}$, with an image size of $28.7 \times 28.7\,\text{nm}^2$. Right image: 2D FT filtered image, reconstructed by inverse Fourier transform using the selected spots in the corresponding 2D FT image shown in the insets. Additional superstructure was characterized by an angle of $\tan^{-1}\left(\frac{2}{3}\right) \approx 33.69°$, and a factor $\sqrt{13} \approx 3.6$, respect to the CsBr lattice.

CsBr and Au(100) were prepared in UHV. Au(100) was cleaned by Ar^+ sputtering and annealing cycles. CsBr was sublimated from a heated quartz Knudsen cell. Deposition rates were current controlled and monitored.

STM imaging for negative and positive biases idest for filled and empty states showed no difference in the imaging. At 0.5 ML coverage, CsBr showed island growth on the step edges of Au(100)(Figure 4.3). Substrate steps and CsBr island edges could be distinguished. Step heights of CsBr layers were measured as 1.6 ± 0.1 Å and 2 ± 0.1 Å for the CsBr layer and Au(100) steps, respectively. Step height measurements were similar for both filled and empty state images. Measured island heights were lower than expected for either rock salt or CsCl structures. The decrease in island heights is attributed to CsBr's insulating behavior.

Atomically resolved images showed a square pattern, suggesting the (001) face of CsBr. Bright features were attributed to Br atoms (anions). The inter-atomic distance of 5.23 Å matched the expected distance for the rock salt structure. Additional super structure was also observed as the angle given by $\tan^{-1}\left(\frac{2}{3}\right) \approx 33.69°$ and the factor given by $\sqrt{13} \approx 3.6$ with respect to CsBr which can also be observed in LEED image. Since the measurement done at room temperature, 2D FT filtering was needed to see the structure (Figure 4.4). The structure can be seen better at low temperature [72].

Chapter 5

$SnBr_2$ on gold surfaces

Tin(II) bromide ($SnBr_2$) is of significant interest in the realm of optoelectronics, particularly due to its role in perovskite structures such as $CsSnBr_3$. This section explores the atomic-scale interactions of $SnBr_2$ with two distinct gold surfaces, Au(111) and Au(100), offering insights into how crystallographic orientation influences film growth, structure, and electronic properties at the interface.

The hexagonal structure of Au(111) provides a well-characterized platform for studying epitaxial growth. Here, we investigate how $SnBr_2$ interacts with this surface, focusing on the disappearance of the characteristic herringbone reconstruction, the formation of new atomic structures, and the dynamics of growth at different coverages. Our experiments, conducted using STM and LEED, document the evolution from initial nucleation to the establishment of stable layers, highlighting potential phase segregation or dissociation phenomena.

In contrast, the Au(100) surface, with its square lattice, presents a different scenario for $SnBr_2$ deposition. This study delves into the adaptation of $SnBr_2$ to the square-like symmetry of Au(100), examining how this interaction leads to unique structural patterns, changes in surface morphology, and the impact on gold's surface reconstruction. The use of STM under ultra-high vacuum conditions allows for atomic-resolution imaging, capturing the dynamic processes like island formation and dissolution, which are indicative of the material's behavior at the interface.

Both sets of experiments are crucial for understanding the growth mechanisms of $SnBr_2$ on gold surfaces, which are pivotal for optimizing the fabrication of perovskite-based devices. By comparing and contrasting the behaviors on these two surfaces, we aim to provide a comprehensive view of $SnBr_2$'s growth dynamics, its potential for controlling electronic properties, and its implications for the development of novel optoelectronic technologies.

5.1 $SnBr_2$ on Au(111)

Tin(II) bromide ($SnBr_2$) is a yellow powder, possessing a density of 5.12 g/cm^3 and a melting point of 215 °C [73]. Its structure and bonding exhibit interesting characteristics. In the gas phase, $SnBr_2$ adopts a bent configuration with a Br-Sn-Br angle of 95° and a Sn-Br

bond length of 255 pm, and there is evidence for dimerization [74, 75]. In the solid state, $SnBr_2$ forms $(SnBr_2)_\infty$ chains, with the tin atoms surrounded by five bromine neighbors in a trigonal bipyramidal configuration [76]. Two polymorphs exist: an orthorhombic form stable at room temperature and a hexagonal form stable at higher temperatures. Both polymorphs feature the same chain-like $(SnBr_2)_\infty$ structure but differ in their packing arrangements [77].

Here the focus is on the atomic structure of ultra-thin $SnBr_2$ films on Au(111) substrates, grown using MBE. Characterization was performed using STM and LEED. The Au(111) substrate was cleaned by annealing and Ar^+ sputtering cycles. $SnBr_2$ was sublimated from a heated quartz Knudsen cell at a deposition rate of ~ 1 ML/min according to the comparison of the QCM readings and STM images of CsBr films.

Figure 5.1 represents the results of a 0.5-minute deposition of $SnBr_2$ on clean Au(111), with an evaporation temperature of $SnBr_2$ at 169 °C. Immediately after the deposition, it can be seen that the herringbone reconstruction of Au(111) is gone. It was tricky to identify what structure formed and at what coverage. In Figure 5.1 (b), we can partially see the herringbone reconstruction, and in Figure 5.1 (c), it can be seen even more clearly, with accumulations on the herringbone elbows. Occasionally, islands can be seen in Figure 5.1 (d), and by the height profile shown in Figure 5.1 (f), it can be assumed that gold is underneath the deposited structure. Figure 5.1 (e) is a zoomed-in area of (c), where it was not possible to resolve the structure clearly but the height of 1.65 Å was measured. In Figure 5.2, a 1-minute deposition of $SnBr_2$ on Au(111) can be seen. Figure (d) is the LEED image, and as expected, the herringbone reconstruction is gone, with only gold spots visible. Figures 5.2 (b) and (c) are zoomed images of areas similar to (a). In Figure 5.2(b), a hexagonal structure can be observed with a corrugation of approximately 0.7 Å, considering the holes. The lattice constant of the hexagonal structure is 5.6 Å. In Figure 5.2(c), alongside the hexagonal structure, protrusions can be seen with a height of around 2 Å. The protrusions tend to cluster and attempt to form a honeycomb structure with lattice constants of approximately 10.4 Å.

In Figure 5.3, a 2-minute deposition of $SnBr_2$ on Au(111) is shown. In this figure, two types of structures can be measured, with lattice constants of approximately 5.9 Å and 3.2 Å.

In Figure 5.4, a 10-minute deposition of $SnBr_2$ on Au(111) is shown. At this high coverage, a $\sqrt{3} \times \sqrt{3}\,R30°$ structure can be observed in the LEED image presented in Figure 5.4 (d). The STM images reveal triangular-like structures with side length of 50 to 200 Å. Figure 5.4 (e) indicates that the corrugation of the structure is around 1 Å. In Figure 5.4(b), the measured step height can be assigned to the Au(111) step, as shown in Figure 5.4(f). Figure 5.4(c) provides a closer look of a chain-like structure, while Figure 5.4(g) displays the profile drawn from (c), illustrating a distance between the protrusions of the individual chain-segments of 8.4 Å.

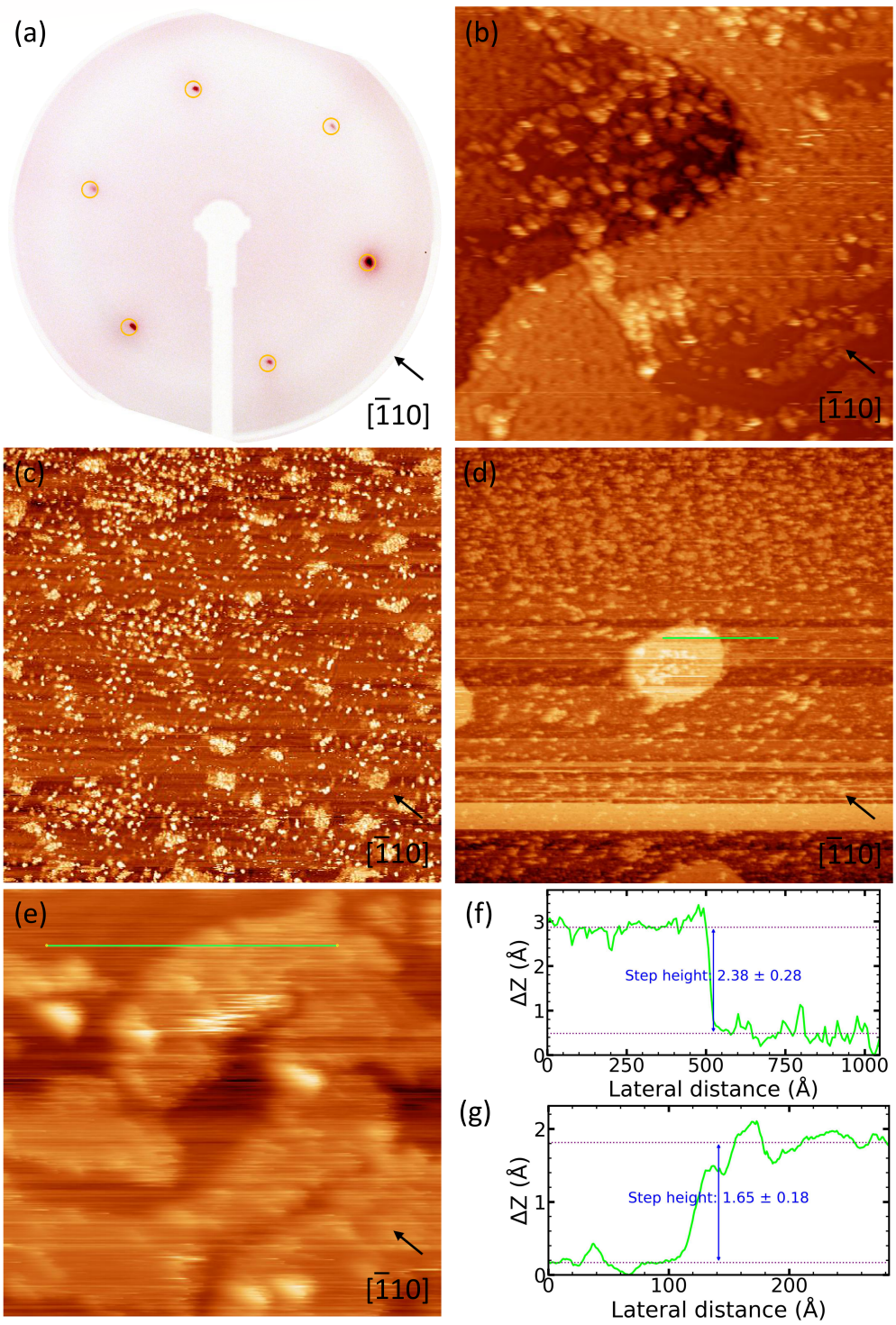


Figure 5.1: (a) LEED image of low coverage $SnBr_2$ on Au(111) at 81 eV. (b-e) STM images of $SnBr_2$ on Au(111) with image sizes of 100 nm × 100 nm, 200 nm × 200 nm, 400 nm × 400 nm, and 43 nm × 43 nm, respectively, and tunnelling conditions: (b) $U_{\text{bias}} = 2$ V, $I = 0.1$ nA; (c) $U_{\text{bias}} = 2$ V, $I = 0.2$ nA; (d) $U_{\text{bias}} = -3$ V, $I = 0.2$ nA; (e) $U_{\text{bias}} = -1$ V, $I = 4$ nA. (f) Height profile from (d), (g) height profile from (e).

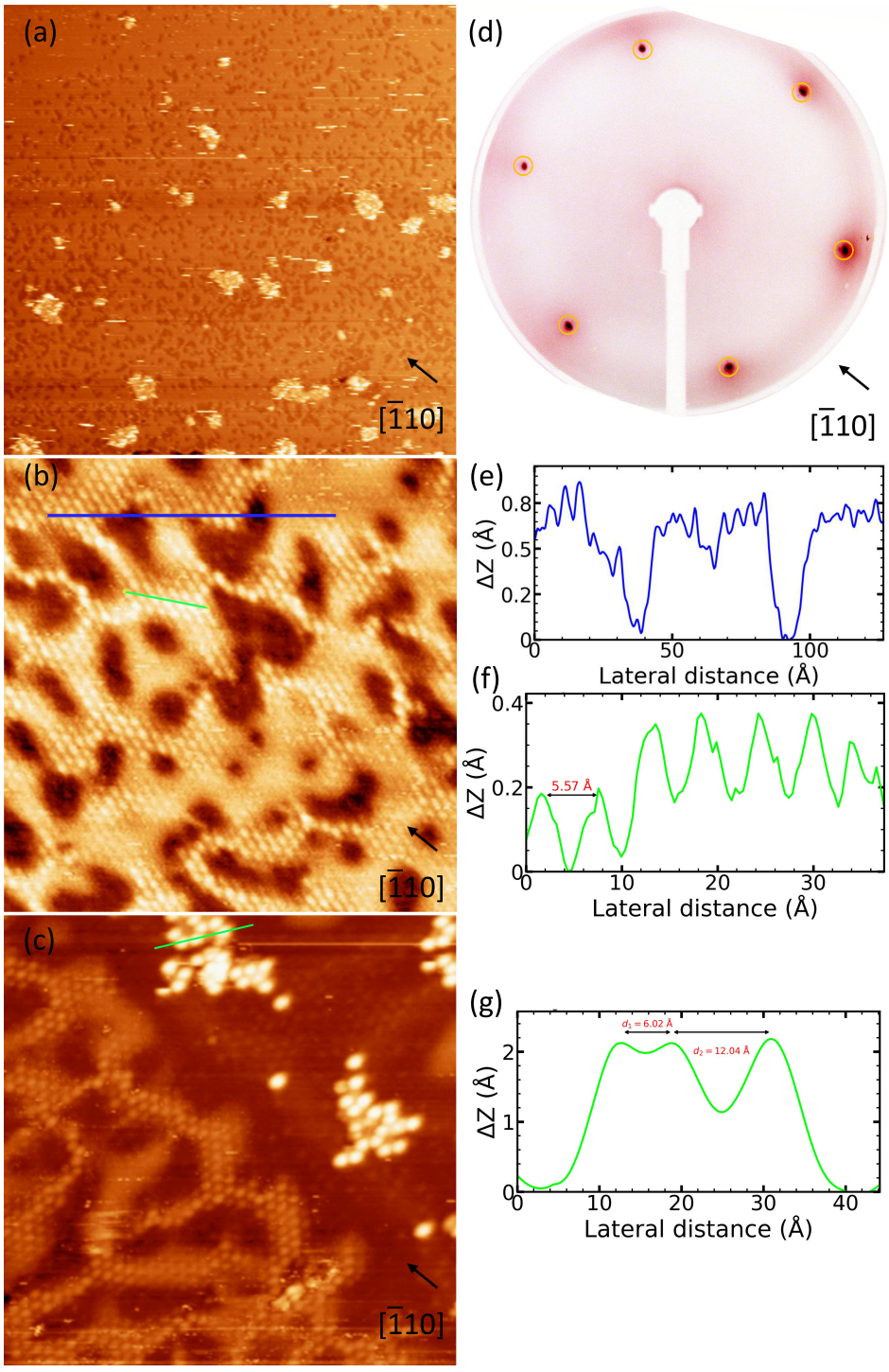


Figure 5.2: (a) STM image of $SnBr_2$ on Au(111) at $U_{\text{bias}} = 2\,\text{V}$ and $I = 0.07\,\text{nA}$, with an image size of $121\,\text{nm} \times 121\,\text{nm}$. (b) STM image of $SnBr_2$ on Au(111) at the same bias and current, with an image size of $20\,\text{nm} \times 20\,\text{nm}$. (c) Another STM image of $SnBr_2$ on Au(111) at $U_{\text{bias}} = 2\,\text{V}$ and $I = 0.07\,\text{nA}$, also with an image size of $20\,\text{nm} \times 20\,\text{nm}$. (d) LEED image of $SnBr_2$ on Au(111) taken at an electron energy of 53 eV. (e) and (f) Blue and green profile lines drawn in (b). (g) Profile line from (c).

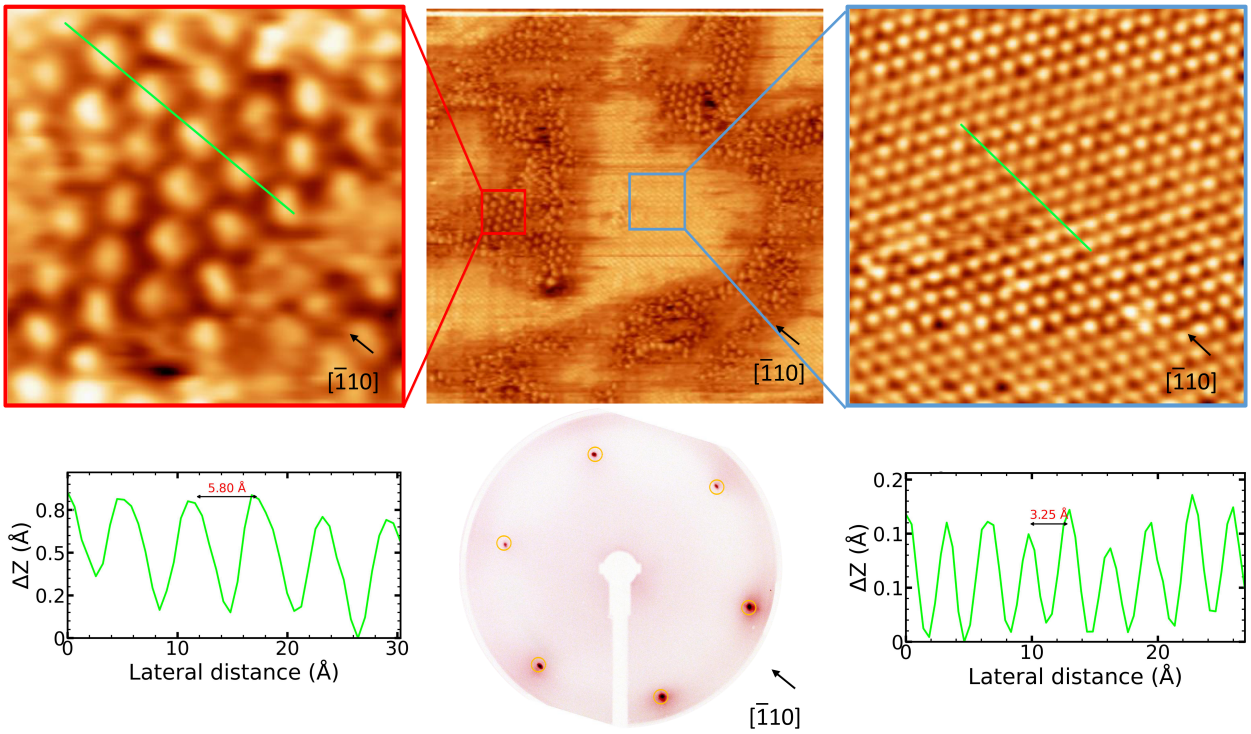


Figure 5.3: Top middle is the STM image of $SnBr_2$ on Au(111) at $U_{bias} = -1\,V$ and $I = 5\,nA$, $25\,nm \times 25\,nm$. The top left and top right images are zoomed and filtered areas from the top middle STM image. The bottom left and bottom right images show the corresponding profiles drawn in the left and right images, respectively. The bottom middle image is the LEED image of $SnBr_2$ on Au(111) taken at an electron energy of 56 eV.

An interpretation of the observed structures is difficult. From XPS studies (see Chapter 8) it can be confirmed that the adsorbed species are Sn and Br. Further, the XPS data shows that the $SnBr_2$ can dissociate into Sn and Br, when adsorbed at the surface. Therefore, structures can be either pure Sn, pure Br or a combination of Sn and Br (e.g. $SnBr_2$). In literature several mostly theoretical studies have been done for these and related elements. For example, Naik et al. [78] used density functional theory to investigate the structural, electronic, and optical properties of $SnBr_2$ monolayers. Their study revealed the stability of the monolayer and its promising electronic band strcuture for 2D material applications. Bandgap calculations indicated that the monolayer exhibited semiconducting properties with tunable characteristics. The authors discussed how the inert-pair effect contributes to the stability of Sn in the monolayer.

Gao et al. [79] explored the adsorption of chlorine, which is an halide as Br, on Au(111) surfaces to understand surface modifications at the atomic level. They examined whether the adsorption resulted in chlorine overlayers or surface chlorides, using experimental and theoretical techniques. Their findings demonstrated that chlorine interacts strongly with Au(111), forming well-defined structures. The study highlighted the role of temperature and surface preparation in influencing chlorine adsorption behavior. The authors discussed

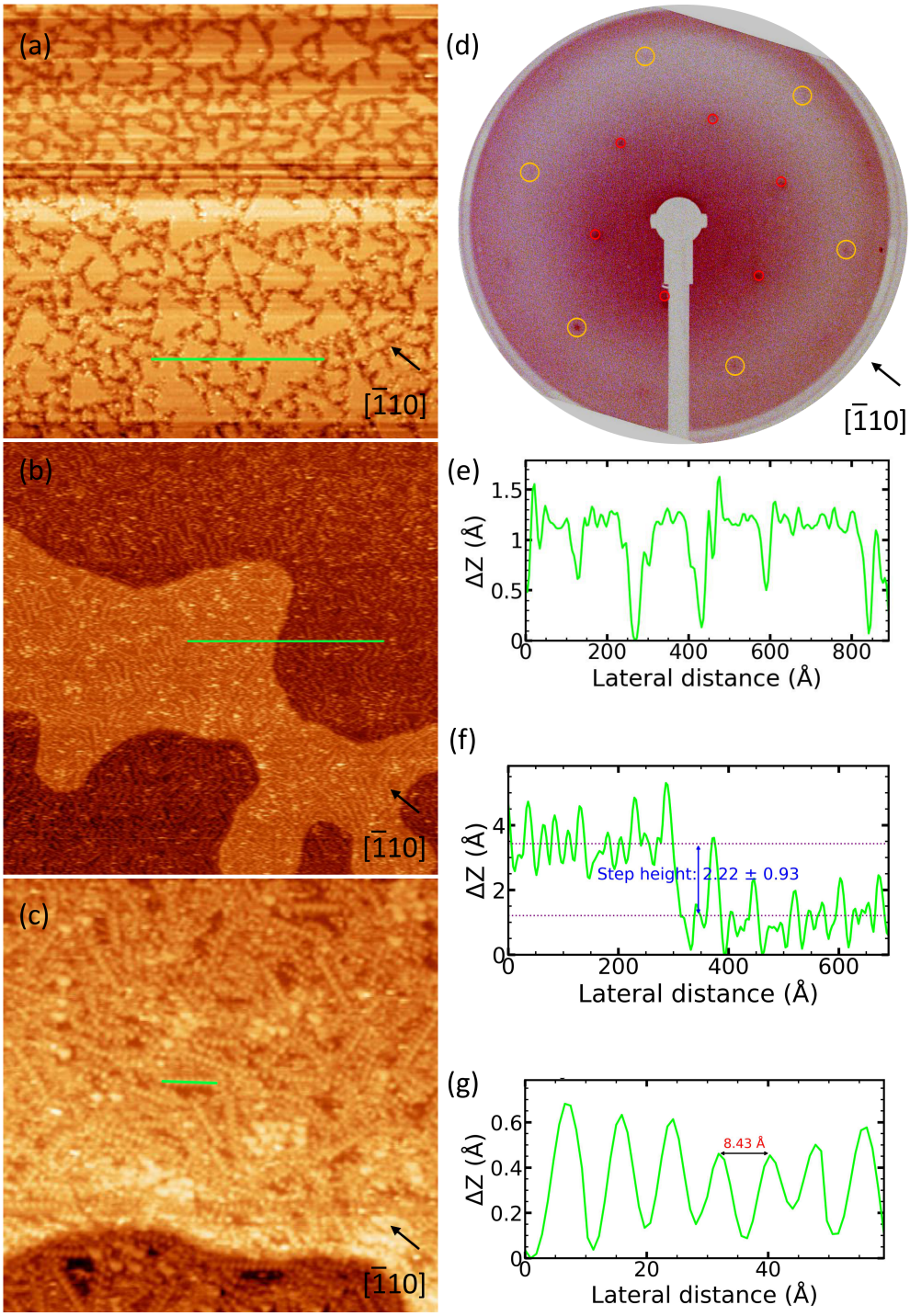


Figure 5.4: (a), (b), and (c) are the STM images of $SnBr_2$ on Au(111). Image size of 220 nm × 200 nm with $U_{\text{bias}} = 2\,\text{V}$ and $I = 0.01\,\text{nA}$. Image (b) size of 155 nm × 155 nm with $U_{\text{bias}} = 1\,\text{V}$ and $I = 0.5\,\text{nA}$. Image (c) size of 50 nm × 50 nm with $U_{\text{bias}} = 1\,\text{V}$ and $I = 0.5\,\text{nA}$. The profiles (e), (f), and (g) are drawn respectively from images (a), (b), and (c). Image (d) is the LEED image of $SnBr_2$ on Au(111) taken at an electron energy of 62 eV.

the implications of chlorine-induced changes for catalytic processes on gold surfaces. Their results provided a model for understanding halogen interactions with noble metal surfaces.

Yuan et al. [80] presented a study on the direct growth of SnI_2 monolayers using van der Waals epitaxy. The research focused on the synthesis and characterization of this novel 2D material. SnI_2 monolayers were found to exhibit high crystallinity and stability under ambient conditions. The study discussed the challenges of achieving uniform growth and maintaining monolayer quality.

Meier et al. [81] investigated the spontaneous deposition of tin on Au(111) surfaces using in situ STM. Their study provided insights into the initial stages of tin layer formation on noble metal surfaces. The results revealed the formation of distinct surface structures depending on deposition parameters. Tin atoms were observed to self-assemble into well-ordered arrangements at submonolayer coverage.

Yet, a clear interpretation remains open at this point. One can speculate that the chain-like structures observed in Figure 5.4 c originate from ($SnBr_2$)-chains [76] and the hexagonal structure observed at higher coverages belongs to $SnBr_2$ layers.

5.2 $SnBr_2$ on Au(100)

$SnBr_2$ powder was deposited on the cleaned Au(100) surface under the same conditions as used for Au(111). Understanding interface properties is essential for device performance and the investigation of growth processes for $CsSnBr_3$.

Figure 5.5 shows a 1.5-minute deposition of $SnBr_2$ on Au(100). Figure 5.5 a is the STM image of the deposition, which illustrates the step height of Au(100), as can be seen in Figure 5.5 d, the profile drawn from image (a). One can see discontinuous disordered structures of similar height with a coverage of close to one monolayer. The apparent height of the adlayer varies between 0.4 and 1.0 Å. The step-height of the large terraces are assigned to monolayer high gold steps.The LEED image in Figure 5.5 c, which is rotated by 45 degrees with respect to the STM image, shows that the Au(100) reconstruction is lifted and a square pattern emerges, with the lattice constant of the unreconstructed Au(100) surface. This indicates that the adsorption of $SnBr_2$ strongly modifies the Au(100) surface. In Figure 5.5 b, a zoomed-in image of the structure can be seen, Local order with a square structure is present, where the distances between the protrusions is about 8 Å.

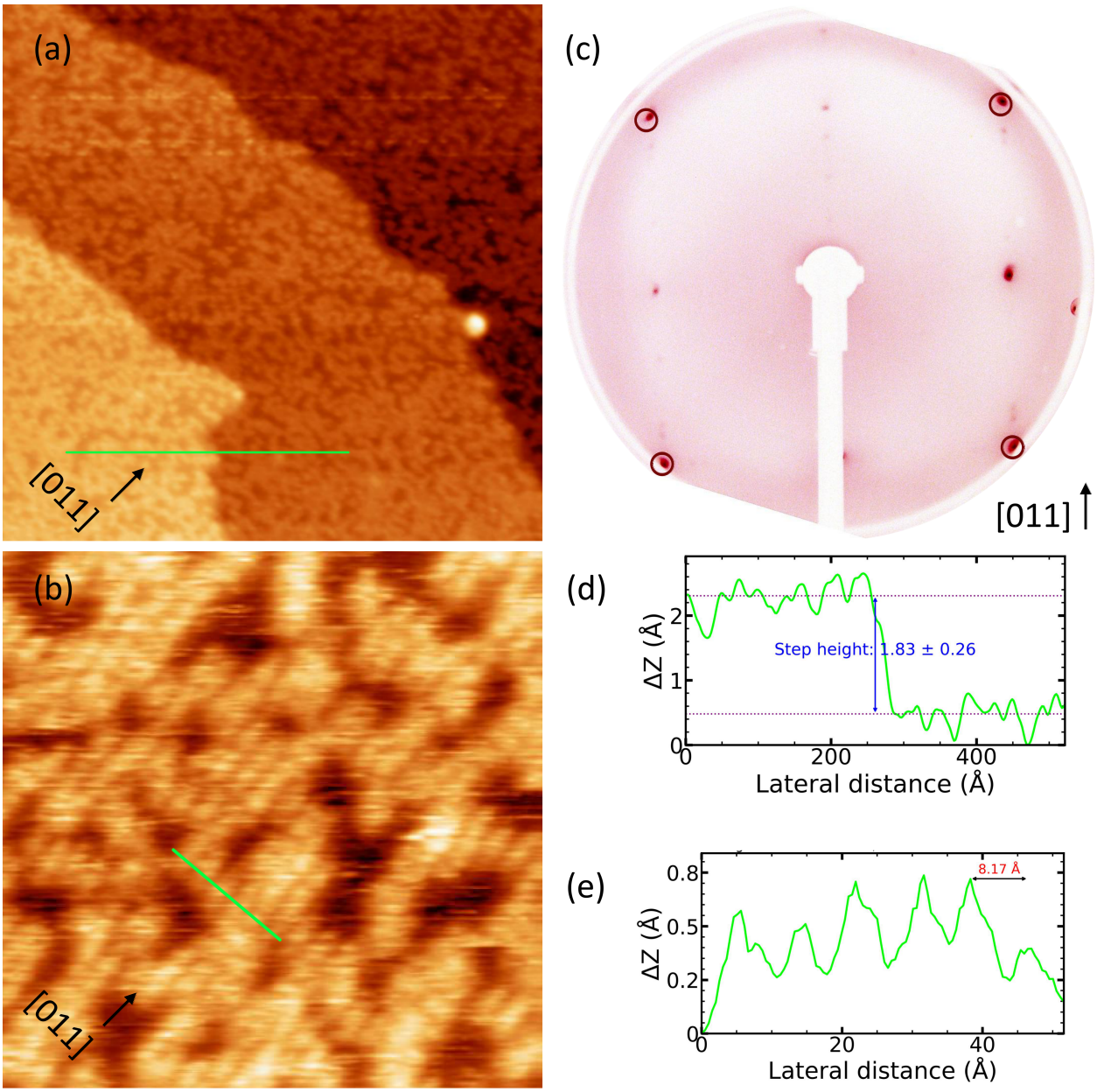


Figure 5.5: (a) STM image of $SnBr_2$ on Au(100), with $U_{bias} = 1$ V and $I = 0.3$ nA, 100 × 100 nm^2. (b) STM image of $SnBr_2$ on Au(100), with $U_{bias} = 1$ V and $I = 0.3$ nA, image size of 20 × 20 nm^2. (c) LEED image of $SnBr_2$ on Au(100) taken at an electron energy of 57 eV. (d) and (e) line profiles drawn in (a) and (b).

Figure 5.6 presents a 5-minute deposition of $SnBr_2$ on Au(100). A smooth film is now observed with an island with a height of 1.94 Å.The sequence of STM images reveals the dynamic evolution of an island on Au(100) surface at room temperature. Subsequent images (panels b-d) demonstrate the gradual diffusion and dissolution of the island, characterized by a reduction in size and blurring of the island edges. Ultimately, the island completely disappears (panels e-f), leaving smooth surface. This behavior indicates significant mobility

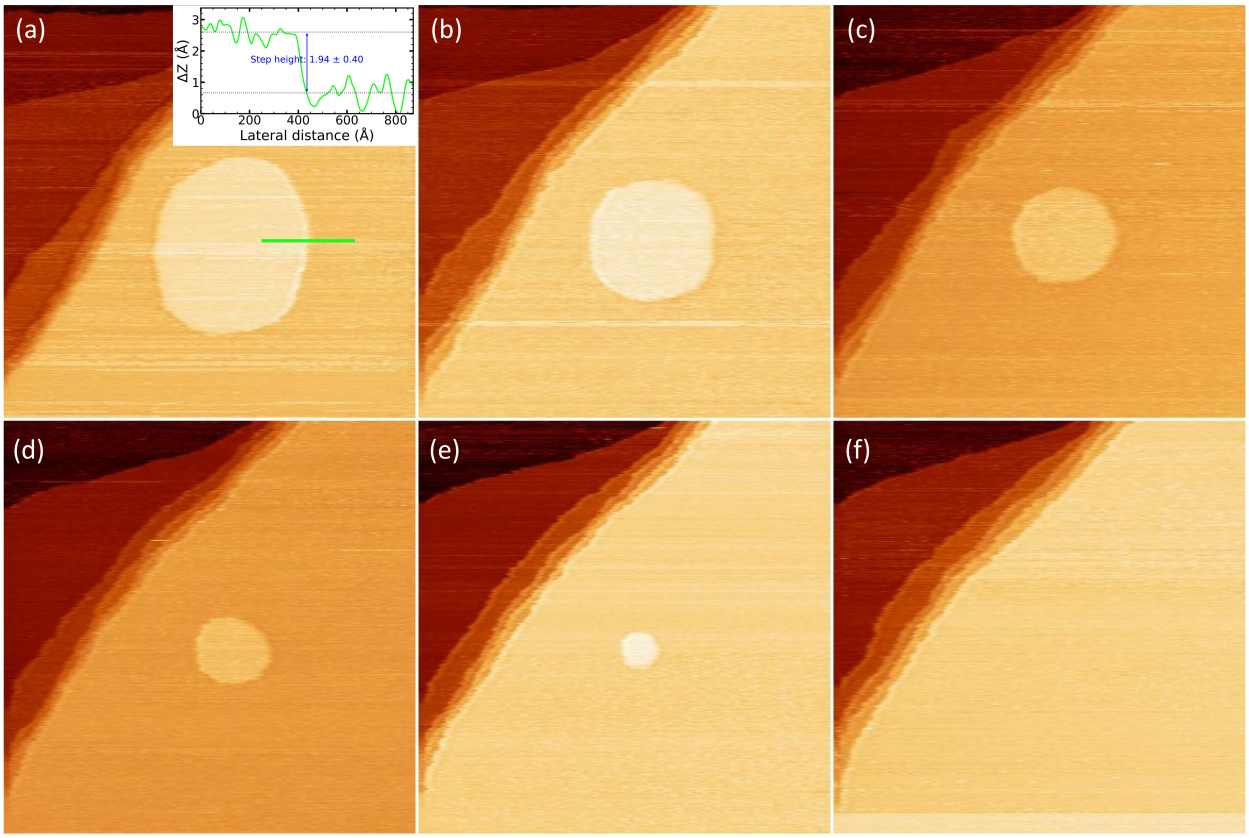


Figure 5.6: (a-f) STM image of $SnBr_2$ on Au(100), with $U_{\text{bias}} = 1.5$ V and $I = 0.1$ nA, 273 $\times$ 273 nm^2. The profile drawn in (a) shows the height of the disappeared island.

of $SnBr_2$ on the surface of Au(100) at room temperature. Due to its similar height with gold steps the island can also be assigned to a gold island, where the gold atoms gradually diffuse into nearby regions. Interestingly, when the STM tip moved to not scanned area, this type of islands can be found again and as the scanning continues one can observe the disappearing of the island in the same way, suggesting that the energy provided by the applied tunneling voltage can trigger this process.

Chapter 6

$CsSnBr_3$ on Au(111)

6.1 Submonolayer coverage and more

The goal of this subsection is to achieve the growth of cesium tin bromide perovskite by identifying the optimal deposition conditions. The growth stages and ideal conditions for perovskite formation were examined through the co-deposition of CsBr and $SnBr_2$ on Au(111). The deposition ratios (temperatures of the precursors) and durations were systematically varied, and the structural evolution of the precursors on Au(111) was analyzed. Interestingly, the deposition process resulted in the emergence of diverse surface structures that were identified as novel structural outcomes, providing valuable insights into the growth mechanisms of perovskite films and highlighting the significant influence of deposition parameters on surface morphologies.

The first sample was prepared by co-depositing CsBr and $SnBr_2$ onto an Au(111) substrate. CsBr was deposited at 425°C with a QCM rate of 0.07 Å/min, while $SnBr_2$ was deposited at 168°C with a QCM rate of 0.07 Å/min. The deposition rate was measured with only one shutter open at a time. The deposition lasted for 0.5 minutes at room temperature. Figure 6.1, (a) shows an STM image of this deposition resulting in submonolayer coverage. One can see small clusters around the elbow sites of the herringbone reconstruction and larger regular islands at step-edges. The step height d_1 is close to the Au(111) step-height, whereas d_2 is the step-height of the island with a value of 3 ± 0.5 Å. The zoomed-in image in (c) reveals that the structure has a hexagonal symmetry with a unit cell of 28.5 Å, corresponding to a (10×10) superstructure. Due to its characteristic appearance the structure is coined "flower" structure. The highly ordered nature of this structure is further highlighted in (d) by the 2D Fourier Transform (FT) of the zoomed image. Finally, (e) presents the LEED image at 57 eV, where the Au(111) reconstruction remains visible alongside the superstructure.

Given the lack of comparable structures in the literature, we propose a possible model to understand the formation of this unique structure. In Figure 6.2, (a) overlays the (111) cut of Cs_2SnBr_6 [27] on the flower structure, where red Sn atoms correspond to the bright atoms observed in the STM image, and dark blue represents Sn atoms that are not visible in the

STM image. Figure 6.2(b) shows a ball-and-stick model of the Cs_2SnBr_6 structure, which we consider a reasonable candidate for the flower structure. Panel (c) displays the (111) plane of Cs_2SnBr_6, highlighting the slab thickness, and (d) provides a perspective view of the slab, emphasizing the distance between four Sn atoms on the top layer, which is 30.5 Å. The slight discrepancy in length can be attributed to the reconstruction of the (111) plane of Cs_2SnBr_6. This structure aligns with the observed flower pattern, likely due to its higher Cs content per unit cell compared to perovskite.

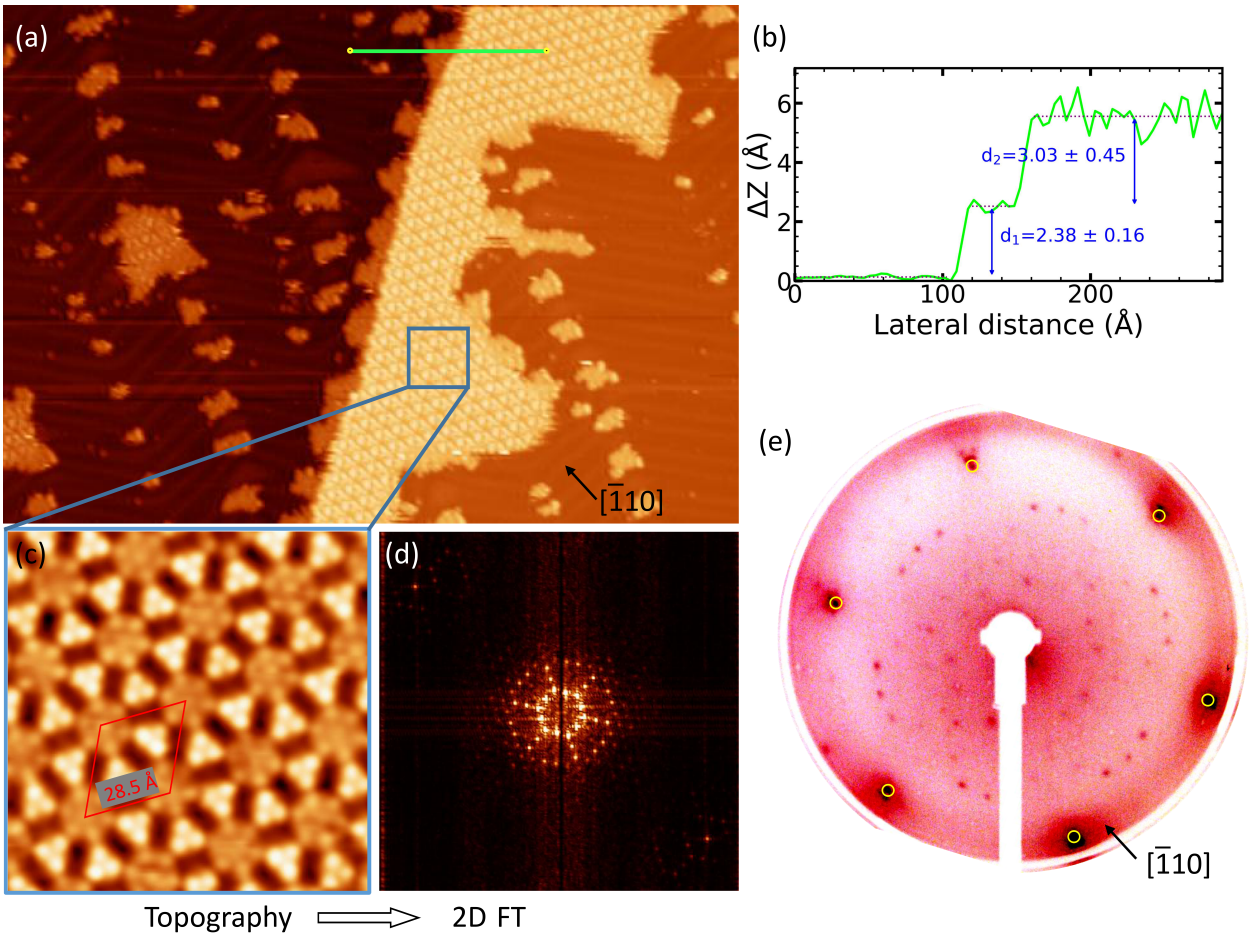


Figure 6.1: (a) STM image of the "flower" structure on Au(111), $U_{\text{bias}} = 2$ V and $I = 0.02$ nA. (b) Line profile corresponding to (a). (c) Zoomed-in view of the selected square region in (a). (d) 2D Fourier Transform (FT) of the zoomed image in (c). (e) LEED image at 57 eV.

The next sample was prepared by co-depositing CsBr and $SnBr_2$ onto an Au(111) substrate with slightly more $SnBr_2$. CsBr was deposited at 422°C with a rate of 0.06 Å/min, while $SnBr_2$ was deposited at 175°C with a rate of 0.11 Å/min. The deposition was carried out for 2 minutes at room temperature. Figure 6.3 (a) shows the STM image of the resulting "stripes" pattern on Au(111) covering nearly a monolayer. The structure grows in three crystallographic directions: $\left[\bar{1}\ 1\ 0\right]$, $\left[0\ \bar{1}\ 1\right]$, and $\left[1\ 0\ \bar{1}\right]$. In (b), the LEED pattern reveals a

5×5 superstructure with respect to gold. In (c), the line profile drawn from the STM image in (a) highlights the height variation of the stripes.

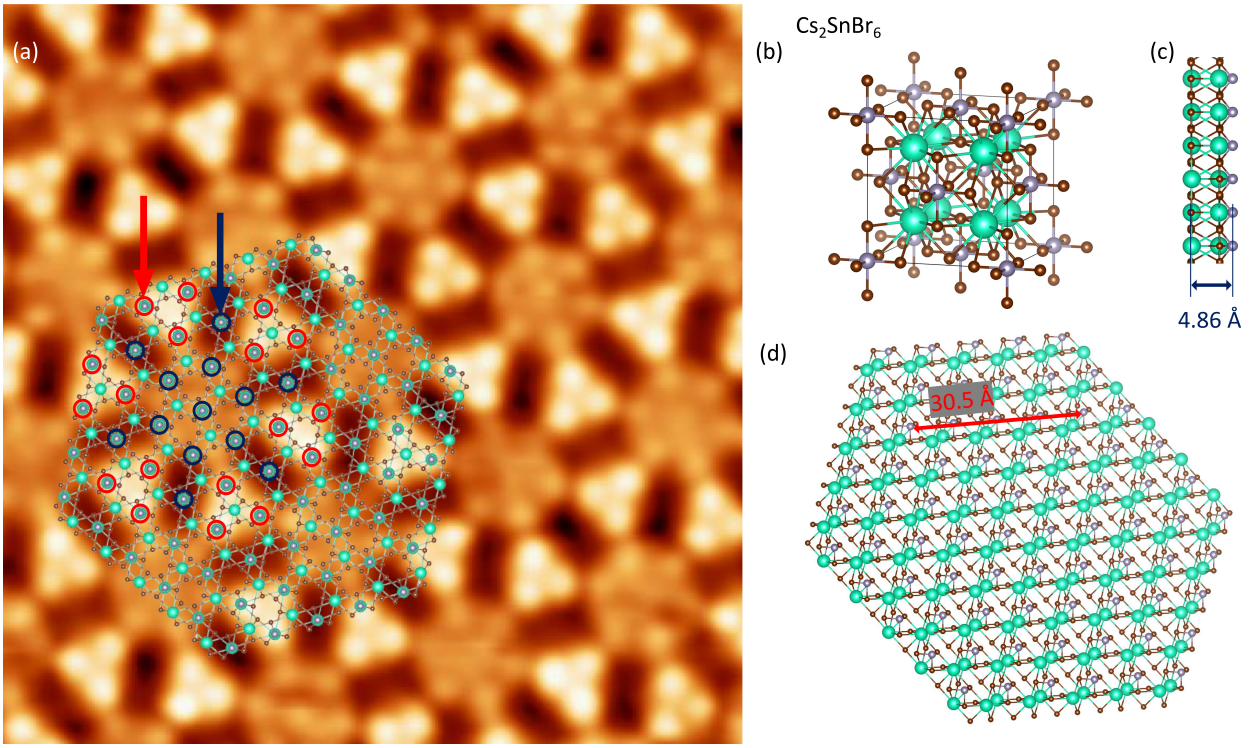


Figure 6.2: (a) Atomically resolved STM image of the "flower" structure on Au(111), $U_{\text{bias}} = 2$ V and $I = 0.05$ nA. (b) Ball-and-stick model of the Cs_2SnBr_6 structure. (c) (111) plane of Cs_2SnBr_6 showing the slab thickness. (d) Perspective view of the slab highlighting the distance between four Sn atoms on the top layer.

Figure 6.4 (a) presents the atomically resolved image of the stripes structure. In (b), the line profile corresponding to the dark blue line in (a) illustrates the smaller periodic structure with square pattern which has lattice constant of 10.66 Å. In (c), the line profile along the green line in (a) reveals a periodicity alternating between 34 and 46 Å, corresponding to two stable arrangements of the square-structured atoms between the stripe tops.

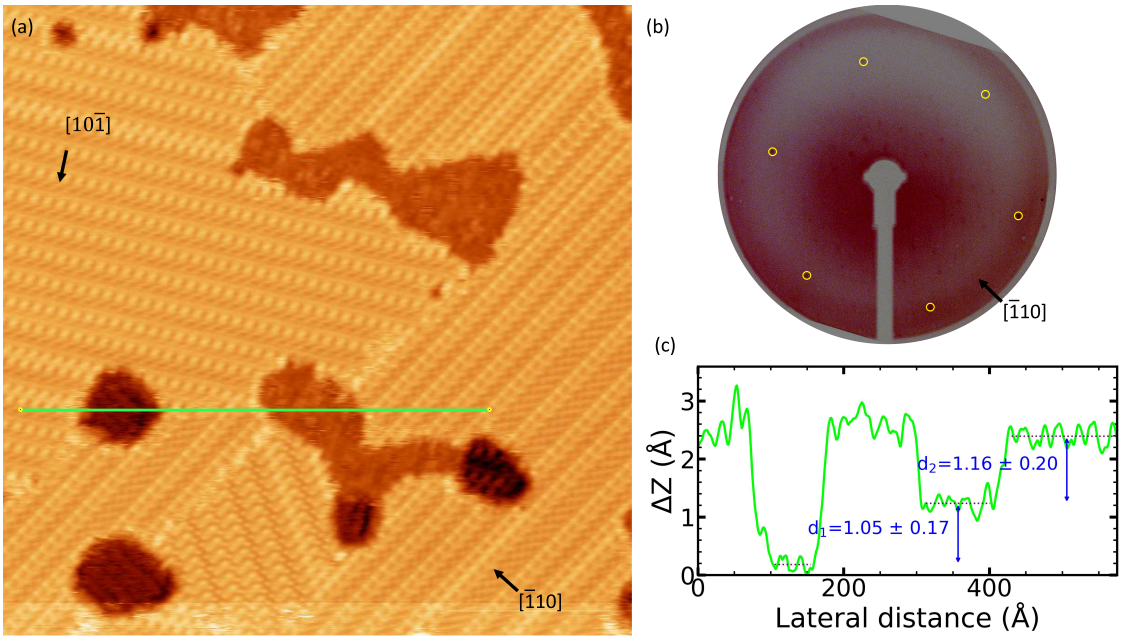


Figure 6.3: (a) STM image of the stripes structure on Au(111), $U_{\text{bias}} = 1.8$ V and $I = 0.04$ nA. (b) LEED image at 57 eV, showing the diffraction pattern of the stripes structure. (c) Line profile drawn in (a).

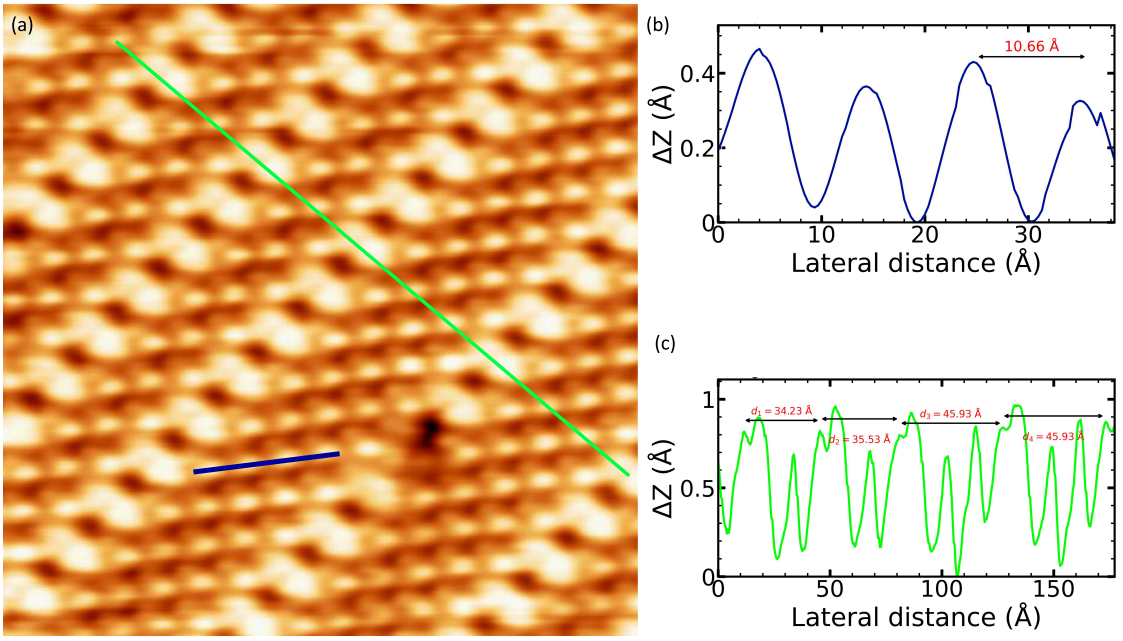


Figure 6.4: (a) Atomically resolved STM image of the stripes structure on Au(111), $U_{\text{bias}} = 1.8$ V and $I = 0.04$ nA. (b) Line profile corresponding to the dark blue line in (a), showing height variations along the stripes. (c) Line profile corresponding to the green line in (a), indicating the periodicity and structural features of the stripes.

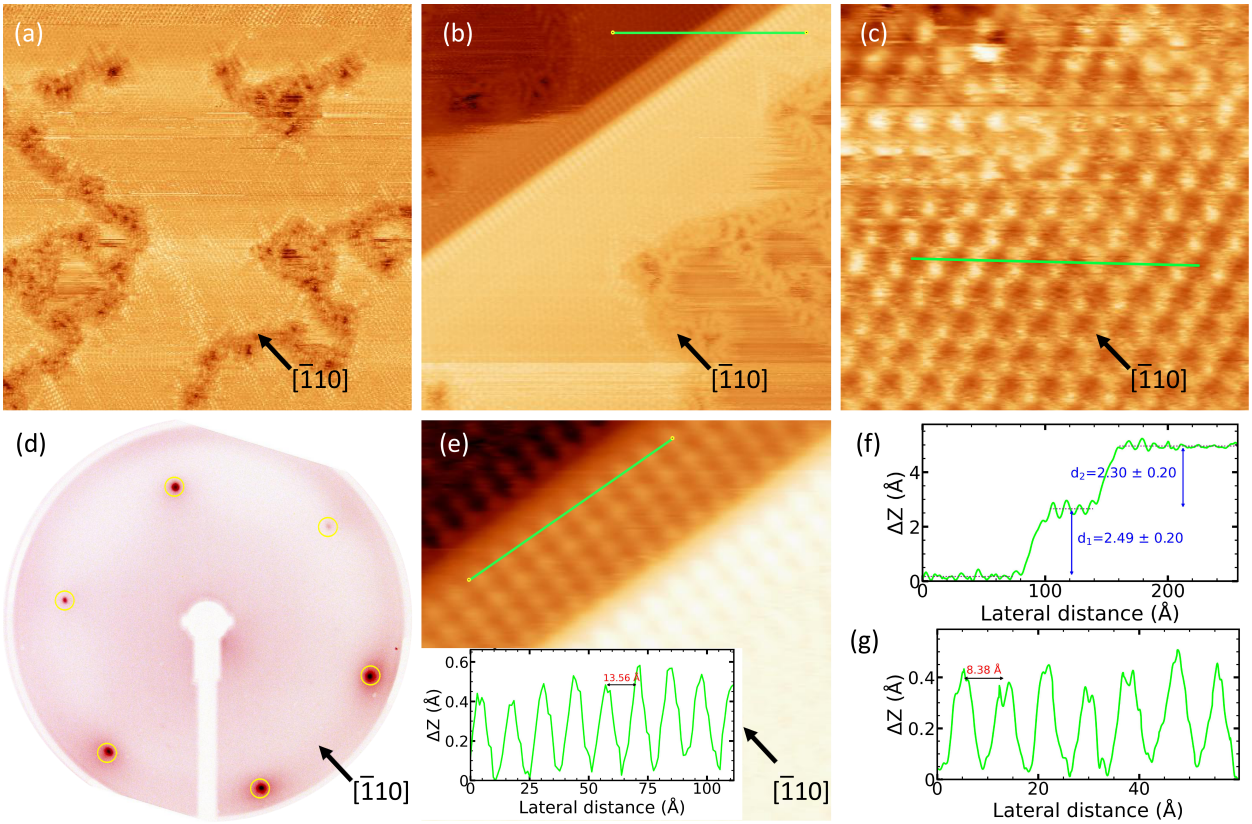


Figure 6.5: (a) 76 nm × 76 nm STM image of CsBr and $SnBr_2$ co-deposited on Au(111) with an excess of $SnBr_2$, $U_{\text{bias}} = 1.6$ V and $I = 0.02$ nA. (b) 48 nm × 48 nm STM image showing the co-deposited surface, $U_{\text{bias}} = 2$ V and $I = 0.02$ nA. (c) 9.5 nm × 9.5 nm close-up view of the honeycomb-like structure appearing in (b), $U_{\text{bias}} = 1.8$ V and $I = 0.02$ nA. (d) LEED image at 57 eV of the same deposition. (e) A close view of the step edges from the region in (b), with the inset showing a structure with square symmetry. (f) and (g) are line profiles corresponding to (b) and (c), respectively.

The next sample was prepared by co-depositing CsBr and $SnBr_2$ onto an Au(111) substrate with less coverage. CsBr was deposited at 422°C with a rate of 0.055 Å/min, while $SnBr_2$ was deposited at 175°C with a rate of 0.11 Å/min. The deposition was carried out for 0.5 minutes at room temperature. The STM image in Figure 6.5(a) shows the resulting honeycomb-like structures on Au(111), formed with an excess of $SnBr_2$. These structures have a lattice constant of 8.2 ± 0.3 Å, comparable to our results for $SnBr_2$ chain structures on Au(111)(Figure 5.4). The honeycomb-like structures are terminated at the edges by square structures, exhibiting a larger lattice constant of approximately 13 Å. In Figure 6.5(b), the step edges clearly show these square structures.

Figure 6.5(c) provides a close-up view of the honeycomb structure, highlighting its detailed arrangement. The LEED image in Figure 6.5(d), taken immediately after deposition, shows the disappearance of the herringbone reconstruction of gold, while the main gold spots

remain visible without any additional spots. Finally, the step height seen in the line profile of Figure 6.5(f) can be attributed to Au(111) step edges.

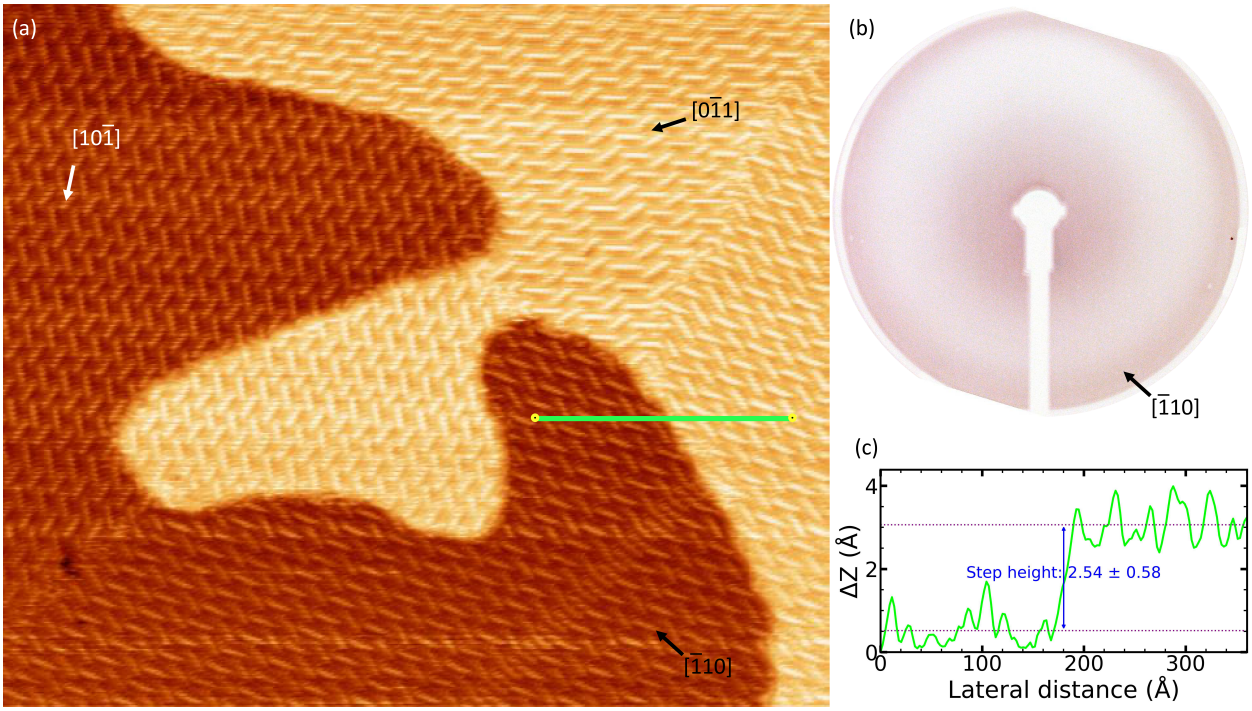


Figure 6.6: (a) STM image of the "ladder" structure on Au(111), $U_{\text{bias}} = 2$ V and $I = 0.03$ nA. (b) LEED image at 57 eV showing no spots. (c) Line profile drawn in (a), highlighting the step height of the gold surface.

The next sample was prepared by co-depositing CsBr and $SnBr_2$ onto an Au(111) substrate with higher coverage. CsBr was deposited at 425°C with a rate of 0.069 Å/min, while $SnBr_2$ was deposited at 168°C with a rate of 0.0644 Å/min. The deposition was performed for 6 minutes at room temperature. In Figure 6.6, (a) shows the STM image of the resulting "ladder" structure on Au(111). The structure grows in three crystallographic directions: $[\bar{1}\ 1\ 0]$, $[0\ \bar{1}\ 1]$, and $[1\ 0\ \bar{1}]$. Domain boundaries are also visible within this image, suggesting a variation in structural alignment across different regions. In (b), the LEED image does not show any visible pattern. In (c), the line profile reveals that the step height is similar to that of Au(111); however, the error bar appears larger due to the higher corrugation of the ladder structure. There seems to be no correlation between the lower and upper terrace, allowing us to exclude carpet layer growth. Instead, the growth appears to happen terrace by terrace.

Figure 6.7 presents the atomically resolved image of the ladder structure. In (a), the image displays chains of atoms spaced approximately 8.59 Å apart, which turn 120 degrees after every four protrusions per line. This turning creates alternating depressions and protrusions along the structure. In (b) and (c), line profiles corresponding to the blue and red lines in (a) illustrate the structural variations along the ladder. Although further experiments and

analysis may yield higher-resolution STM images and provide a deeper understanding of this structure, we are currently unable to assign it to any known structure in the literature.

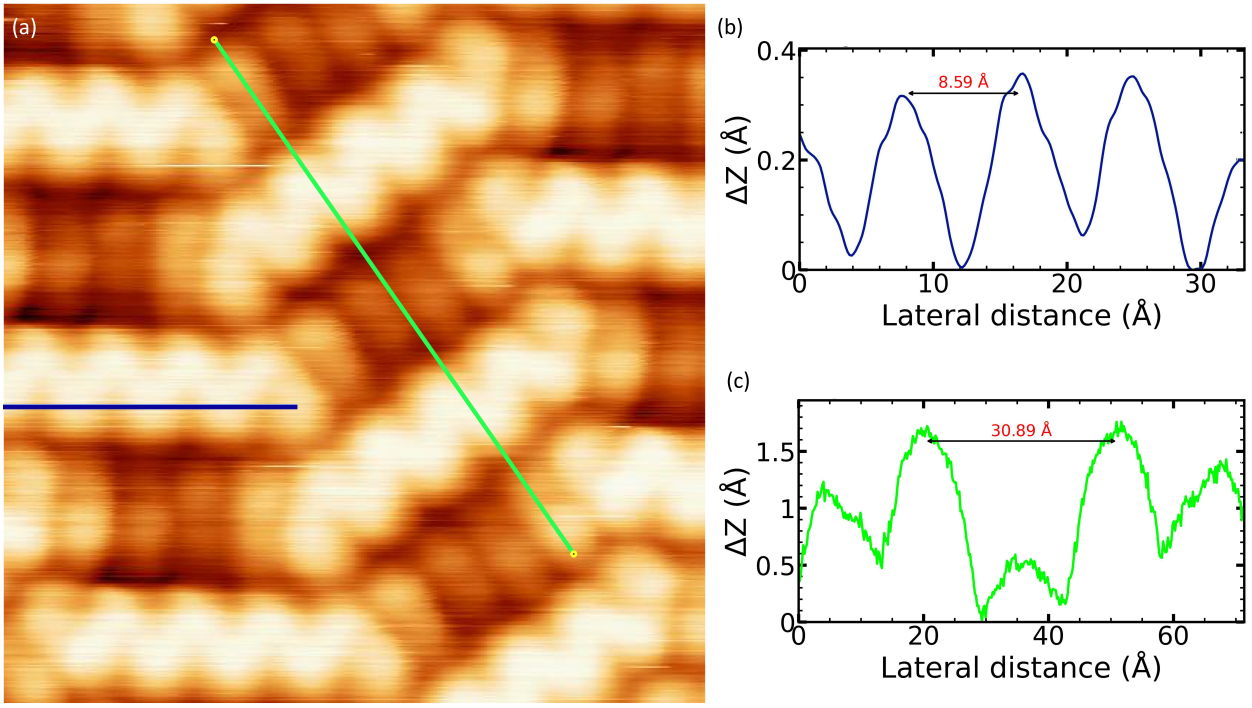


Figure 6.7: (a) Atomically resolved STM image of the "ladder" structure on Au(111), $U_{\text{bias}} = 2$ V and $I = 0.03$ nA. (b) Line profile corresponding to the blue line in (a). (c) Line profile corresponding to the red line in (a), showing the structural variations along the ladder structure.

The STM image in Figure 6.8(a) shows the 6-minute co-deposition of CsBr and $SnBr_2$ on Au(111) with an excess of $SnBr_2$ at higher coverage. Figure 6.8 (b) an atomically resolved image is shown.

In Figure 6.8(c), the filtered STM image of the region from (b) highlights the structural details with improved clarity. The Fourier Transform (FT) of the STM images, before and after filtering, is shown in Figures 6.8(f) and 6.8(g), respectively, to visualize the periodicity and any changes in frequency components due to the filtering process.

The LEED image in Figure 6.8(d), taken at 57 eV, reveals the surface structure after the 6-minute deposition. Additionally, line profiles drawn from the STM images in Figures 6.8(a) and 6.8(c) are shown in Figures 6.8(e) and 6.8(h), respectively, providing insights into the step heights and surface features. The step height is 6.2 ± 0.2 Å, and the lattice constant is measured at 5.84 Å. These values match well with the cubic phase of $CsSnBr_3$.

Our experiments of the codeposition of CsBr and $SnBr_2$ on a Au(111) substrate at room temperature revealed a rich variety of structures, including what we call 'Flower,' 'Honeycomb,' 'Stripes,' 'Ladder,' and 'Square.' These distinct morphologies were observed under varying deposition conditions, characterized by different ratios of CsBr to $SnBr_2$ and varying deposition durations. By systematically exploring these parameters, we gained valuable

insights into the fundamental mechanisms governing the formation of perovskite structures. These findings are instrumental in optimizing growth conditions for high-quality perovskite films.

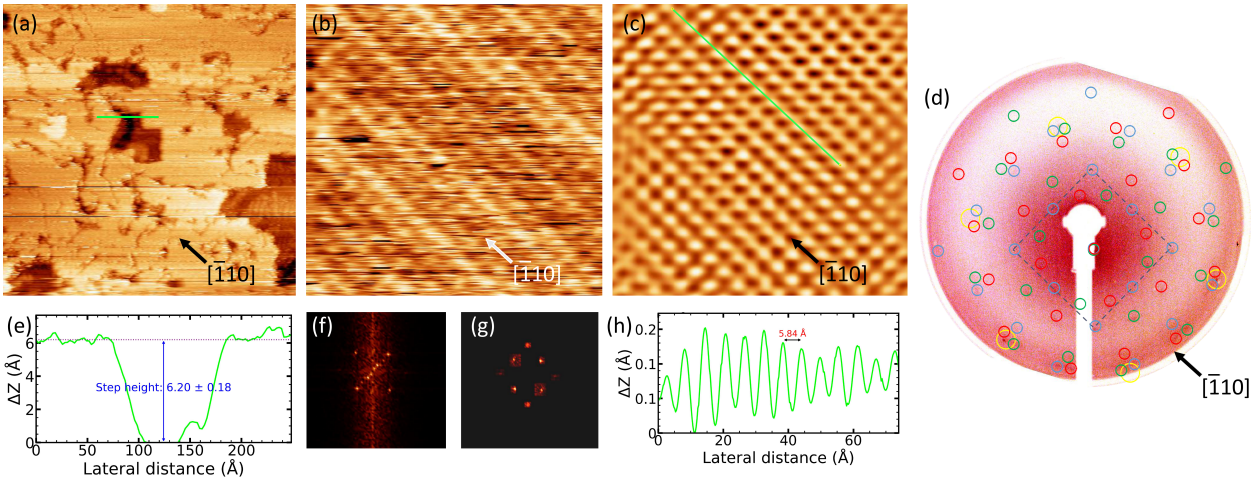


Figure 6.8: (a) STM image of CsBr and $SnBr_2$ co-deposited on Au(111) with an excess of $SnBr_2$ at higher coverage, $U_{bias} = 2$ V and $I = 0.02$ nA. The image size is 120 nm × 120 nm. (b) STM image with a size of 9.5 nm × 9.5 nm, $U_{bias} = 1.8$ V and $I = 0.02$ nA. (c) Filtered STM image of the region in (b), $U_{bias} = 1.6$ V and $I = 0.02$ nA. (d) LEED image taken at 57 eV. (e) and (h) are line profiles drawn from (a) and (c), respectively. (f) and (g) are the 2D Fourier Transforms (FT) of the STM images before and after filtering, corresponding to (b) and (c), respectively.

Deposition duration (minutes)	**Ratio ($CsBr/SnBr_2$)**		
	2/1	**1/1**	**1/2**
0.5 (submonolayer)	/	Flower	Honeycomb
2 (<1ML)	Flower	Flower and square	Stripes
6 (>1ML)	Ladder	Ladder and square	Square

Table 6.1: Codeposition of precursor molecules on Au(111) at different deposition durations and ratios.

Table 6.1 summarizes the deposition conditions and resulting structures for three $CsBr/SnBr_2$ ratios (2/1, 1/1, and 1/2) over different deposition durations. At 0.5 minutes (submonolayer), flower and honeycomb patterns emerge for the 1/1 and 1/2 ratios, respectively. With a 2-minute deposition (less than one monolayer), the 2/1 ratio shows a flower pattern, the 1/1 ratio a mix of flower and square patterns, and the 1/2 ratio stripes. For a 6-minute deposition (more than one monolayer), ladder, ladder-square, and square patterns are observed for the 2/1, 1/1, and 1/2 ratios, respectively.

6.2 Few monolayer coverage

An STM image of a few monolayers (∼6 ML, corresponding to a film thickness of ∼3.5 nm) of $CsSnBr_3$ prepared by co-deposition of CsBr and $SnBr_2$ on Au(111) is shown in Figure 6.9a. The surface is fully covered by perovskite. Steps typically have a height of 2.3±0.2 Å corresponding to the height of one gold atomic layer (see inset right of Figure 6.9 a) revealing the substrate steps underneath the perovskite. Terraces have irregularly terminated edges and sporadically holes, with higher occurrence close to the steps indicating a preference for growth at the terrace. A larger step height is observed, occasionally, on top of the terraces with a height of 5.7±0.3 Å (see inset right of Figure 6.9 a) corresponding to a monolayer island of perovskite. Due to the fully covered surface with several layers of perovskite and the absence of islands larger than 1 ML height, the growth is assigned to the layer-by-layer mode. A LEED image is shown in Figure 6.9 b. Spots marked with yellow circles are assigned to the underlying hexagonal gold surface. Colored spots arranged in a square are assigned to perovskite, which grows along three preferred axes — $[1\bar{1}0]$, $[10\bar{1}]$, and $[01\bar{1}]$ — of the substrate according to its 3-fold symmetry. Using the known lattice constant for gold of 4.070 Å [82], the lattice constant of perovskite is determined from LEED as 5.8±0.1 Å. A model of the epitaxial growth is visualized in Figure 6.9 c. Along the $\langle\bar{1}10\rangle$ directions, the growth is commensurate with one unit cell of perovskite occupying two unit cells of gold. The preference of growth along these directions is in accordance with the small lattice mismatch of gold and perovskite amounting to 1.1%, when considering two unit cells of Au(111) along $\langle\bar{1}10\rangle$ and one unit cell of $CsSnBr_3$ (001).

Figure 6.10 depicts atomically-resolved STM images of the $CsSnBr_3$ perovskite surface at low temperature (T=118 K). Bright protrusions are arranged in a square-like pattern. The distance between the neighboring protrusions is $d_1 = 4.8 \pm 0.2$ Å for the short and $d_2 = 6.8 \pm 0.2$ Å for the long distance. The size of the unit cell depicted in the image is 11.6×11.6 Å^2 (dashed orange square). The apparent height corrugation is approximately 0.3 Å. Occasionally, an armchair-like pattern is observed as highlighted in the image (white lines bottom left). The armchair pattern is found at the transition between domains which are shifted by half a lattice constant (see black lines in Figure 6.10 a), i.e., at an antiphase domain boundary. The edges of the terraces are mostly irregular. However, some edges are preferred following the edges of the unit cell or being aligned at an angle of 45° to it (white lines at middle right). In Figure 6.10 two domains are present following the Au(111) substrate symmetry. In total, three main directions have been observed (third one see Figure 6.12 a), following the same directions as observed in LEED. Due to the differently oriented domains, domain boundaries are observed showing a depression at the intersection (Figure 6.12 b).

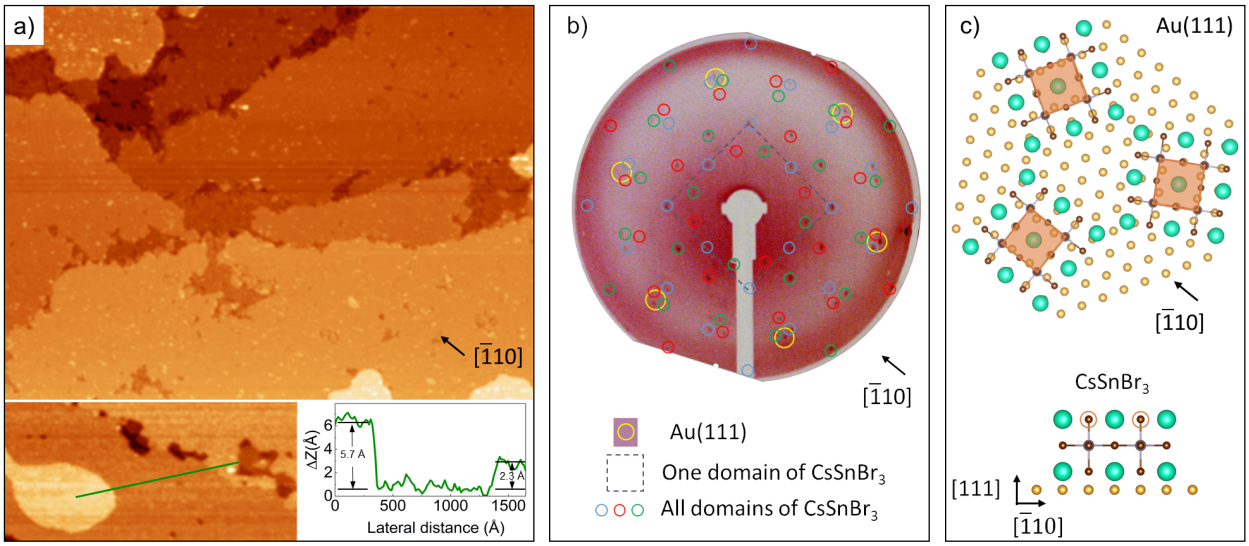


Figure 6.9: $CsSnBr_3$ on Au(111). (a) STM topography image at low temperature (T=118 K) , $U_{\text{Bias}} = 2$ V, $I = 0.02$ nA (Image size: 390×500 nm^2). Inset left: $U_{\text{Bias}} = 2$ V, $I = 0.02$ nA (144×300 nm^2). Inset right: Apparent height profile along the green line. (b) LEED image acquired at 57 eV. Yellow circles mark spots originating from Au. Red, green, and blue circles, respectively, mark one of the three possible orientational domains of the perovskite. The dashed blue square highlights the first order spots of one orientation. (c) Model of the top view (top) and side view (bottom) of the alignment of perovskite with respect to Au(111). Crystallographic directions refer to gold. Color legend of spheres: Cs (green), Sn (grey), Br (brown), and Au (yellow).

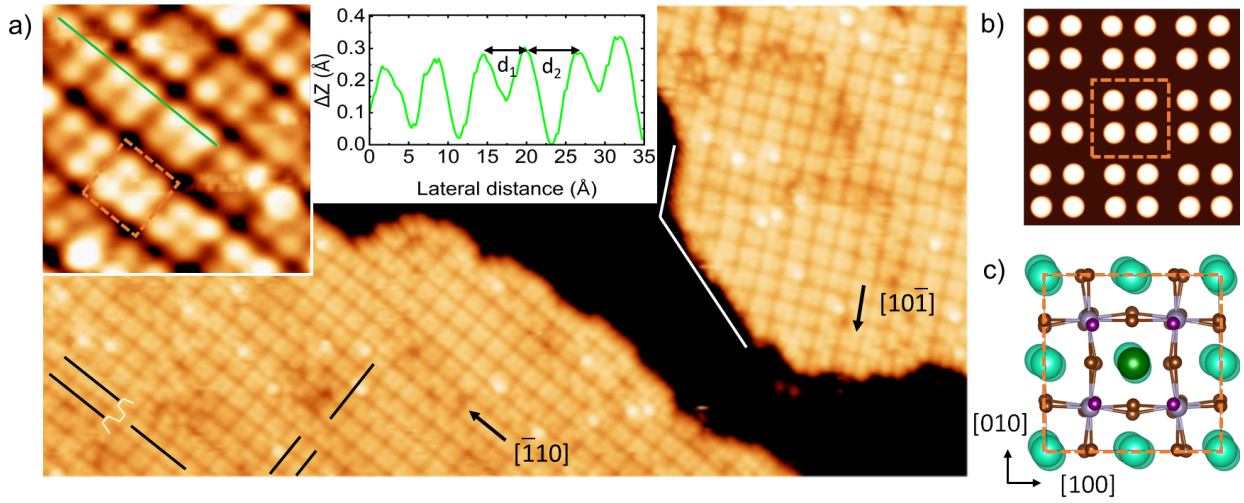


Figure 6.10: Atomically resolved STM image of $CsSnBr_3$ on Au(111). (a) STM image showing different orientational domains. White lines (left bottom) mark the armchair pattern. Black lines are guides to the eye indicating the shift of half a lattice constant. White lines (middle right) mark the perovskite edges. Inset left: High-resolution STM image. The dashed square marks the unit cell. Inset middle: Height profile along the green line in the inset on the left. Crystallographic directions refer to the metal substrate. (b) Simulated STM image of the tetramer phase. (c) Atomic structure of the (001) surface of $CsSnBr_3$ (tetramer phase) (top view). Dark green and violet: Cs and Br (only top layer). Light green, brown, and grey: Cs, Br, and Sn. Dashed lines in (b) and (c) mark the computational cell of size 11.7×11.7 Å^2. Parameters: (a) $U_{\mathrm{Bias}} = 2$ V, $I = 0.02$ nA. Size: 50×21.3 nm^2 and inset 4.5×4.5 nm^2. (b) Integration of the density of states from 0 to 2 eV. Crystallographic directions in (c) refer to the perovskite.

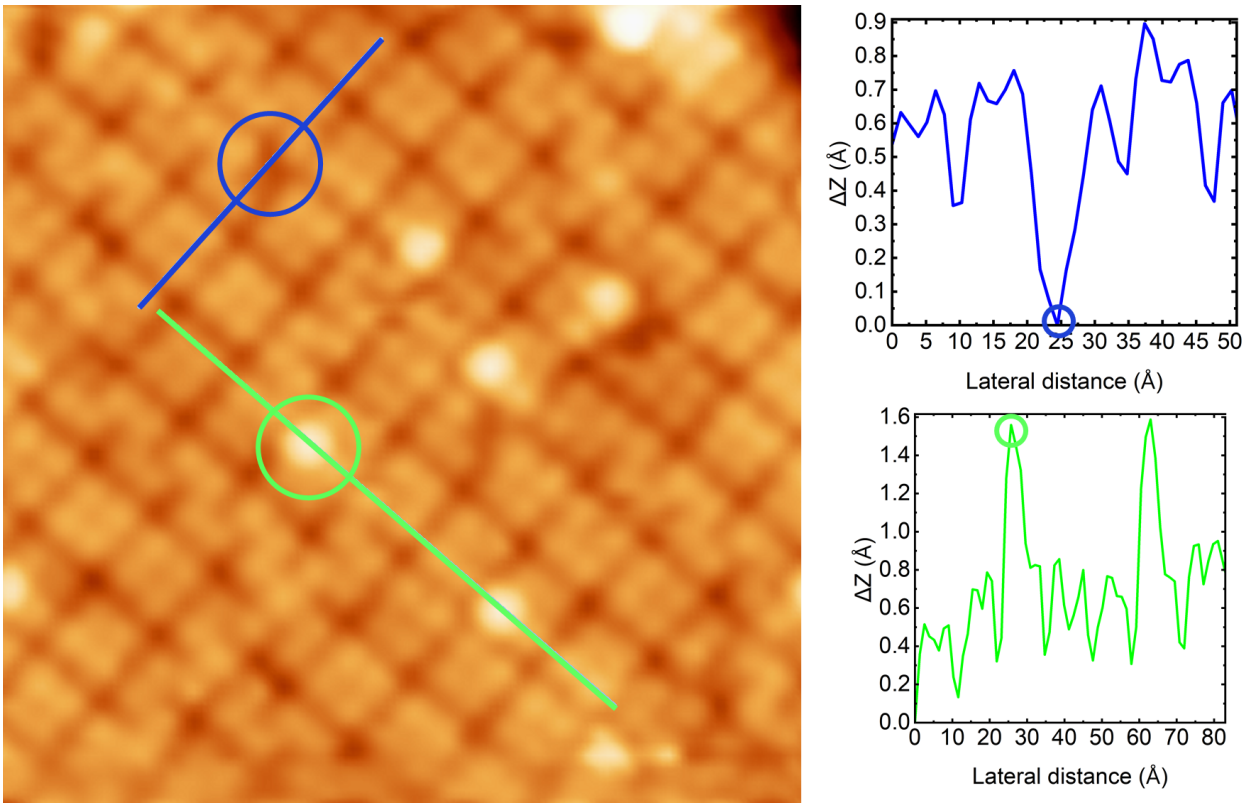


Figure 6.11: High-resolution STM image of $CsSnBr_3$ on Au(111) showing surface defects. $U_{\text{Bias}} = 2$ V, $I = 0.02$ nA (Image size: 11.4×11.4 nm^2). A large protrusion marked by a green circle and a depression marked by a blue circle.

Defects in halide perovskites can play an important role in solar cell performance [87, 88]. In Figure 6.11, a high-resolution STM image showing several defects is shown. Large protrusions with an additional height of 0.7 ± 0.1 Å above the regular protrusions and depressions with a reduced height of 0.7 ± 0.1 Å with respect to the regular protrusions are observed. A characteristic shared by all these protrusions is their presence at the position of one of the corners of the small square pattern. Depressions are assigned to Br vacancies [89, 90] and larger protrusions are assigned to adatoms [90, 91].

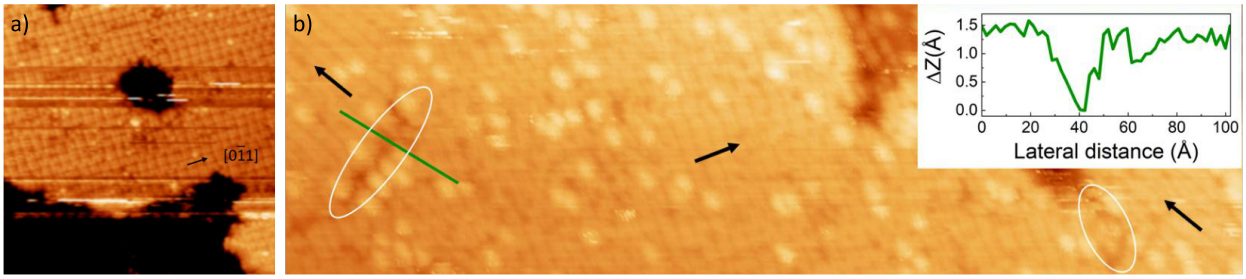


Figure 6.12: (a) Co-deposition of CsBr and $SnBr_2$ on Au(111). $U_{\text{bias}} = 2$ V, $I = 0.05$ nA. Image size: 34.4×34.4 nm^2. (b) White ellipses mark regions of domain boundaries. Black arrows indicate the orientation of respective domains. Inset shows apparent height profile across the domain boundary. Scanning parameters: $U_{\text{bias}} = 2$ V, $I = 0.05$ nA. Image size: 20.6×72.4 nm^2.

To get a more detailed understanding of the experimental results of the surface DFT calculations were performed. Based on the symmetry of the STM and LEED, the (001) surface is to be expected, which we used as a starting configuration for the computations. In this configuration, the perovskite is composed of atomic planes which alternate between CsBr and $SnBr_2$. Therefore, the surface can be either terminated with a CsBr or $SnBr_2$ plane.

Based on our calculations, we can rule out the $SnBr_2$ termination as it does not reproduce the observed pattern in the STM images. We note, while a similar pattern on a lead perovskite may be caused by such termination [82], also our observed shift of the lattice showing an armchair arrangement would not be compatible with this surface termination. For the CsBr termination we considered three cases with varying numbers of Cs atoms in the surface unit cell (see Figure 6.13). The best match was found for one Cs atom per supercell. The simulated STM image in Figure 6.10b agrees well with the experimental observations. The simulated atomic structure of the surface is shown in Figure 6.10 c. One Cs cation is surrounded by four Br anions in the top layer held together by attractive electrostatic interaction. A similar pattern has been found for a different perovskite, namely $CsSnI_3$, termed tetramer phase, due to the four Br atoms surrounding the Cs in the surface [91]. Our DFT simulations enable us to associate the protrusions seen in the STM image with Br anions. In particular, we can correlate the measured distances d_1 and d_2 to the Br-Br distances of the simulation (see Figure 6.14), which are matching well. Cs cations are not visible in the image, in accordance with previous reports in the literature [92]. The crystallographic structure of the perovskite is thus assigned to the orthorhombic crystal system with the Pnma space group as used in the DFT simulations.

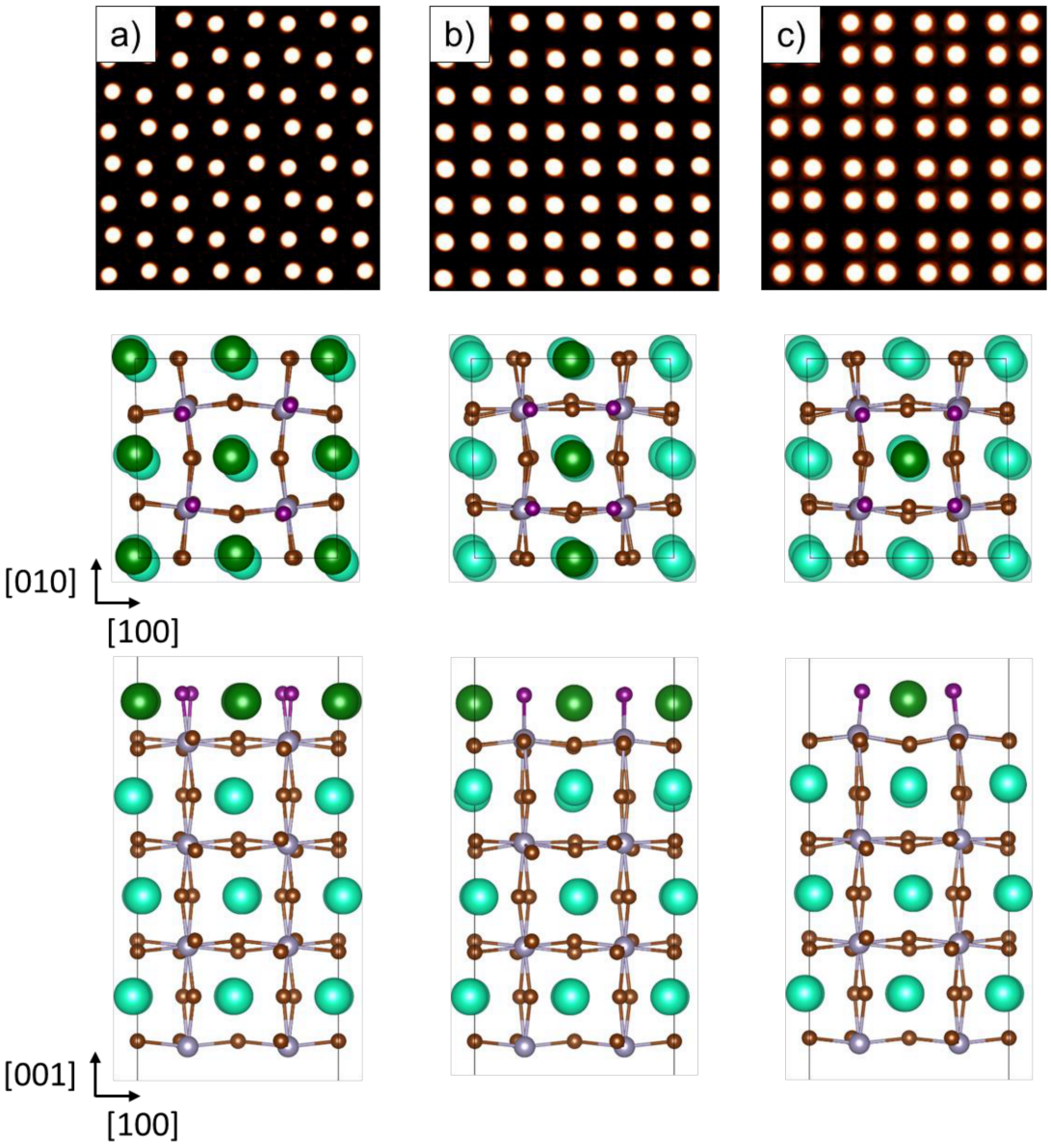


Figure 6.13: DFT calculations of $CsSnBr_3$. (top row) Simulated STM image, (middle row) top view of the atomic structure of the (001) perovskite plane, and (bottom row) side view of the atomic structure. Black lines mark the boundaries of the supercell. Cs (light green and for the surface atoms dark green), Sn (grey), and Br (brown and for the surface atoms violet). (a) 4 Cs atoms per supercell, (b) 2 Cs atoms per supercell, (c) 1 Cs atom per supercell.

The detailed parameters used for the DFT calculations are outlined in the following. The energy cutoff of the plane-wave expansion is set to 450 eV and all atomic positions of the bottom four layers in the slab models are fixed whereas the other are relaxed until a force criterion of 0.005 eV/Å is reached. All the slab models are extracted from the relaxed

orthorhombic bulk structure of $CsSnBr_3$ by adding a 15 Å thick vacuum layer in the [001] direction. In all cases the surfaces are terminated with Cs and Br atoms. A $2\times2\times1$ supercell (a = 11.72 Å, b = 11.72 Å, $\alpha = \beta = \gamma = 90°$) is constructed for the surface reconstruction. Three models are studied: pristine, two Cs vacancies in the surface, and three Cs vacancies in the surface. Γ-centered $5 \times 5 \times 1$ k-meshes are used for all the slab models.

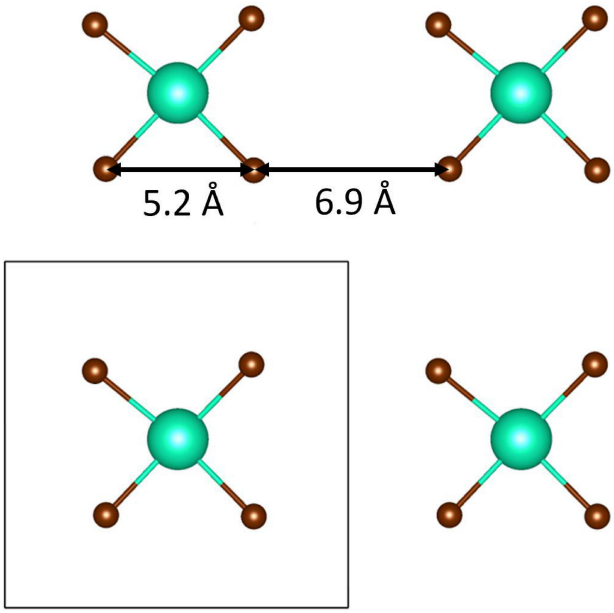


Figure 6.14: DFT calculation of $CsSnBr_3$. Additional representation of the geometry of the surface of the tetramer configuration, i.e., one Cs atom per unit cell (see Figure 6.13 c), with explicitly marked Br–Br distances. Cs (light green) and Br (brown). Black line marks the boundary of the supercell.

Pristine: The supercell contains 16 Cs (4 in the surface), 16 Sn, and 44 Br atoms. The Sn-Br (Sn in the subsurface and Br in the surface) average bond length is 2.97 Å. The Cs-Br (Cs in the surface and Br in the subsurface) bond lengths are Cs-Br1 = 4.02 Å, Cs-Br2 = 4.01 Å, Cs-Br3 = 3.77 Å, and Cs-Br4 = 4.91 Å. The Cs-Br (both Cs and Br in the surface) bond lengths are Cs1-Br = 3.80 Å, Cs2-Br = 3.79 Å, Cs3-Br = 4.62 Å, and Cs4-Br = 4.47 Å.

Two Cs vacancies in the surface: The supercell contains 14 Cs, 16 Sn, and 44 Br atoms. The Sn-Br (Sn in the subsurface and Br in the surface) average bond length is 2.69 Å. The Cs-Br (Cs in the surface and Br in the subsurface) bond lengths are Cs-Br1 = 3.95 Å, Cs-Br2 = 3.78 Å, Cs-Br3 = 3.74 Å, and Cs-Br4 = 4.09 Å. The average Cs-Br (both Cs and Br in the surface) bond length is 3.83 Å.

Three Cs vacancies in the surface: The supercell contains 13 Cs, 16 Sn, and 44 Br atoms. The Sn-Br (Sn in the subsurface and Br in the surface) average bond length is 2.60 Å. The Cs-Br (Cs in the surface and Br in the subsurface) bond lengths are Cs-Br1 = 3.89 Å, Cs-Br2 = 3.96 Å, Cs-Br3 = 3.85 Å, and Cs-Br4 = 3.90 Å. The Cs-Br (both Cs and Br

in the surface) bond lengths are Cs-Br1 = 3.83 Å, Cs-Br2 = 3.81 Å, Cs-Br3 = 3.78 Å, and Cs-Br4 = 3.86 Å.

The STM images are calculated by integrating the density of states from 0 to 2 eV.

Chapter 7

$CsSnBr_3$ on Au(100)

7.1 Submonolayer coverage

To determine the impact of the substrate symmetry on the growth of the $CsSnBr_3$ perovskite, we investigate the growth of $CsSnBr_3$ on a Au(100) substrate that possesses a square lattice. The initial stages of $CsSnBr_3$ perovskite growth on Au(100) are essential for understanding the formation of high-quality thin films. In the submonolayer regime, co-deposition of CsBr and $SnBr_2$ precursors allows the investigation of nucleation and initial growth behavior. This regime also highlights the influence of the Au(100) surface reconstruction on the deposited species. STM and LEED were used to study the surface morphology and structure during this stage.

The submonolayer regime provides valuable insights into the interplay between the CsBr and $SnBr_2$ precursors and the role of substrate-induced effects in the growth process. These findings establish a foundation for understanding subsequent growth stages and the formation of continuous $CsSnBr_3$ films.

Figure 7.1 presents STM and LEED images capturing the morphology of CsBr and $SnBr_2$ co-deposition on Au(100) under the conditions: CsBr at 425°C with a deposition rate of 0.07 Å/min and $SnBr_2$ at 172°C with a rate of 0.09 Å/min, with deposition time of 1 min. on the substrate held at room temperature and subsequent cooling for STM analysis. After deposition, the LEED image (panel e) shows the absence of the typical Au(100) reconstruction, suggesting that the co-deposited layers alter the original surface structure. In STM panel (a), the lowest surface visible corresponds to the Au(100) terraces, with line profiles in panels (a) and (b) illustrating the step edges of the Au(100) substrate.

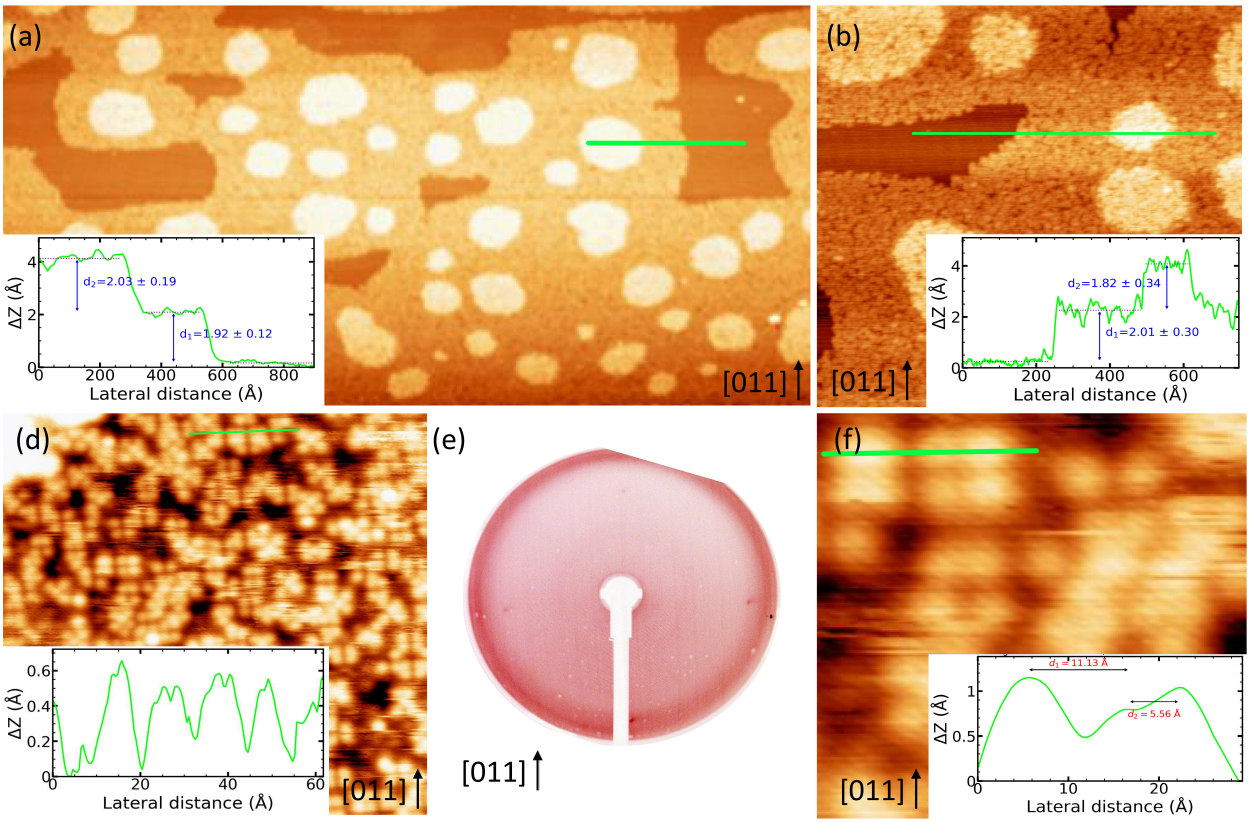


Figure 7.1: STM images of CsBr and $SnBr_2$ co-deposition on Au(100) are shown in (a), (b), (d), and (f), recorded under measurement conditions of $U_{\text{Bias}} = 2.3\,\text{V}$ and $I = 0.02\,\text{nA}$. The image dimensions are: (a) $468 \times 246\,\text{nm}^2$, (b) $106 \times 106\,\text{nm}^2$, (d) $24 \times 24\,\text{nm}^2$, and (f) $6 \times 6\,\text{nm}^2$. The LEED pattern in (e) was captured at 59 eV, with the crystallographic direction [011] aligned to the Au(100) substrate. Insets within the STM images display line profiles, illustrating the height variations across terraces and islands.

The STM images further reveal that the resulting surface is rough and incomplete, reflecting a partially formed perovskite layer. Panel (d) displays the disordered surface structure with short-range order, showing a disrupted, non-uniform layer across the substrate. Panel (f) includes measurements highlighting the irregular spacing between atomic structures, indicating a lack of continuity in the perovskite coverage, as reflected in the bright protrusions and roughness evident across the STM images.

The co-deposition of CsBr, at 425°C with a rate of 0.07 Å/min, and $SnBr_2$, at 174°C with a rate of 0.11 Å/min, was performed on Au(100) for 2.5 minutes at room temperature, which is longer than the previous time. Figure 7.2 a shows the corresponding STM image resulting in a coverage of approximately 1 ML and the appearance of islands. In Figure 7.2 a, the absence of the Au(100) reconstruction suggests that excess gold atoms have formed isolated gold islands, which are visible in the STM image. The line profile drawn in Figure 7.2 a confirms that the step heights of these islands are comparable to the Au(100) terrace steps. Figure 7.2 c presents the area ratio of gold islands to the entire surface, calculated

using a Python code to evaluate the distribution of island coverage amounting to 0.26 with respect to the total area. In Figure 7.2 d, atomic displacements appear comparable to the lattice constant of $CsSnBr_3$.

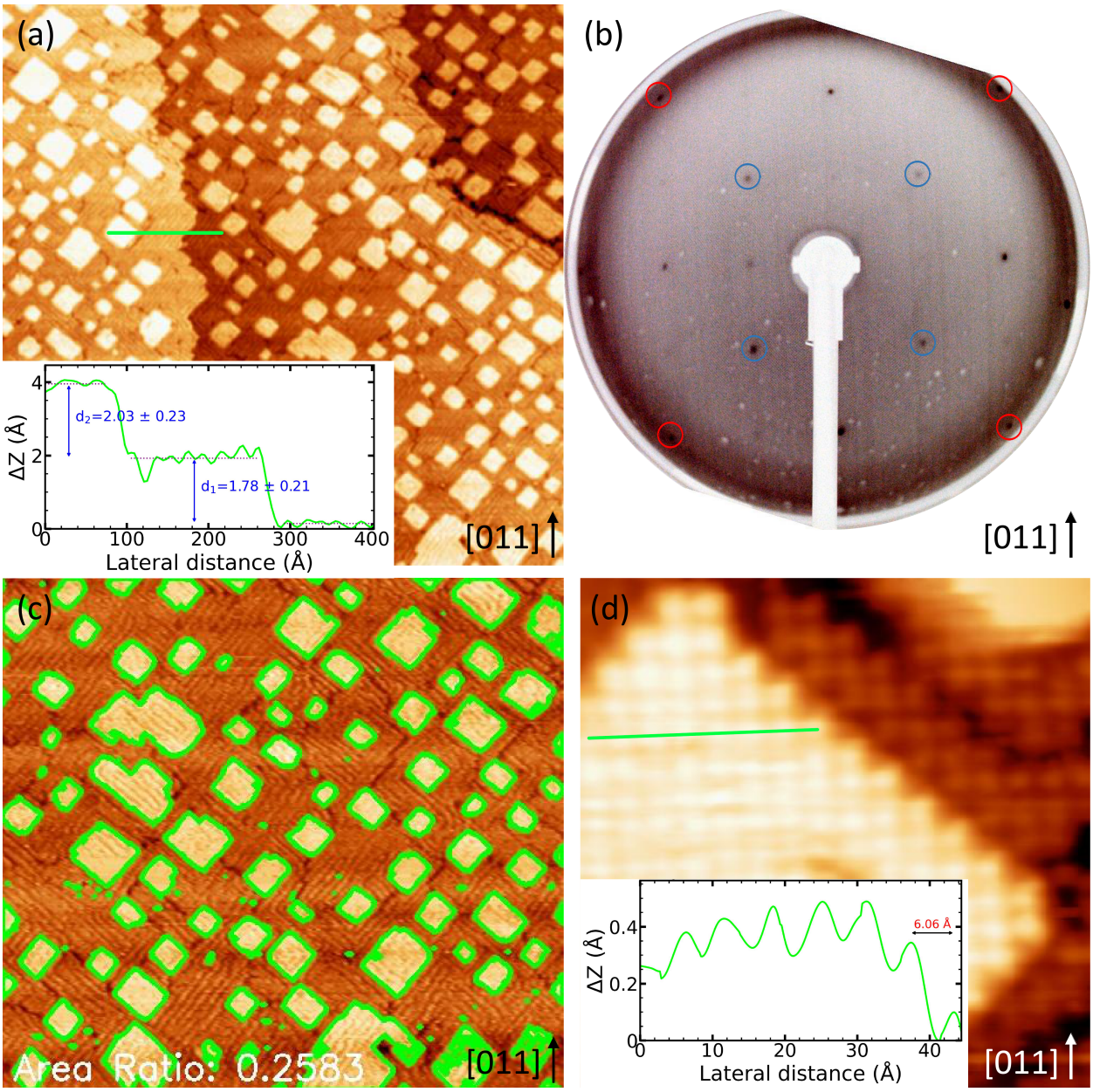


Figure 7.2: STM images of CsBr and $SnBr_2$ co-deposition on Au(100) are shown in (a), (c), and (d), recorded under measurement conditions of $U_{\text{Bias}} = 2.3\,\text{V}$ and $I = 0.01\,\text{nA}$. The image dimensions are: (a) $200 \times 200\,\text{nm}^2$ and (d) $10 \times 10\,\text{nm}^2$. The LEED pattern in (b) was captured at 59 eV. Image (c) illustrates the area ratio of gold islands trapped beneath the deposited layer. Insets in (a) and (d) include line profiles, highlighting height variations.

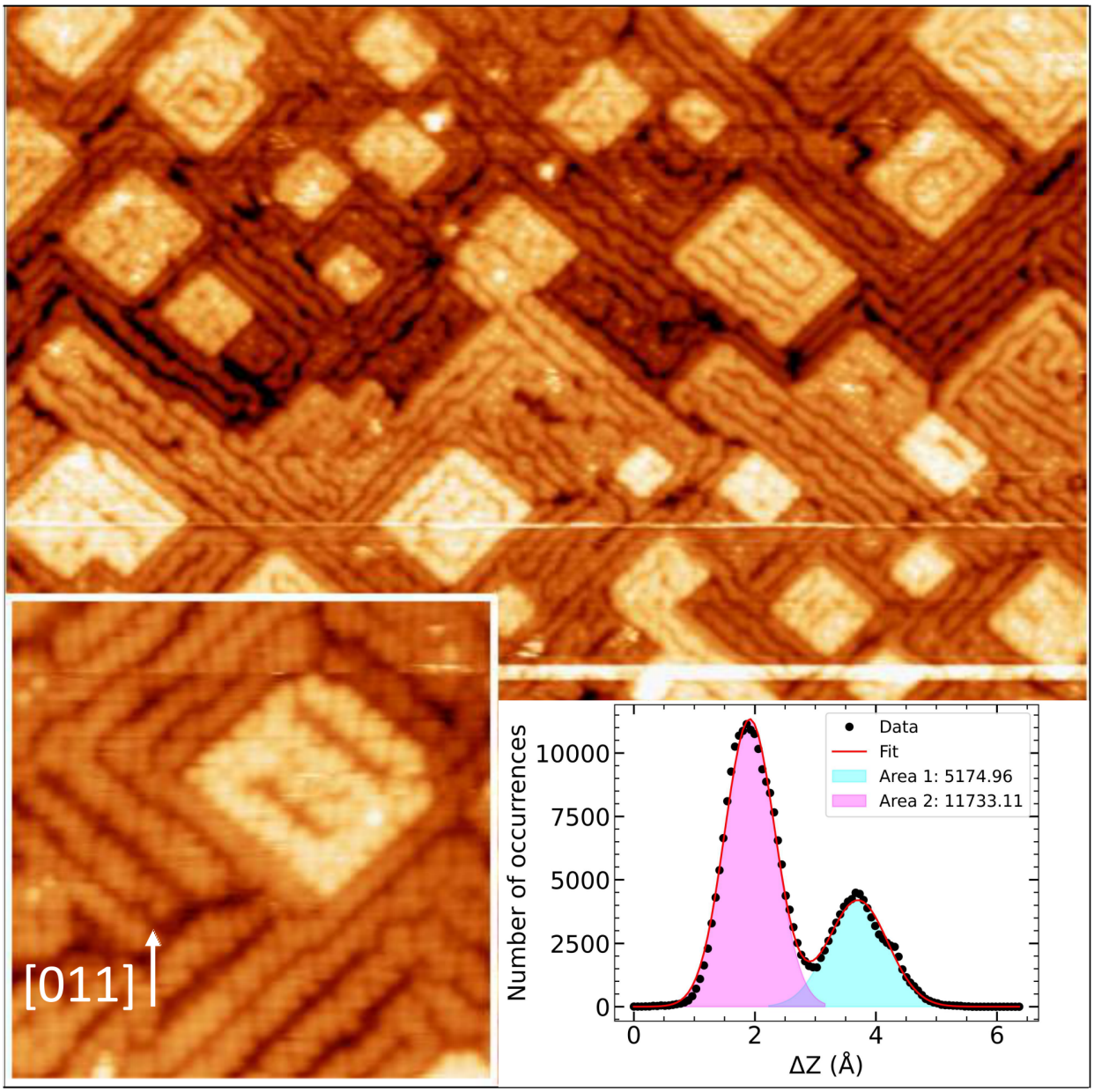


Figure 7.3: Co-deposition of CsBr and $SnBr_2$ on Au(100) with an approximate coverage of 1 ML. Measurement conditions: $U_{\text{Bias}} = 2\,\text{V}$, $I = 0.1\,\text{nA}$ with image size of $100 \times 100\,\text{nm}^2$. Insets: Left inset with $U_{\text{Bias}} = 2\,\text{V}$, $I = 0.1\,\text{nA}$ over $12 \times 12\,\text{nm}^2$. Right inset shows a histogram of the apparent height taken on one terrace, with the peak at smaller height assigned to the terrace itself and the one at larger height to the islands. The distance between the peaks is 2.0 ± 0.1 Å, corresponding to the height of one atomic layer of Au. The ratio of the area of all islands to the total area is 0.3 ± 0.1.

Figure 7.3 shows that locally a square structure is present with a lattice constant of approximately 6 Å, indicating the formation of $CsSnBr_3$. These findings are further confirmed by the LEED image shown in Figure 7.3 b, where the reconstruction is lifted and a (2×2)

superstructure appears in agreement with the lattice of $CsSnBr_3$. The histogram in the right inset reveals a peak separation of 2.0 ± 0.1 Å, corresponding to the height of one atomic layer of Au, with the ratio of the island area to the total surface area determined to be 0.3 ± 0.1, in agreement with the analysis of Figure 7.3 c. Islands of the same height and coverage are observed as for the several monolayers case. The surface structure of the islands is identical to the one on the terrace, showing lines of perovskite-like structures. For the Au reconstruction, there are 6 atoms within a (5×1) unit cell, whereas without reconstruction there are only 5 atoms [62]. Thus, there are 20% more atoms in the unit cell of the reconstruction compared to the bulk value. These additional atoms form the gold islands. The adsorption of the perovskite lifts the reconstruction lowering the needed number of atoms per unit cell, which then form gold islands. The islands are still present after a coverage of several monolayers. We cannot find overgrowth on the step edges which further proves the islands are from the trapped gold atoms underneath.

In the submonolayer regime, STM images reveal a rough and incomplete perovskite layer with short-range order and irregular atomic spacing accompanied by the formation of gold islands. LEED patterns indicate alterations to the Au(100) surface structure.

7.2 Few monolayer coverage

7.2.1 Sequential deposition

Alternatively to the co-deposition the sequential deposition of CsBr and SnBr was investigated. The sample was prepared by sequential deposition of CsBr at 425°C with a rate of 0.05 Å/min and $SnBr_2$ at 172°C with a rate of 0.07 Å/min on Au(100), targeting a ($SnBr_2$/CsBr) ratio of 1.4 with a coverage above one monolayer. Figure 7.4 shows an STM image from this deposition sequence. The LEED image in Figure 7.4 b reveals a 2×2 structure, suggesting the $CsSnBr_3$ structure. In Figure 7.4 a, the measured steps are comparable with those of the Au(100) substrate (see panel (d)). Figure 7.4 c highlights surface protrusions and depressions, with line profile (e) providing measurements of both the height of the protrusions and the depth of the depressions. The STM images and line profiles highlight the effects of sequential deposition on the formation of strcutures on the surface. The protrusions are assigned to adatoms and the depressions are assigned to Br-vacancies.

Figure 7.5 demonstrates the mobility of atoms on the surface, captured through sequential STM images taken at 5-minute intervals. Panels (a), (b), (d), (e), (g), and (h) display STM images showing atomic positions over time, with visible shifts in atom positions indicating surface mobility at room temperature. Panels (c), (f), and (i) present subtracted images, where (c) is the difference between (a) and (b), (f) is the difference between (d) and (e), and (i) is the difference between (h) and (g). These subtracted images emphasize areas of atomic movement, with bright yellow spots representing the appearance of atoms at specific positions. This sequential analysis reveals the dynamic behavior of atoms on the surface, highlighting the extent of atomic mobility under the given conditions.

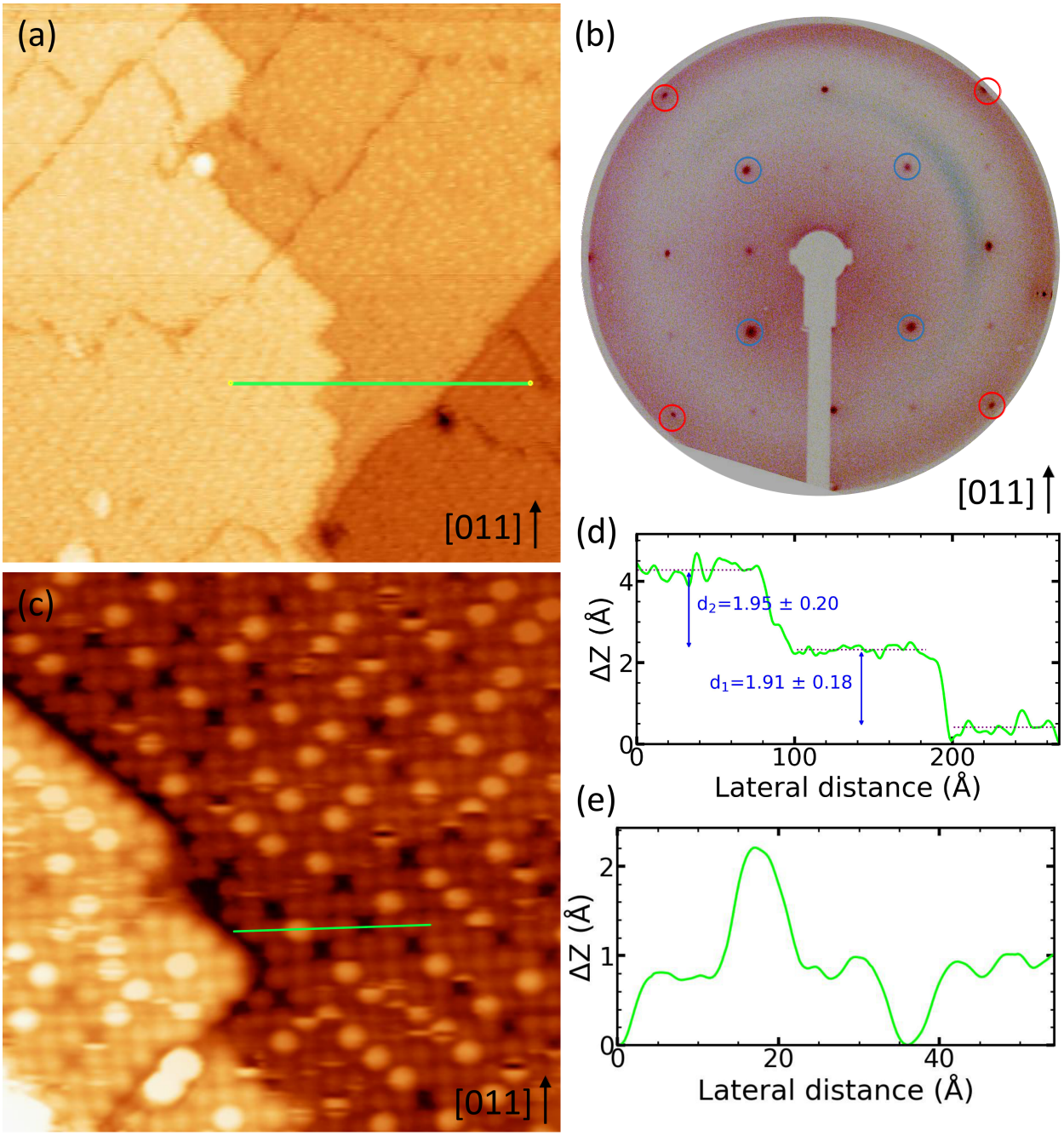


Figure 7.4: STM images of sequential deposition of CsBr and $SnBr_2$ on Au(100) are shown in (a) and (c), recorded under measurement conditions of $U_{\mathrm{Bias}} = 2\,\mathrm{V}$ and $I = 0.02\,\mathrm{nA}$. The image dimensions are: (a) $50 \times 50\,\mathrm{nm}^2$ and (c) $10 \times 10\,\mathrm{nm}^2$. The LEED pattern in (b) was captured at 58 eV. Line profiles drawn in (a) and (c) are presented in (d) and (e), respectively.

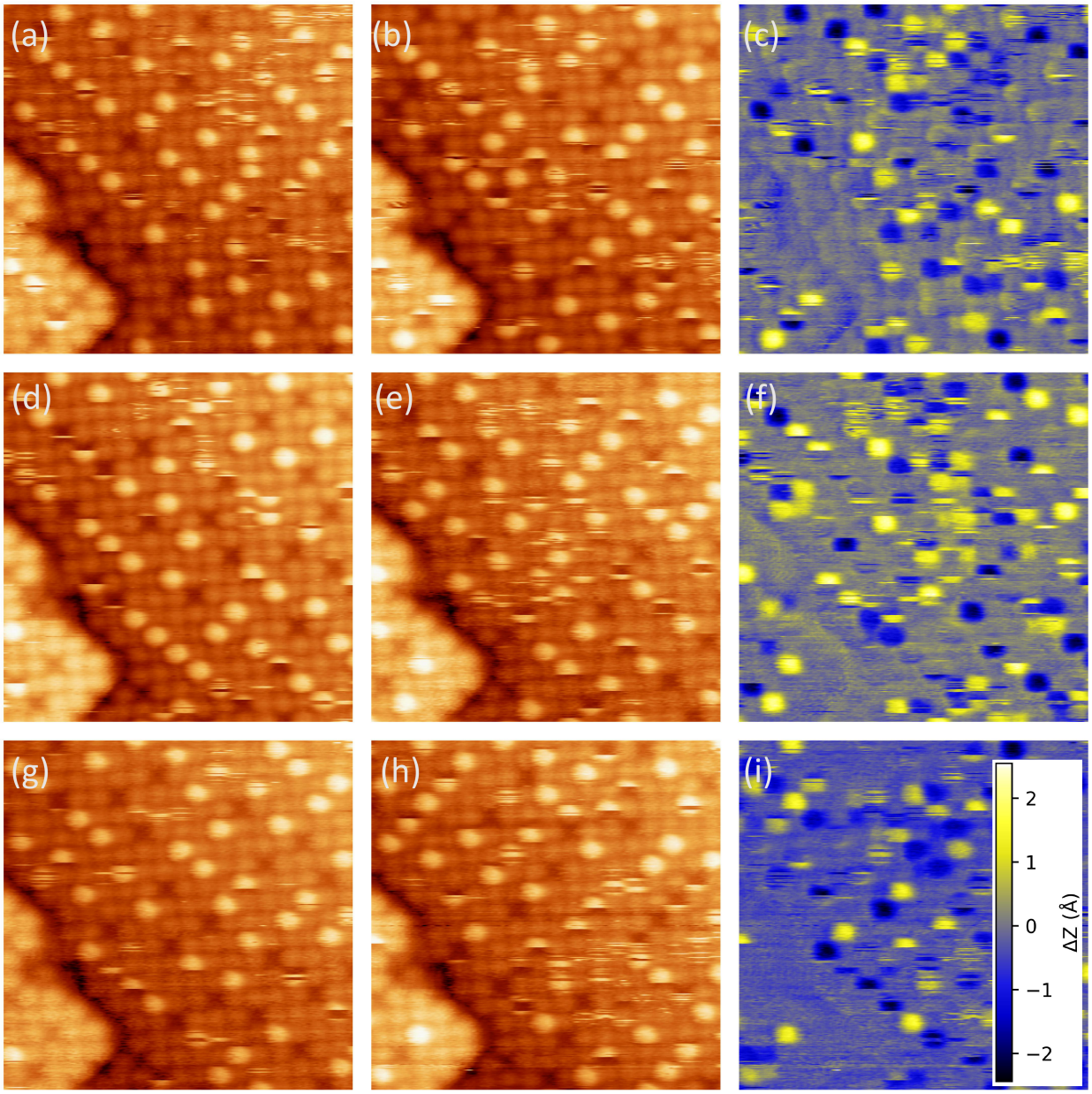


Figure 7.5: The figure illustrates atomic mobility at room temperature through sequential STM images. Panels (a), (b), (d), (e), (g), and (h) show STM images taken in sequence, capturing changes in atom positions over time. Panels (c), (f), and (i) display the subtracted images, highlighting the differences between sequential images: (c) is the subtraction of (a) and (b), (f) is the subtraction of (d) and (e), and (i) is the subtraction of (h) and (g), showing areas of atomic movement. Bright yellow color means appearance and black means disappearance of the atom on that particular spot.

Another sample was prepared by sequential deposition of CsBr at 425°C with a rate of 0.05 Å/min and $SnBr_2$ at 172°C with a rate of 0.07 Å/min on Au(100), targeting a ($SnBr_2$/CsBr) ratio of 1.4. Deposition proceeded in 0.5-minute CsBr steps, concluding with a final CsBr layer after additional alternating $SnBr_2$ and CsBr layers were deposited for 2 minutes. Figure 7.6 illustrates the resulting structure. Panels (a)–(c) present STM images of the sequentially deposited layers. The LEED pattern in panel (d), recorded at 57 eV, confirms the structural ordering of the deposited layer on the Au(100) substrate showing absence of gold reconstruction and again a (2×2) superstructure remindful of $CsSnBr_3$. Line profiles in panels (d)–(e) correspond to measurements drawn from panels (a)–(c), providing quantitative analysis of height variations and structural features across the surface. Step-height between terraces are assigned to gold steps. Locally a square-like pattern becomes apparent remindful of the perovskite structure. Unlike in other structures so far an octagon motif is visualized, marked in blue in Figure 7.6 (c), composed of 4 depressions surrounded by squares. This motif occurs regularly as seen in Figure 7.6 (b) and can also form extended structures, where several octagons are connected.

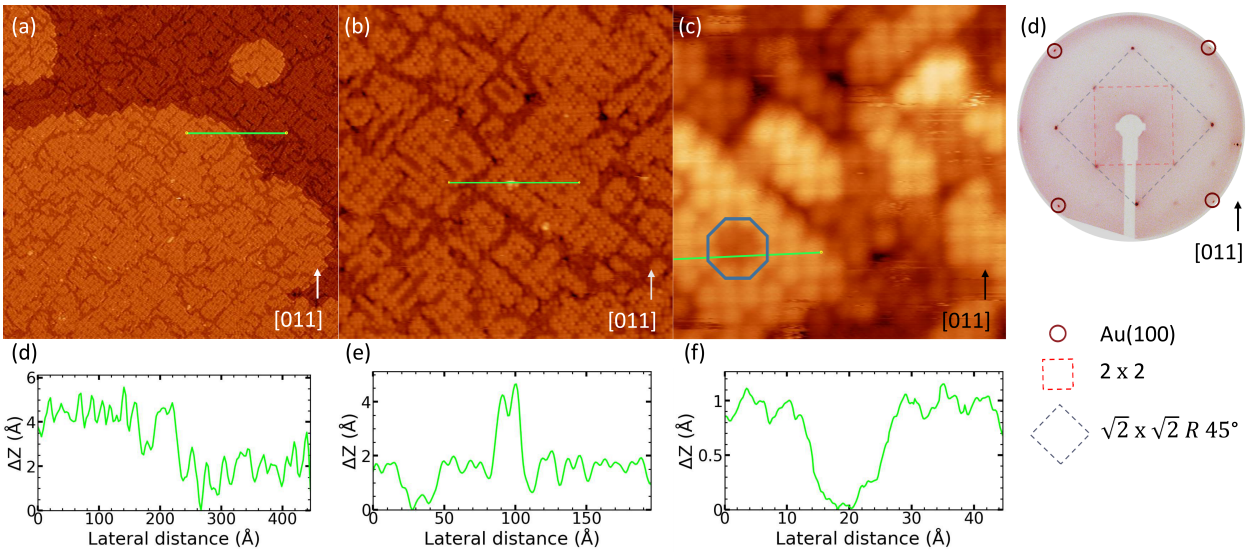


Figure 7.6: STM images of sequential deposition of CsBr and $SnBr_2$ on Au(100) are shown in (a)–(c), recorded under measurement conditions of $U_{\mathrm{Bias}} = 2\,\mathrm{V}$ and $I = 0.02\,\mathrm{nA}$. The image dimensions are: (a) $100 \times 100\,\mathrm{nm}^2$, (b) $40 \times 40\,\mathrm{nm}^2$, and (c) $10 \times 10\,\mathrm{nm}^2$. The LEED pattern in (d) was captured at 57 eV. Line profiles drawn in (a)–(c) are displayed in (d)–(e) respectively.

Figure 7.7 presents STM images taken at 5-minute intervals to capture surface mobility over time. Panels (a), (b), (d), (e), (g), and (h) show sequential STM images that reveal atomic movement on the surface. Panels (c), (f), and (i) display subtracted images, each highlighting differences between consecutive images to emphasize areas of atomic mobility: panel (c) shows the subtraction of (a) and (b), panel (f) the subtraction of (d) and (e), and panel (i) the subtraction of (g) and (h). Bright yellow spots in the subtracted images

indicate the appearance of atomic protrusions at those locations, marking areas of active atomic movement and mobility on the surface.

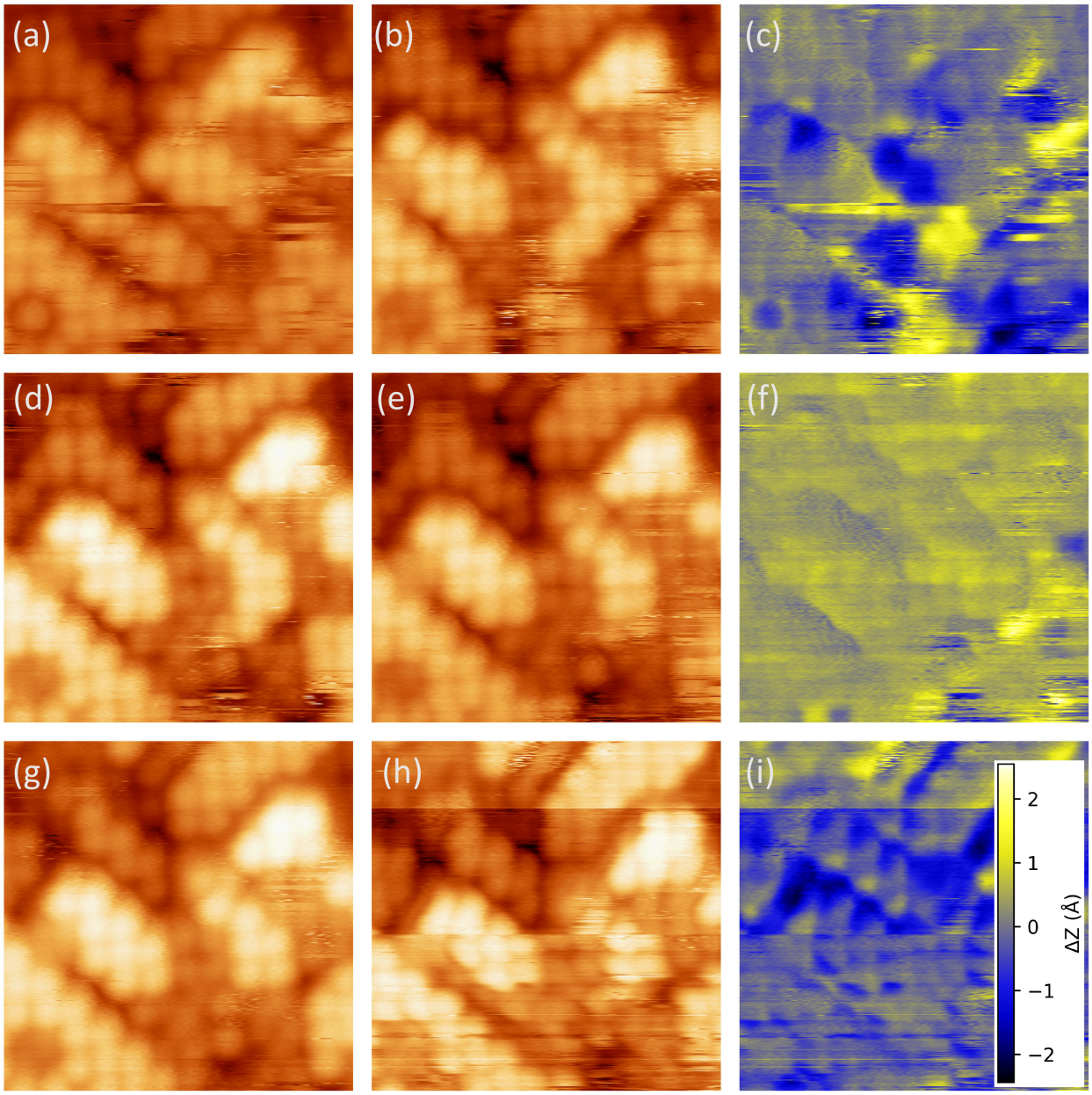


Figure 7.7: STM images illustrating surface mobility. Panels (a), (b), (d), (e), (g), and (h) show sequential STM images, capturing atomic movement on the surface over time. Panels (c), (f), and (i) display the subtracted images, with each subtraction highlighting differences between consecutive images: (c) is the subtraction of (a) and (b), (f) is the subtraction of (d) and (e), and (i) is the subtraction of (g) and (h). Bright yellow spots in the subtracted images indicate the appearance of protrusions at those locations, marking areas of atomic mobility.

7.2.2 Codeposition

This sample was prepared by co-depositing CsBr at 420°C and $SnBr_2$ at 176°C on Au(100) for 6 minutes at room temperature. Figure 7.8 illustrates the resulting structure, with STM images rotated by 45 degrees in the software during scanning. Panels (a) and (c) display STM images captured at $U_{\text{Bias}} = 1\,\text{V}$ and $I = 0.1\,\text{nA}$, with image sizes of $100 \times 100\,\text{nm}^2$ and $10 \times 4.2\,\text{nm}^2$, respectively. Figure 7.8 (c) displays a consistent spacing that aligns with the lattice constant of $CsSnBr_3$. The square structure is characteristic for the cubic CsSnBr3 perovskite. STM images were recorded at room-temperature. Additionally, the line profile in panel (e) reveals the presence of a missing atom. The LEED pattern in panel (b), recorded at 54 eV, exhibits a 2×2 structure, indicating ordered crystallographic alignment on the Au(100) substrate.

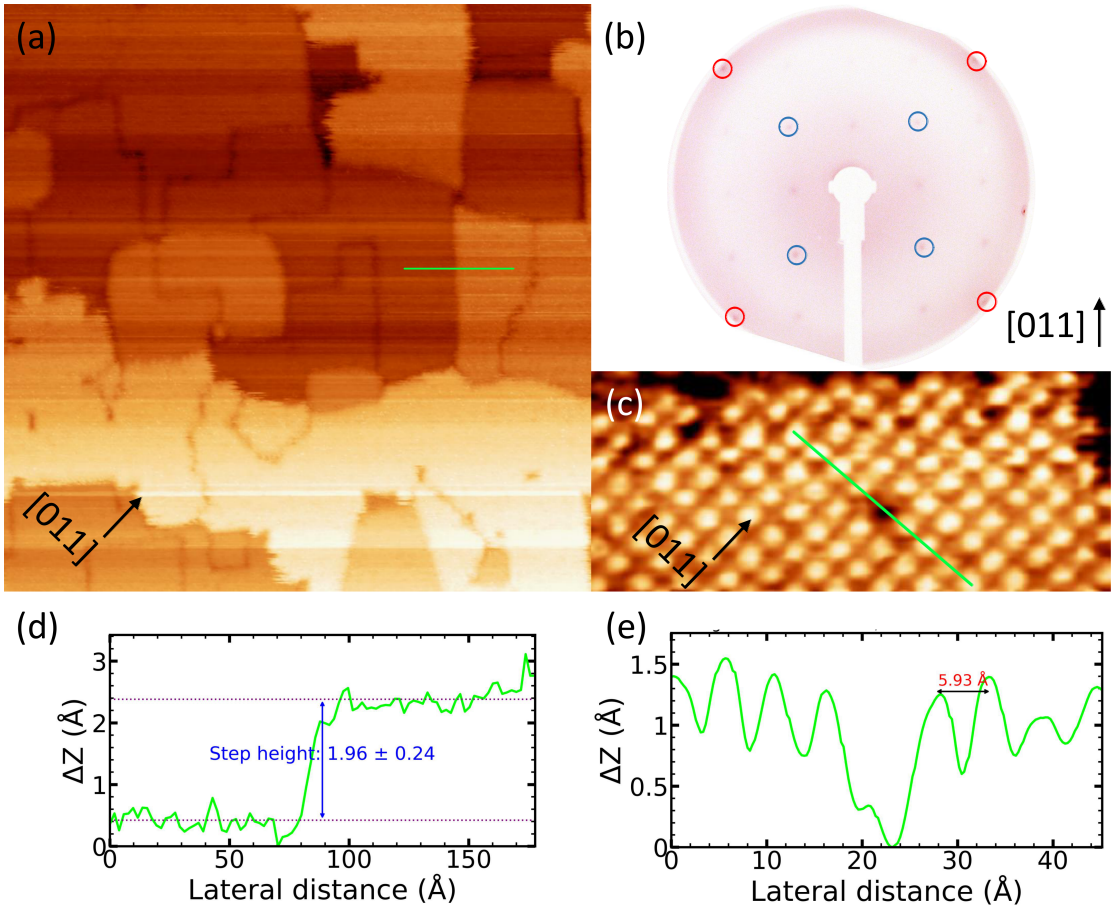


Figure 7.8: STM images of CsBr and $SnBr_2$ co-deposition on Au(100) scanned at room-temperature, rotated by 45 degrees during scanning ((a) and (c)), with measurement conditions of $U_{\text{Bias}} = 1\,\text{V}$ and $I = 0.1\,\text{nA}$. Image sizes are: (a) $100 \times 100\,\text{nm}^2$ and (c) $10 \times 4.2\,\text{nm}^2$. Panel (b) displays the LEED pattern at 54 eV. Panels (d) and (e) present line profiles drawn in (a) and (c), respectively.

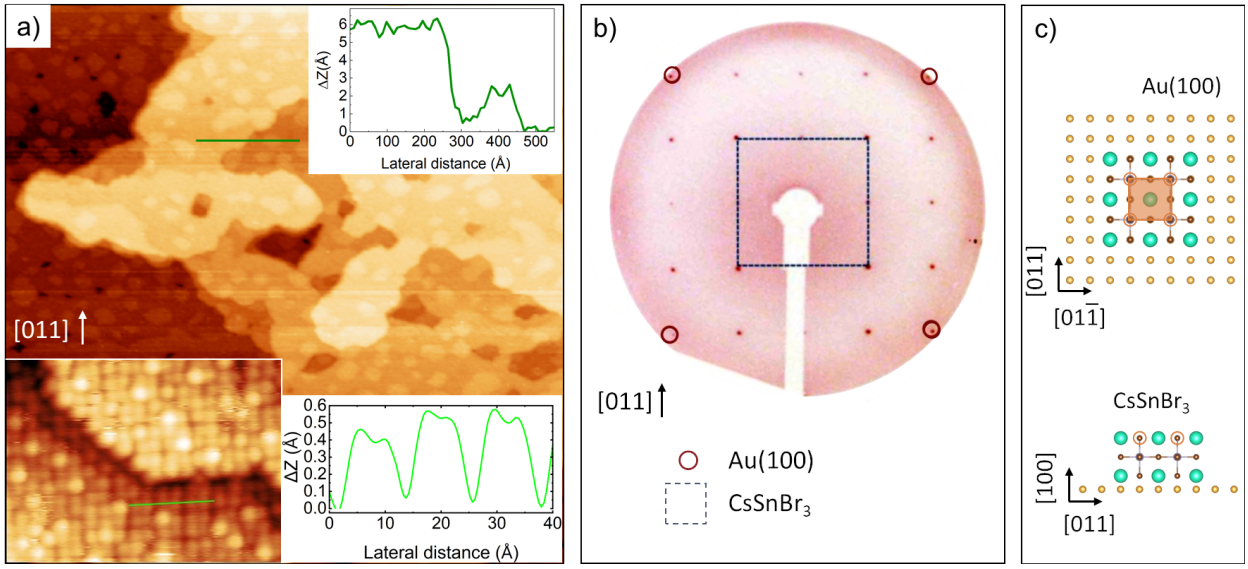


Figure 7.9: $CsSnBr_3$ on Au(100). (a) STM topography image at low-temperature. Insets provide additional detail: Left inset shows an atomic-resolution STM image, while the top right and right insets display the apparent height profiles along the green lines, providing localized surface variations. Main image parameters: $U_{\text{Bias}} = 5$ V, $I = 0.01$ nA; size: 310×310 nm^2. Inset parameters: $U_{\text{Bias}} = 2$ V, $I = 0.02$ nA; size: 10.7×8.4 nm^2. (b) LEED image acquired at 57 eV. Red circles mark the positions of gold, and dashed blue lines indicate the perovskite structure. (c) Models showing the top view (top) and side view (bottom) of the alignment of perovskite relative to Au(100). Crystallographic directions are referenced to the gold substrate. Color legend for spheres: Cs in green, Sn in grey, Br in brown, and Au in yellow.

Figure 7.9 a presents an STM image taken at low-temperature depicting a few monolayers (∼7 ML, i.e., ∼4 nm) of $CsSnBr_3$ perovskite on a Au(100) surface (the next sample). Islands of a height of 1.8 ± 0.3 Å are observed. The islands are homogeneously distributed and cover approximately 30% of the surface. Occasionally, holes are observed inside the terraces. Terrace steps are of a height of 5.8 ± 0.2 Å (see inset top Figure 7.9 a). The atomically-resolved STM image (see Figure 7.9 a inset left) reveals a square pattern that possesses the same structure as the one observed for $CsSnBr_3$ on Au(111). Although the edges of the terraces seem irregular overall, locally a preference for the edge termination along the perovskite unit cell and at an angle of 45° with respect to the square unit cell is observed. The diffraction pattern of $CsSnBr_3$ on Au(100) was measured by LEED and is depicted in Figure 7.9 b. The diffraction peaks at higher k-values marked with red circles correspond to the smaller square unit cell of the underlying Au(100) substrate. The blue dashed square at lower k-values highlights the diffraction peaks originating from the larger perovskite lattice. The LEED pattern demonstrates that the perovskite follows the symmetry of the underlying substrate. Only one orientation is observed. Using the Au(100) lattice constant [82], the lattice constant of perovskite is determined from LEED to be 5.8 ± 0.1 Å corresponding to a

(2×2) superstructure. This is in agreement with the small lattice mismatch between the two surfaces of 1.1%, when considering two unit cells of Au(100) and one unit cell of $CsSnBr_3$ (001). A model of the epitaxy of $CsSnBr_3$ on Au(100) is depicted in Figure 7.9 c showing the commensurate relationship between perovskite and the substrate.

The observed step height agrees with the height of one monolayer of perovskite. The island height, which is much lower than the height of a perovskite layer, is assigned to Au islands that have formed in the initial growth during the lifting of the Au(100) reconstruction [93].

Our microscopy and diffraction results reveal the formation of epitaxially grown tin perovskite films on Au(111) and Au(100) under ultra-high vacuum.

For solar cell applications, perovskites can be exposed to air during production and operation. To get insights into the stability of the $CsSnBr_3$ perovskite films, we performed XPS chemical analysis before and after air exposure.

Chapter 8

XPS measurement of the precursor molecules and tin halide perovskite samples

After STM and LEED investigations were conducted, X-ray photoelectron spectroscopy (XPS) was used to gain a deeper understanding of the chemical composition of the pristine precursor molecules, CsBr and $SnBr_2$, as well as of the tin perovskite films. XPS serves as a precise tool, revealing the elemental composition and chemical states within the materials. The XPS measurements were performed in an ultra-high vacuum (UHV) environment to reduce contamination and ensure accurate results. For the perovskite films, changes in the XPS spectra were monitored after air exposure, allowing the identification of chemical species that form during degradation and providing insights into the underlying mechanisms. This information is crucial for developing strategies to improve the air stability of tin perovskites and to enhance their application in clean energy technologies.

8.1 Precursors

8.1.1 CsBr on Au(111)

CsBr was deposited at 432°C with a QCM read rate of 0.06 Å/min for 6 minutes ($\sim$ 3 ML) on Au(111). This sample, along with the others which will be mentioned following, was transferred to a different ultra-high vacuum (UHV) chamber at the University of Luxembourg using a vacuum suitcase to preserve its pristine state. X-ray photoelectron spectroscopy (XPS) measurement of CsBr on Au(111) yielded spectra plotting the intensity (y-axis) of photoelectrons as a function of their binding energy (x-axis) (Figure 8.1). Distinct peaks were observed, corresponding to the elements and their chemical states.

For cesium, the spin-orbit components Cs $3d_{5/2}$ and Cs $3d_{3/2}$ were evident at binding energies of 724.42 eV and 738.37 eV, respectively (Figure 8.1 a). The peaks were modeled using a Gaussian-Lorentzian (GL(50)) lineshape, with the area ratio fixed to the expected value of

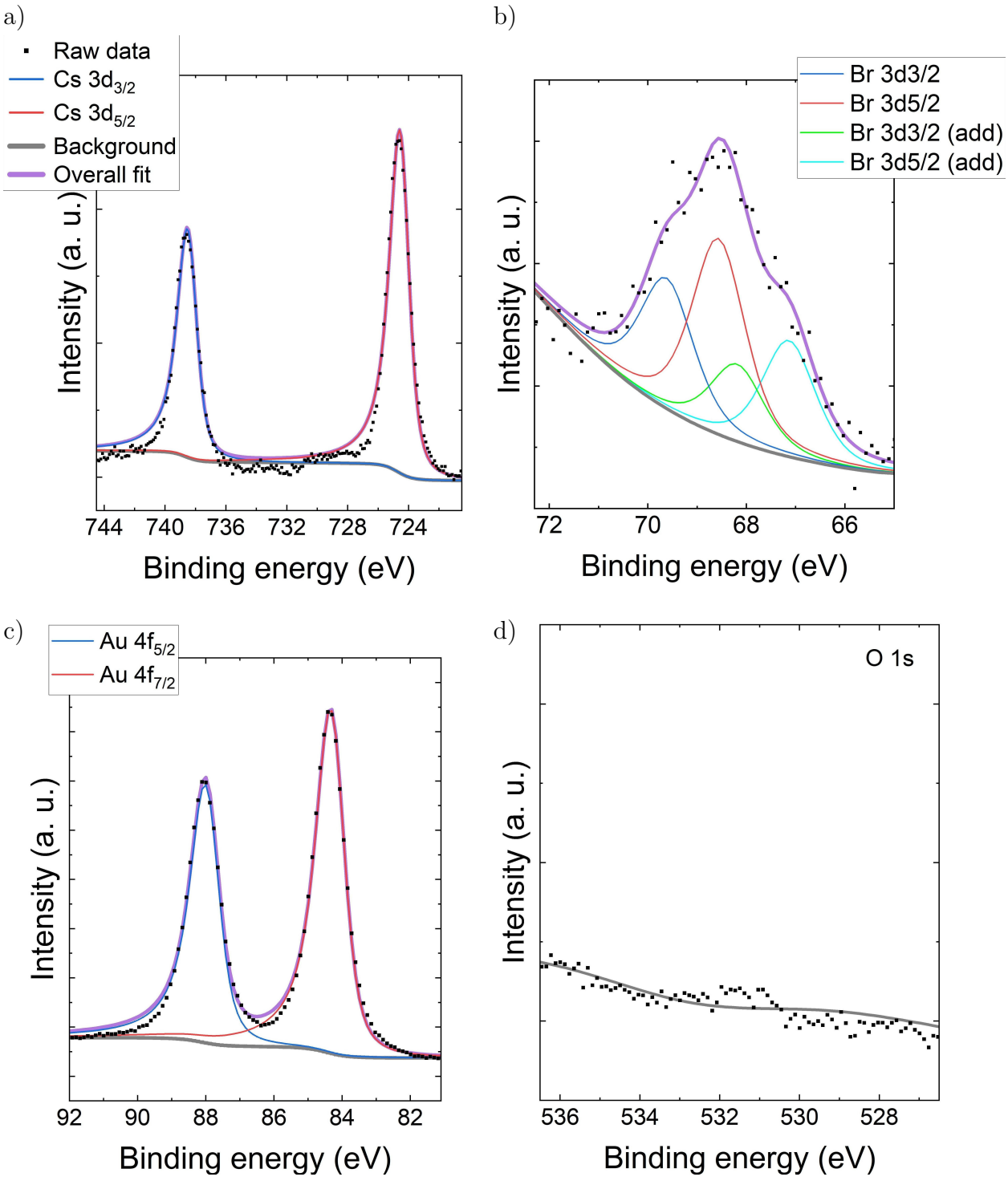


Figure 8.1: XPS data of elements from CsBr on Au(111). (a) Cs 3d spectrum with Cs $3d_{3/2}$ and Cs $3d_{5/2}$ peaks. Raw data (black dots), individual fits (blue and red lines), background (gray line), overall fit (purple). (b) Br 3d spectrum with Br $3d_{3/2}$ and Br $3d_{5/2}$ peaks, and additional components (cyan, red, green, blue lines). (c) Au 4f spectrum with Au $4f_{5/2}$ and Au $4f_{7/2}$ peaks. Individual fits (blue and red lines). (d) O 1s spectrum showing no peak.

3:2 for d orbitals. This hybrid lineshape is useful when modeling the peaks, accommodating both the Gaussian broadening effects, like instrumental resolution, and Lorentzian aspects, such as lifetime broadening [94].

Element	Area	FWHM (eV)	Position (eV)
Au $4f_{7/2}$	3831011.50	0.96	87.91
Au $4f_{5/2}$	5108015.30	0.96	84.23
Br $3d_{3/2}$	36625.44	1.3	69.62
Br $3d_{5/2}$	54938.14	1.3	68.57
Br $3d_{3/2}$ (add)	21735.1	1.3	68.19
Br $3d_{5/2}$ (add)	32602.63	1.3	67.14
Cs $3d_{3/2}$	752364.17	1.45	738.37
Cs $3d_{5/2}$	1128545.7	1.45	724.42

Table 8.1: XPS fitting parameters for CsBr on Au(111), including peak areas, FWHM, and positions.

$$\text{Elemental Ratio} = \frac{\left(\frac{\text{Area of Element A}}{\text{RSF of Element A}}\right)}{\left(\frac{\text{Area of Element B}}{\text{RSF of Element B}}\right)} \tag{8.1}$$

Element	Ratio
Br $3d_{5/2}$	0.98
Cs $3d_{5/2}$	1

Table 8.2: Elemental ratio of Br with respect to Cs on CsBr on Au(111).

The bromine 3d orbital displayed a broad peak, which was deconvoluted into two peak pairs representing distinct chemical states (Figure 8.1 b). An SGL(50) lineshape was employed for this non-metal, with a fixed energy separation of 1.05 eV [95] between spin splits and area ratios of 3:2. The peaks were located at 68.57 eV and 69.62 eV for Br $3d_{5/2}$ and Br $3d_{3/2}$, respectively, and at 67.14 eV and 68.19 eV for another set of Br $3d_{5/2}$ and Br $3d_{3/2}$.

The substrate, gold, also produced discernible peaks due to the thin film deposition. These peaks were located at 84.23 eV (Au $4f_{7/2}$) and 87.91 eV (Au $4f_{5/2}$), and were modeled using a TLA(5,95) lineshape, maintaining the expected 4:3 ratio for the f orbital.

Notably, the sample was found to be clean, with no apparent O 1s peak indicating minimal oxygen contamination (Figure 8.1 d).

The elemental ratio of Cs to Br, calculated using peak areas and relative sensitivity factors (RSF) from [96] using Equation 8.1 , was found to be approximately 1:0.98 (Table

8.2). This is close to the expected 1:1 stoichiometry for CsBr. The additional peaks observed in the Br spectrum may indicate the presence of a different bromine-containing species or chemical state on the surface (e.g. Br in a different chemical environment or dissociation). XPS fitting parameters for CsBr on Au(111) can be found in Table8.1.

The XPS analysis of CsBr on Au(111) provides detailed insights into the elemental composition and chemical states of the surface. The data indicates a successful deposition of CsBr with a nearly 1:1 stoichiometric ratio of Br to Cs, and well-defined electronic states for gold, bromine, and cesium. This analysis is essential for understanding the surface chemistry and verifying the integrity of the deposited layer.

8.1.2 $SnBr_2$ on Au(111)

Approximately 4 ML of $SnBr_2$ was deposited on Au(111) at the precursor temperature of 174°C with a QCM read rate of 0.04 Å/min for 6 minutes at room temperature. In the XPS data of Sn 3d (Figure 8.2 a), we observe two distinct peaks corresponding to the spin-orbit components Sn $3d_{5/2}$ and Sn $3d_{3/2}$. These peaks are differentiated by their binding energies, with the Sn $3d_{5/2}$ peak at a lower binding energy and Sn $3d_{3/2}$ at higher. The peaks were fitted using a TLA(5,95) lineshape [19] to account for the peak broadening and shape accurately. After fixing the energy separation between these peaks to be 8.41 eV, and the ratios of the area under the curves 3:2 since it is a d orbital, we get the right fit for the peaks. The peaks at slightly higher energy can be assigned to the Sn^{2+} and lower metallic Sn^0 state of Sn $3d_{3/2}$ and Sn $3d_{5/2}$ based on reference measurements on a piece of tin foil [19]. The fitting parameters can be found in Table 8.3.

For bromine, we observe 3d orbital with respective spin-orbit components (Figure 8.2 b). This broad peak can be fitted with 2 couples of peaks, each corresponding to the different chemical states. For this case again, we use SGL(50) lineshape, which is used for non-metals. The peaks for Br $3d_{5/2}$ and $3d_{3/2}$ are located at 67.06 eV, 68.11 eV, 68.49 eV, and 69.54 eV, respectively (Figure 8.2 b). The other parameters can also be found in Table 8.3.

The substrate peaks can also be seen always in these samples, since we deposited ultrathin films. Figure 8.2 c shows the gold peaks. We used TLA(5,95) lineshape for this metal, fixing the 4:3 ratio for the f orbital.

The sample was checked for the oxygen contamination as well, and it seemed rather clean with no significant peak of the O 1s (Figure 8.2 d).

The ratio for Br $3d_{5/2}$ is 1.78 with respect to Sn $3d_{5/2}$, which deviates from the expected 1:2 stoichiometry. This discrepancy can be attributed to the dissociation of $SnBr_2$ and the desorption of Br_2 gas. The loss of Br_2 through desorption reduces the relative amount of bromine detected in the XPS measurements, resulting in a lower than expected Br/Sn ratio (see Table 8.4).

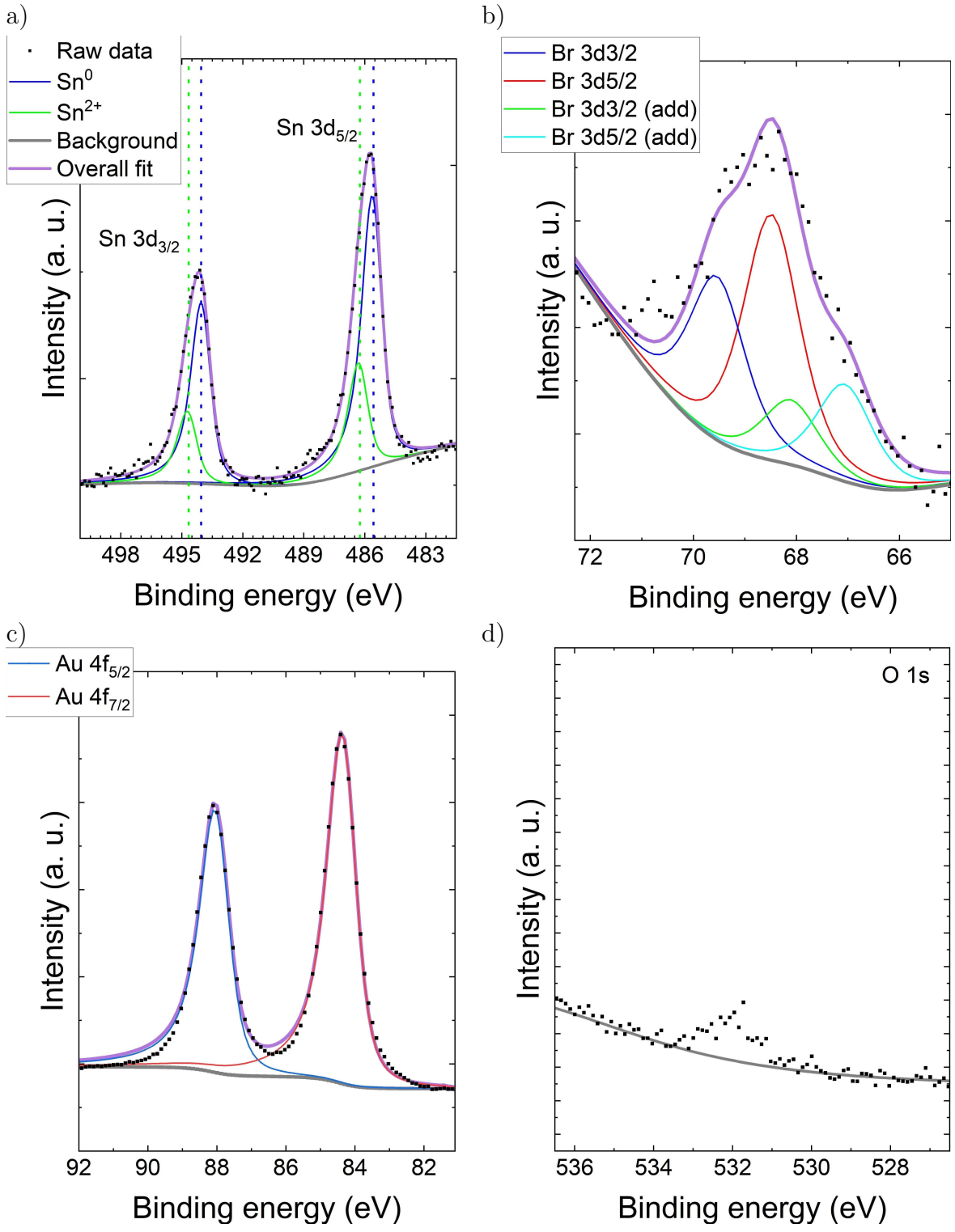


Figure 8.2: XPS data of elements from $SnBr_2$ on Au(111). (a) Sn 3d spectrum with Sn $3d_{3/2}$ and Sn $3d_{5/2}$ peaks. Raw data (black dots), individual fits (blue and green lines), background (gray line), overall fit (purple). (b) Br 3d spectrum with Br $3d_{3/2}$ and Br $3d_{5/2}$ peaks, and additional components (cyan, red, green, blue lines). (c) Au 4f spectrum with Au $4f_{5/2}$ and Au $4f_{7/2}$ peaks. Individual fits (blue and red lines). (d) O 1s spectrum showing no significant peak.

Element	Area	FWHM (ev)	Position (eV)
Au $4f_{5/2}$	4160286.10	0.92	87.96
Au $4f_{7/2}$	5547048.10	0.92	84.28
Br $3d_{3/2}$	52808.96	1.3	69.54
Br $3d_{5/2}$	79213.4	1.3	68.49
Br $3d_{3/2}$ (add)	20891.23	1.3	68.11
Br $3d_{5/2}$ (add)	31336.83	1.3	67.06
Sn^0 $3d_{3/2}$	212011.89	0.88	493.90
Sn^0 $3d_{5/2}$	318017.67	0.88	485.49
Sn^{2+} $3d_{3/2}$	123241.64	0.88	494.56
Sn^{2+} $3d_{5/2}$	184862.37	0.88	486.15

Table 8.3: $SnBr_2$ on Au(111).

Element	Ratio
Br $3d_{5/2}$	1.78
Sn $3d_{5/2}$	1

Table 8.4: Element ratios with respect to Sn on $SnBr_2$ on Au(111).

8.2 Perovskite samples

8.2.1 $CsSnBr_3$ on Au(100)

An ultrathin film was deposited onto the Au(100) substrate by co-depositing CsBr and $SnBr_2$ for 45 minutes at room temperature. Figure 8.3 shows XPS data of the Sn 3d core levels recorded on ∼10 ML film of $CsSnBr_3$ on Au(100) in UHV before (upper panel) and after (lower panel) air exposure. The fitting parameters: peak position, peak width, and area are listed in Table 8.5. Starting with the pristine case, we find that the spectra can be fitted with two pairs of peaks. One pair is at the positions of 495.03 eV and 486.62 eV. The separation between the peaks was fixed following the known value of 8.41 eV due to spin-orbit coupling (SOC) [95], as well as their intensity ratio was fixed to 3:2 during the fitting procedure. The peaks (green line) are assigned to the Sn^{2+} state of Sn $3d_{3/2}$ and Sn $3d_{5/2}$ [19]. A closer look at the right shoulder of the XPS data in the Sn 3d range reveals a second set of peaks at slightly lower binding energies of 494.19 eV and 485.78 eV (blue line). These are associated with metallic tin (Sn^0). Peaks at positions of the Sn^{4+} state did not improve the overall fitting curve, allowing us to discard the possible presence of oxidized Sn^{4+} state in the pristine tin perovskite films grown in UHV.

This is an important result as in all solution-based preparations the Sn^{4+} state is present. Here, the absence of the Sn^{4+} state shows that the preparation without solvents and only using molecule precursors deposited by PVD stabilizes the Sn^{2+} oxidation state. The peaks at slightly lower energies are assigned to Sn^0 (19% of the total area). We ascribe this to the interaction of the precursor molecules, in particular $SnBr_2$ with the gold surface, leading to a dissociation of the molecules and thus the metallic Sn^0 state. In thicker films (>100 nm) of a different tin perovskite, the metallic state has not been observed [19].

The samples have been taken out of the UHV chamber, exposed to air for 1 hour, and then inserted back into the UHV chamber. The spectrum has been fitted in the same way as the pristine sample. A pair of new peaks appear now at higher binding energies at positions 495.91 eV and 487.50 eV (see Table 8.6). These are assigned to the spin-orbit split peaks of the Sn^{4+} state. The Sn^{4+} peak is now the dominating peak (62% of the total area). Sn^{2+} is still present (38%) at the same energy position, while the Sn^0 has completely vanished. This demonstrates that the sample has undergone oxidation: Sn^{2+} has been converted to Sn^{4+} and Sn^0 has been converted to Sn^{2+} and Sn^{4+}.

These findings reveal the advantage of the PVD growth method in ultra-high vacuum, preventing any undesired oxidation of the tin perovskite. In addition, it demonstrates the need to encapsulate tin perovskite films directly in vacuum, prior to any exposure to ambient conditions. As soon as $CsSnBr_3$ perovskite is exposed to air, it will produce unwanted Sn^{4+} oxidation states, reducing the stability and therefore performance of the perovskite solar cell devices.

The analysis of the oxygen O 1s peak that occurs after air exposure is deconvoluted into three peaks at 530.91 eV, 531.98 eV, and 532.91 eV (see Figure 8.4 d) and Table 8.6). Following the XPS results on SnO_2 nanosheets showing a similar behavior [97], the peaks

are assigned to oxygen in SnO_2 (pristine), SnO_2 (oxygen deficient regions), and adsorbed oxygen species, respectively.

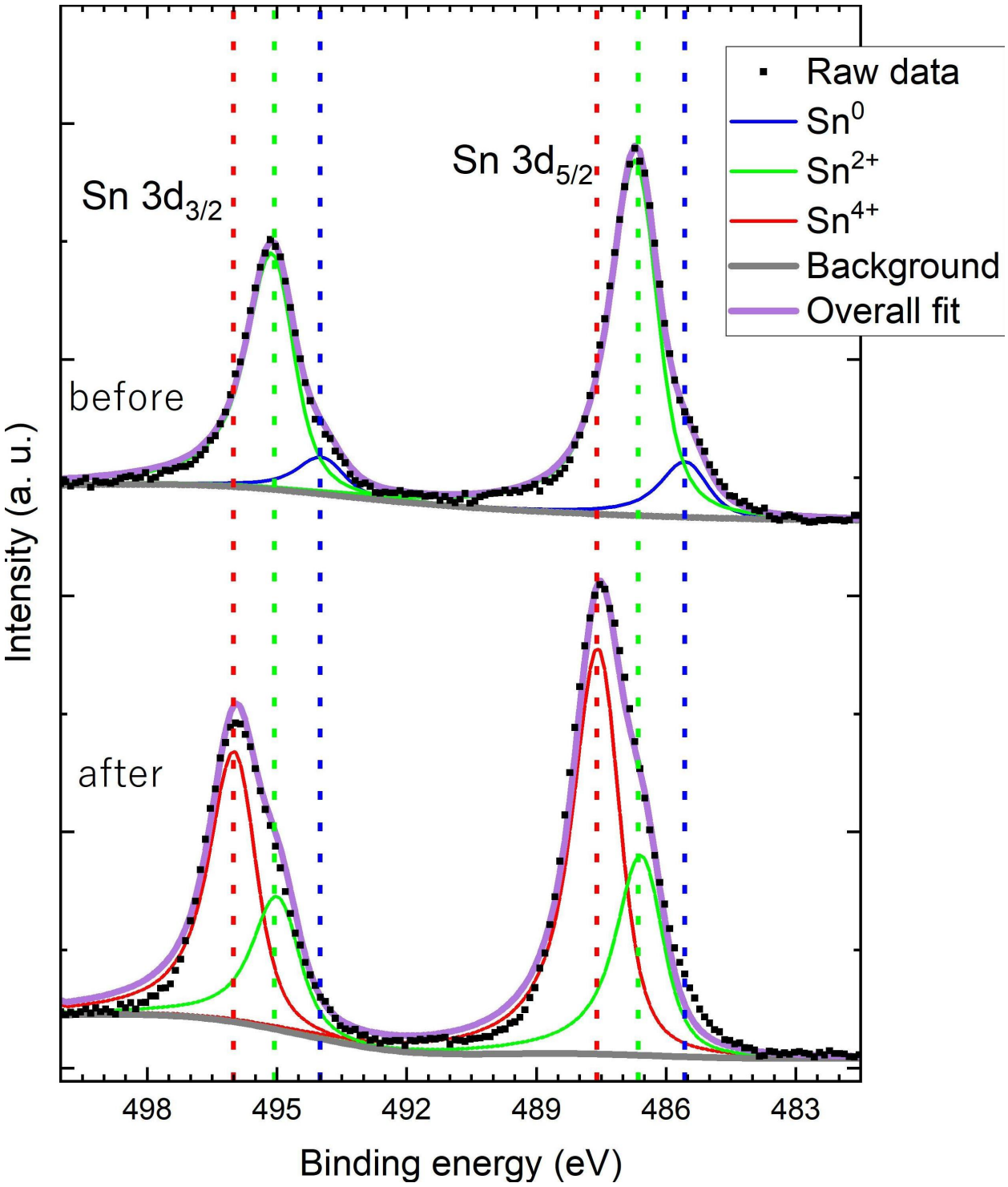


Figure 8.3: XPS spectra of Sn 3d core levels on $CsSnBr_3$ on Au(100) before and after air exposure. Measurement before air exposure has been shifted up for clarity.

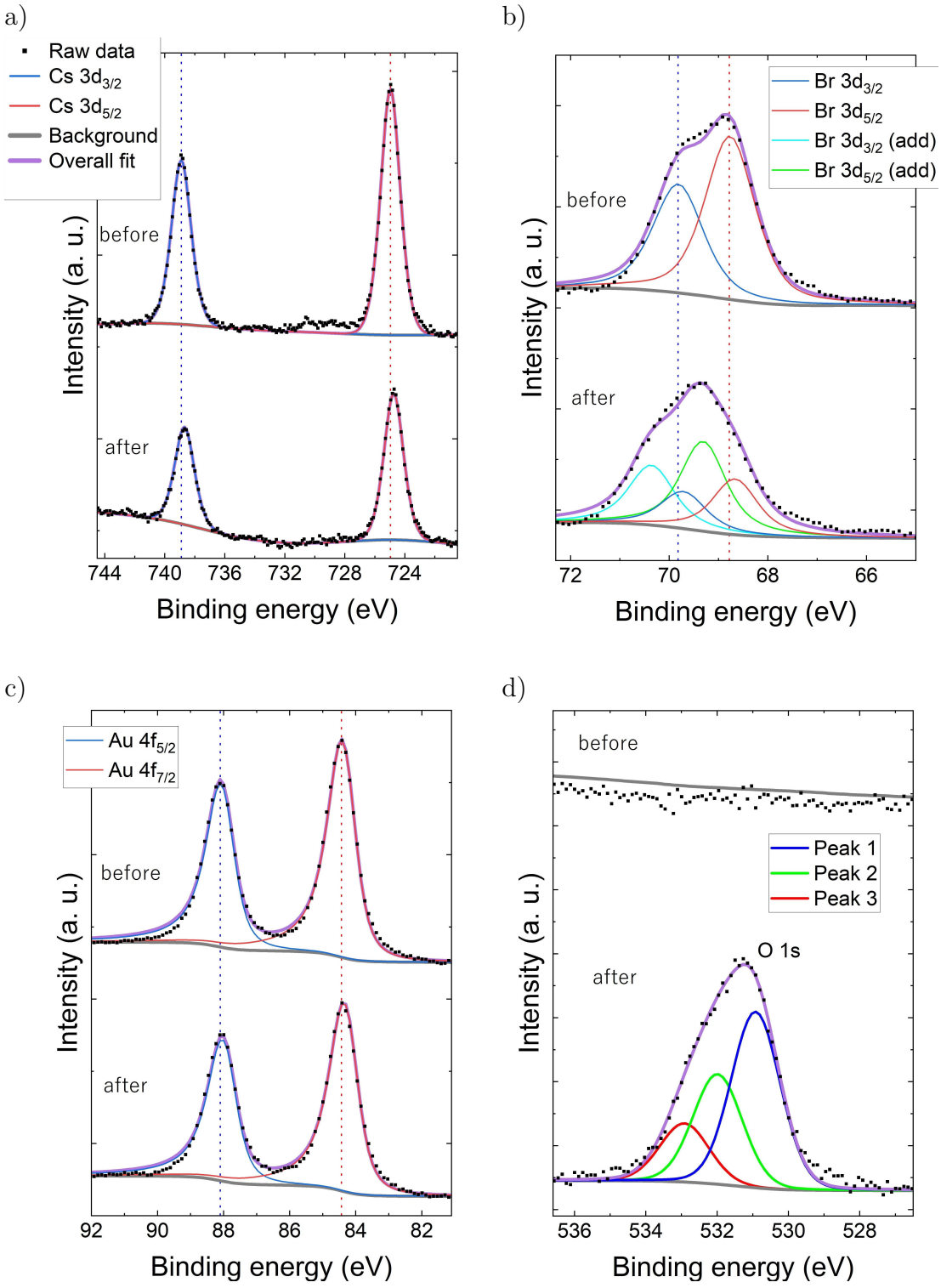


Figure 8.4: XPS data of elements on thick $CsSnBr_3$ on Au(100). (a) Cs 3d spectrum with Cs $3d_{3/2}$ and Cs $3d_{5/2}$ peaks. Raw data (black dots), individual fits (blue and red lines), background (gray line), overall fit (purple). (b) Br 3d spectrum with Br $3d_{3/2}$ and Br $3d_{5/2}$ peaks, and additional components (cyan, red, green, blue lines). (c) Au 4f spectrum with Au $4f_{5/2}$ and Au $4f_{7/2}$ peaks. Individual fits (blue and red lines). (d) O 1s spectrum showing three peaks.

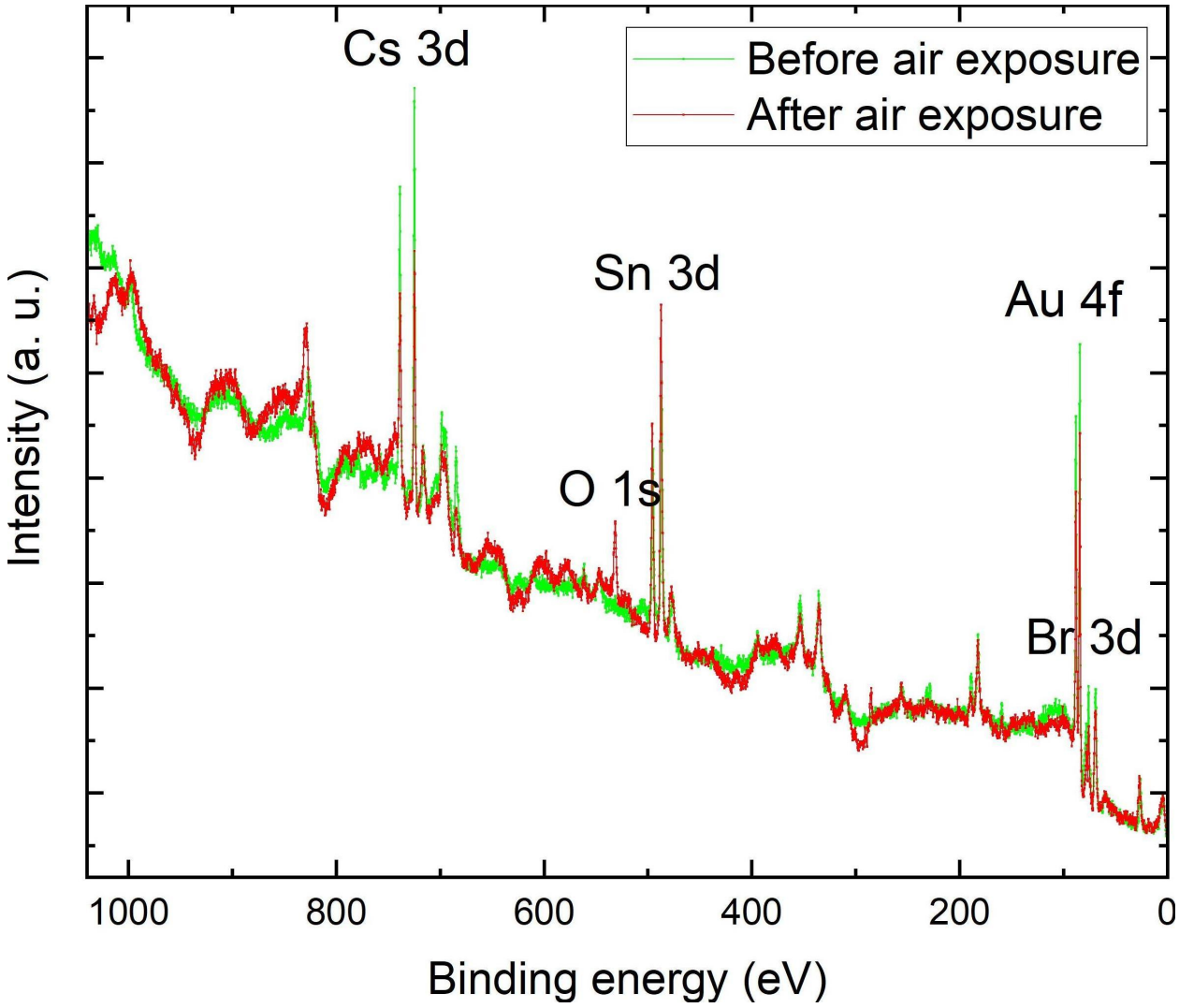


Figure 8.5: Survey spectra of $CsSnBr_3$ on Au(100).

We have further analyzed the other elements, namely Cs and Br (see Figure 8.4 a) and b)). Peaks at 738.89 eV and 724.95 eV are assigned to the spin-orbit split peaks Cs $3d_{3/2}$ and Cs $3d_{5/2}$, while peaks at 69.81 eV and 68.76 eV are assigned to the spin-orbit split peaks Br $3d_{3/2}$ and Br $3d_{5/2}$. After exposure to air, the Cs peaks shift slightly by 0.21 eV to lower binding energy (Table 8.6) and for Br, we obtain besides the original peaks an additional doublet of peaks at 0.6 eV higher binding energy. The energy of the Cs peak is in line with oxidized Cs [98], however, as only a small shift occurs, could also be explained by Cs in a different chemical environment. The additional Br peaks at higher binding energy can be attributed to anionic Br [99], becoming available due to the preferential binding of Sn to O instead of Br. The ratios before exposure to air of the elements follow closely the 1:1:3 ratios as expected for $CsSnBr_3$. However, after air exposure, the amount of Cs has dropped to 0.43 and for Br to 1.94 (Table 8.8), revealing a significant reduction in the amount of these elements compared to Sn (Figure8.5), which was taken as a reference to calculate the

Element	Area	FWHM (eV)	Position (eV)
Au $4f_{5/2}$	1637554.5	0.95	87.96
Au $4f_{7/2}$	2183406.0	0.95	84.31
Br $3d_{3/2}$	342708.6	1.20	69.81
Br $3d_{5/2}$	514062.7	1.20	68.76
Cs $3d_{3/2}$	1523233.9	1.54	738.89
Cs $3d_{5/2}$	2284849.6	1.54	724.95
Sn^0 $3d_{3/2}$	178008.8	1.10	494.19
Sn^0 $3d_{5/2}$	267013.0	1.10	485.78
Sn^{2+} $3d_{3/2}$	756547.2	1.10	495.03
Sn^{2+} $3d_{5/2}$	1134820.2	1.10	486.62

Table 8.5: XPS data before air exposure from the thick $CsSnBr_3$ on Au(100).

Element	Area	FWHM (eV)	Position (eV)
Au $4\,f_{5/2}$	1451115.1	0.97	87.93
Au $4\,f_{7/2}$	1934820.1	0.97	84.25
Br $3\,d_{3/2}$	97114.8	1.14	69.73
Br $3\,d_{5/2}$	197173.8	1.14	68.68
Br $3\,d_{3/2}$(add)	192759.4	1.14	70.39
Br $3\,d_{5/2}$(add)	289139.0	1.14	69.34
Cs $3\,d_{3/2}$	906049.4	1.54	738.68
Cs $3\,d_{5/2}$	1359073.4	1.54	724.74
O 1 s(peak 1)	248679.2	1.62	530.91
O 1 s(peak 2)	155540.9	1.62	531.98
O 1 s(peak 3)	82910.6	1.62	532.91
Sn^{2+} $3\,d_{3/2}$	511666.4	1.10	495.01
Sn^{2+} $3\,d_{5/2}$	767499.2	1.10	486.60
Sn^{4+} $3\,d_{3/2}$	846833.3	1.10	495.91
Sn^{4+} $3\,d_{5/2}$	1270249.4	1.10	487.50

Table 8.6: XPS data after air exposure from the $CsSnBr_3$ on Au(100).

chemical ratio. The origin of the reduction of Cs and Br content and the simultaneous increase in overall Sn intensity is intriguing. We can initially speculate that some of the Br forms Br_2 and desorbs as a gas. However, for Cs, no gases are known which could be formed. A diffusion of Cs inside Au might be one possibility, but Cs is a rather large ion and not likely to diffuse into the metal. However, if Cs diffuses just to the interface of the adlayer

Element	E_{before} - E_{after} (eV)
Au $4f_{5/2}$	<0.10
Au $4f_{7/2}$	<0.10
Br $3d_{3/2}$	<0.10
Br $3d_{5/2}$	<0.10
Cs $3d_{3/2}$	0.21
Cs $3d_{5/2}$	0.21
Sn^{2+} $3d_{3/2}$	<0.10
Sn^{2+} $3d_{5/2}$	<0.10

Table 8.7: Difference in energies before and after air exposure thick $CsSnBr_3$. remember to change for all

Element	Ratio Relative to Sn Before	Ratio Relative to Sn After
Sn $3d_{5/2}$	1	1
Cs $3d_{5/2}$	1.04	0.43
Br $3d_{5/2}$	2.98	1.94

Table 8.8: Ratios of elements relative to Sn before and after air exposure thick $CsSnBr_3$.

with the gold surface, while Sn remains on top, still an intensity difference in XPS could be measured despite the total amount on the surface being the same. Photoelectrons emitting from the interface have to cross the whole adlayer, while photoelectrons from the top will not be hampered leading to an intensity difference. Thus, on the top layer tin oxide is formed and Cs and Br might have partially diffused to lower layers. The decrease of Cs amount is higher than that of Br, therefore a formation of metallic Cs via a reducing reaction and subsequent evaporation may take place as well [100]. The observed decrease in Au intensity (see Figure 8.4 c) and Tables 8.5 and 8.6) is an additional demonstration of the formation of an oxide layer at the top surface, increasing the thickness of the adlayer and thus decreasing the intensity of gold recorded by XPS. We note, LEED measurements after air exposure do not show any crystalline structure anymore, supporting the view of detrimental changes due to air exposure. The formation of tin oxide is particularly critical as it has a band-gap larger than 3 eV [101–103], which will affect the charge transport and light harvesting properties of the perovskite layer in a device.

8.2.2 $CsSnBr_3$ on Au(111)

In order to determine the influence of the substrate, we prepared $CsSnBr_3$ on Au(111). The Au(111) substrate was prepared for thin film deposition through sputtering and annealing processes. The substrate's surface quality was confirmed by LEED before and after thin film deposition. A thin film was prepared by co-depositing CsBr and $SnBr_2$ at an intended 1:1 ratio, and its quality was again checked by LEED.

For $CsSnBr_3$ on Au(111), XPS data of the Sn 3d core levels were analyzed before and after air exposure. Figure 8.6 shows the XPS data of Sn 3d from $CsSnBr_3$ on Au(111) with an intended 1:1 ratio of the precursors. The XPS data for the other elements from the same sample are shown in Figure 8.7. In the pristine state, the spectra revealed two pairs of peaks. One pair, located at 494.95 eV and 486.54 eV, corresponds to the Sn^{2+} state of Sn $3d_{3/2}$ and Sn $3d_{5/2}$, respectively. Another set of peaks at slightly lower binding energies, 494.19 eV and 485.78 eV, is attributed to metallic tin (Sn^0).

Upon exposure to air, new peaks emerged at higher binding energies as in the previous sample discussed (495.83 eV and 487.42 eV), which are characteristic of the Sn^{4+} state. The Sn^{4+} peak became the dominant feature, while the Sn^0 state was no longer present which suggests that Sn^{2+} was oxidized to Sn^{4+} and Sn^0 converted to both Sn^{2+} and Sn^{4+} [19].

The analysis of the oxygen O 1s peak after air exposure showed three distinct peaks at 530.79 eV, 531.97 eV, and 532.97 eV, corresponding to oxygen in SnO_2 (pristine), SnO_2 (oxygen-deficient regions), and adsorbed oxygen species, respectively [97]. For Cs and Br, the XPS data indicated peaks at 738.92 eV and 724.98 eV for Cs $3d_{3/2}$ and Cs $3d_{5/2}$, and at 69.79 eV and 68.74 eV for Br $3d_{3/2}$ and Br $3d_{5/2}$. After air exposure, the Cs peaks shifted by 0.37 eV to lower binding energies, while additional peaks for Br appeared at both higher and lower binding energies, indicating changes in their chemical environments (see Table 8.10).

The elemental ratios of $CsSnBr_3$ were not consistent with the expected stoichiometry (see Table 8.12) this can be due to the dissociation at the surface when the coverage is low. After air exposure, the proportions of Cs and Br relative to Sn decreased significantly, suggesting diffusion or evaporation. The decrease in Cs and Br content, combined with an increase in overall Sn intensity, indicates that Br might have formed Br_2 gas and desorbed, whereas Cs could have diffused to the interface of the adlayer with the gold surface. The greater reduction in Cs compared to Br implies that metallic Cs may have evaporated. The observed decrease in Au intensity suggests the formation of an oxide layer on the top surface.

The choice of Au(111) in our study aimed, in a way, to simulate the grain boundary effects in perovskite films, leveraging its hexagonal symmetry to mimic the atomic structure that promotes grain boundary formation. As noted in references [104, 105], the role of grain boundaries in hybrid perovskite solar cells was crucial for understanding charge transport and stability. By using Au(111), we observed the influence of grain boundaries on the XPS data. This approach differed from Au(100), where the square symmetry did not as closely replicate the natural structure of grain boundaries in these materials. Consequently, Au(111) provided unique insights into substrate-perovskite interactions that were not as prominent with Au(100), particularly in terms of grain boundary simulation.

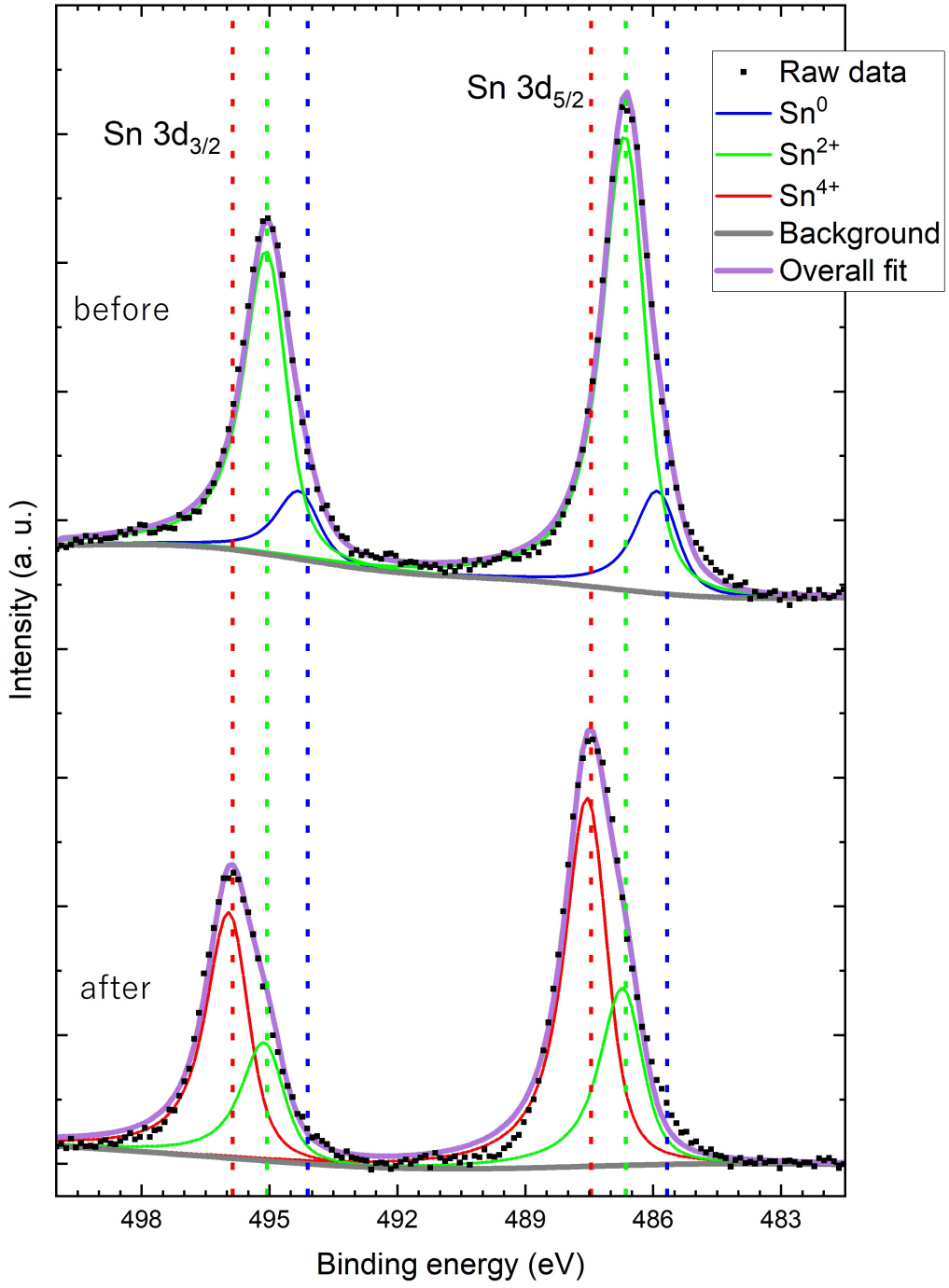


Figure 8.6: XPS data of Sn 3d from $CsSnBr_3$ on Au(111) with 1 to 1 ratio of the precursors.

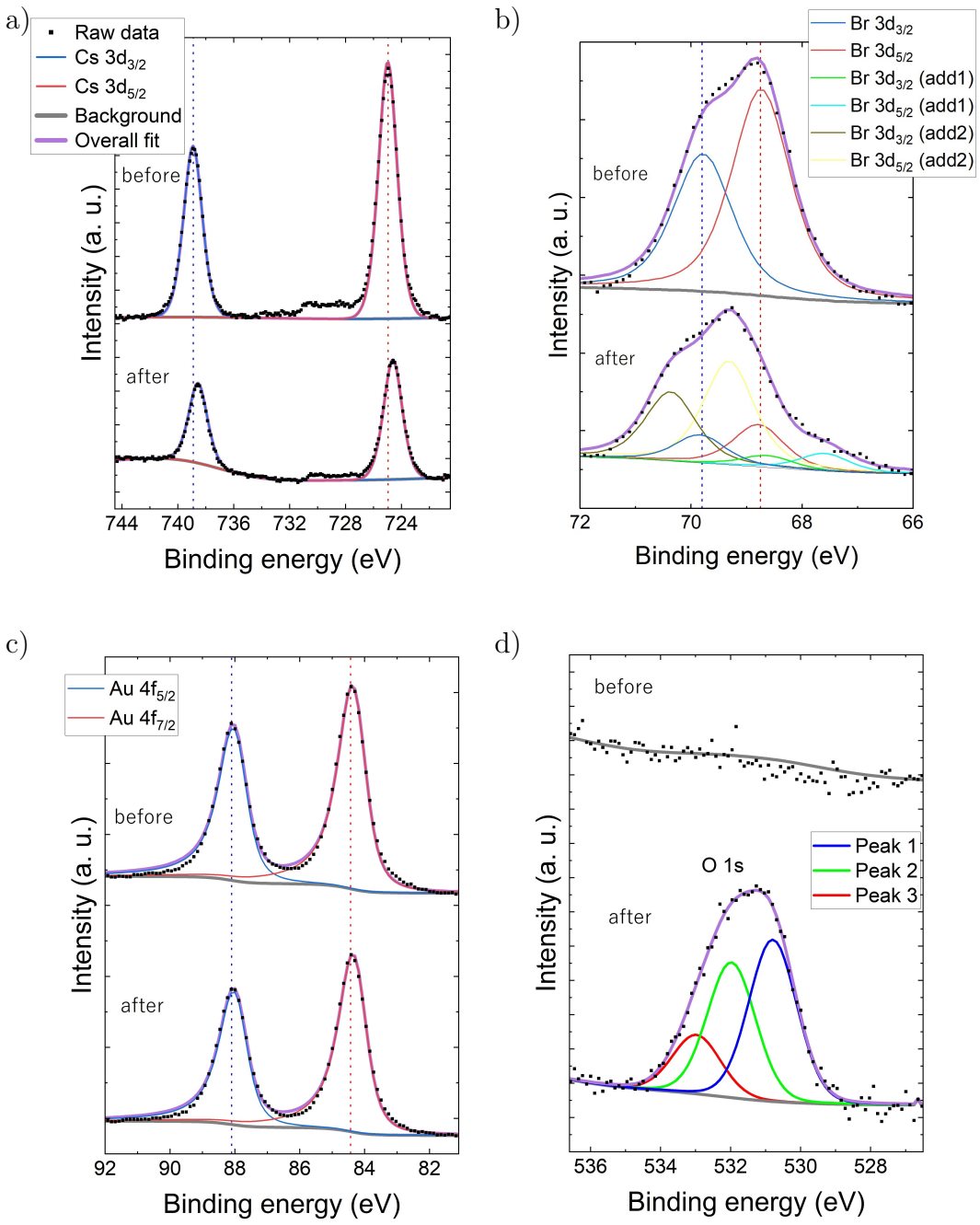


Figure 8.7: XPS data of elements on $CsSnBr_3$ on Au(111) with intended 1 to 1 precursor ratio. (a) Cs 3d spectrum with Cs $3d_{3/2}$ and Cs $3d_{5/2}$ peaks. Raw data (black dots), individual fits (blue and red lines), background (gray line), overall fit (purple). (b) Br 3d spectrum with Br $3d_{3/2}$ and Br $3d_{5/2}$ peaks, and additional components (cyan, red, green, blue, brown, yellow lines). (c) Au 4f spectrum with Au $4f_{5/2}$ and Au $4f_{7/2}$ peaks. Individual fits (blue and red lines). (d) O 1s spectrum showing three peaks.

Element	Area	FWHM (eV)	Position (eV)
Au $4f_{5/2}$	3159063.7	0.96	87.94
Au $4f_{7/2}$	4212085	0.96	84.27
Br $3d_{3/2}$	294196.09	1.26	69.79
Br $3d_{5/2}$	441293.92	1.26	68.74
Cs $3d_{3/2}$	1773931.9	1.57	738.92
Cs $3d_{5/2}$	2660896.6	1.57	724.98
Sn^0 $3d_{3/2}$	177511.18	1.1	494.19
Sn^0 $3d_{5/2}$	266266.64	1.1	485.78
Sn^{2+} $3d_{3/2}$	789123.61	1.1	494.95
Sn^{2+} $3d_{5/2}$	1183684.8	1.1	486.54

Table 8.9: XPS data before air exposure from $CsSnBr_3$ on Au(111) with intended 1 to 1 precursor ratio.

Element	Area	FWHM (eV)	Position (eV)
Au $4f_{5/2}$	2747896.1	0.96	87.93
Au $4f_{7/2}$	3663861.5	0.96	84.25
Br $3d_{3/2}$ (add1)	127037.1	1.08	70.37
Br $3d_{5/2}$ (add1)	190555.55	1.08	69.32
Br $3d_{3/2}$	51799.26	1.08	69.84
Br $3d_{5/2}$	77698.85	1.08	68.79
Br $3d_{3/2}$ (add2)	21692.43	1.08	68.64
Br $3d_{5/2}$ (add2)	32538.63	1.08	67.59
Cs $3d_{3/2}$	827684.69	1.57	738.55
Cs $3d_{5/2}$	1241526.4	1.57	724.61
O 1s (Peak 1)	170697.21	1.62	530.79
O 1s (Peak 2)	142735.63	1.62	531.97
O 1s (Peak 3)	62293.29	1.62	532.97
Sn^{2+} $3d_{3/2}$	308170.69	1.1	495.01
Sn^{2+} $3d_{5/2}$	462255.8	1.1	486.60
Sn^{4+} $3d_{3/2}$	639868.21	1.1	495.83
Sn^{4+} $3d_{5/2}$	959801.83	1.1	487.42

Table 8.10: XPS data after air exposure from $CsSnBr_3$ on Au(111) with intended 1 to 1 precursor ratio.

Element	$E_{\textbf{before}} - E_{\textbf{after}}$ **(eV)**
Au $4f_{5/2}$	0.01
Au $4f_{7/2}$	0.02
Br $3d_{3/2}$	−0.05
Br $3d_{5/2}$	−0.05
Cs $3d_{3/2}$	0.37
Cs $3d_{5/2}$	0.37
Sn^{2+} $3d_{3/2}$	−0.06
Sn^{2+} $3d_{5/2}$	−0.06

Table 8.11: Energy differences before and after air exposure from $CsSnBr_3$ on Au(111) with intended 1 to 1 precursor ratio.

Element	**Ratio Relative to Sn Before**	**Ratio Relative to Sn After**
Sn $3d_{5/2}$	1	1
Cs $3d_{5/2}$	1.17	0.56
Br $3d_{5/2}$	2.47	1.72

Table 8.12: Ratios of elements relative to Sn before and after air exposure from $CsSnBr_3$ on Au(111) with intended 1 to 1 precursor ratio.

The fitting parameters for the elements before air exposure are listed in Table 8.9. The area of Cs $3d_{5/2}$ is 2660896.6 with a FWHM of 1.57 eV and a position of 724.98 eV. The fitting parameters after air exposure are provided in Table 8.10. The Cs $3d_{5/2}$ peak shifts to 724.61 eV with a decreased area of 1241526.4, representing a decrease of approximately 53.4%.

The energy differences before and after air exposure for various elements are listed in Table 8.11. For example, the energy difference for Cs $3d_{5/2}$ is 0.37 eV.

The ratios of elements relative to Sn before and after air exposure are presented in Table 8.12. Notably, the ratio of Cs relative to Sn decreases from 1.17 to 0.56 after air exposure, indicating significant changes in the sample composition.

8.2.3 $CsSnBr_3$ on Au(111) with excess of CsBr

Building upon previous results using a 1:1 ratio of $SnBr_2$ and CsBr precursors, this experiment aimed to investigate the effects of increasing the CsBr content in the deposited ultrathin film. The deposition process involved co-depositing CsBr at 428°C (increased by 5°C) and $SnBr_2$ at 170°C onto Au(111) for 10 minutes at room temperature, with an intentionally increased flux from the CsBr crucible to favor more CsBr incorporation into the film. By adjusting the precursor ratio in this way, we sought to explore how the increased CsBr content influences the film's properties.

Figure 8.8 shows the XPS spectra of Sn 3d core levels on $CsSnBr_3$ on Au(111) with excess CsBr before and after air exposure. The XPS data for the other elements are shown in Figure 8.9.

For $CsSnBr_3$ samples prepared with excess CsBr on Au(111), XPS data of the Sn 3d core levels were recorded before and after air exposure. This time, one pair is at the positions of 494.91 eV and 486.50 eV, corresponding to the Sn^{2+} state of Sn $3d_{3/2}$ and Sn $3d_{5/2}$, respectively. Another set of peaks at slightly lower binding energies of 493.99 eV and 485.58 eV is associated with metallic tin (Sn^0).

After air exposure, new peaks appeared, as expected, at higher binding energies (495.75 eV and 487.34 eV), attributed to the Sn^{4+} state. The Sn^{4+} peak became dominant, while the Sn^0 state disappeared, showing that Sn^{2+} converted to Sn^{4+} and Sn^0 converted to Sn^{2+} and Sn^{4+} similar to the previous samples.

The analysis of the oxygen O 1s peak after air exposure revealed three peaks at 530.78 eV, 532.06 eV, and 533.29 eV, corresponding to oxygen in SnO_2 (pristine), SnO_2 (oxygen-deficient regions), and adsorbed oxygen species, respectively [97]. Only in this sample, SnO_2 (oxygen-deficient regions) shows the highest amount with respect to the other oxygen peaks among the other samples. For Cs and Br, the XPS data showed peaks at 738.92 eV and 724.98 eV for Cs $3d_{3/2}$ and Cs $3d_{5/2}$, and at 69.79 eV and 68.74 eV for Br $3d_{3/2}$ and Br $3d_{5/2}$. After air exposure, the Cs peaks shifted slightly by 0.03 eV to lower binding energies, while additional peaks for Br appeared at 0.18 eV higher binding energy.

Similar to the previous observation, before air exposure, the elemental ratios of $CsSnBr_3$ deviated from the expected stoichiometry (see Table 8.16). Post-exposure, Cs and Br levels relative to Sn dropped considerably, hinting at potential diffusion or evaporation. The decline in Cs and Br, coupled with a rise in Sn intensity, implies that Br may form Br_2 gas and desorb, while Cs might diffuse to the adlayer-gold interface. The more substantial decrease in Cs suggests possible metallic Cs evaporation. The reduced Au intensity, suggesting an oxide layer, further supports this hypothesis.

The fitting parameters for the elements before air exposure are listed in Table 8.13. For example, the area of Cs $3d_{5/2}$ is 2660896.6 with a FWHM of 1.57 eV and a position of 724.98 eV. The fitting parameters after air exposure are provided in Table 8.14. The Cs $3d_{5/2}$ peak shifts to 724.95 eV with a decreased area of 1550382.04, representing a decrease of approximately 41.7%.

The energy differences before and after air exposure for various elements are listed in Table 8.15. For example, the energy difference for Cs $3d_{5/2}$ is 0.03 eV.

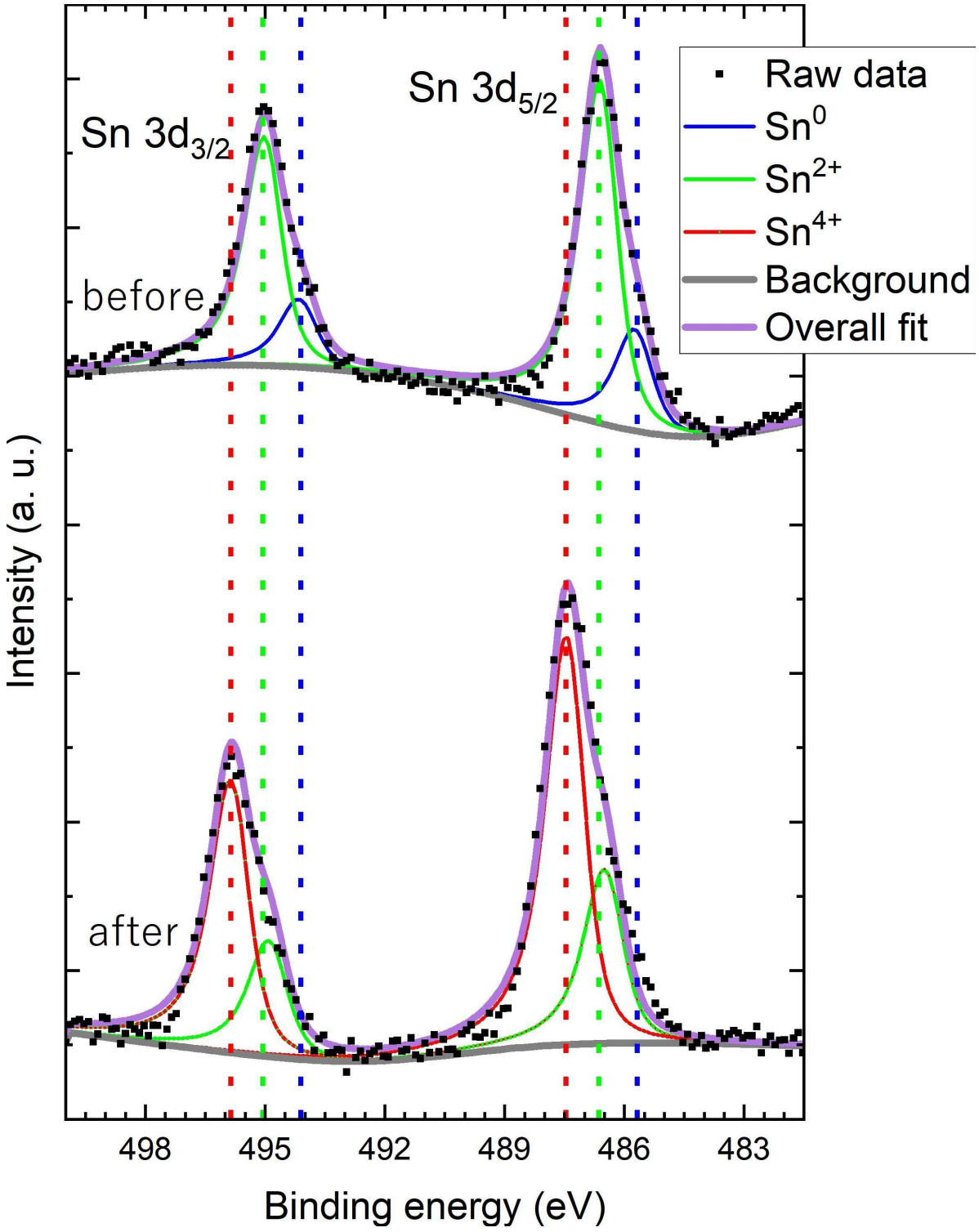


Figure 8.8: XPS spectra of Sn 3d core levels on $CsSnBr_3$ on Au(111) with excess of CsBr before and after air exposure. Spectrum before has been shifted up for clarity. Black dots represent data points and full lines are the respective fits.

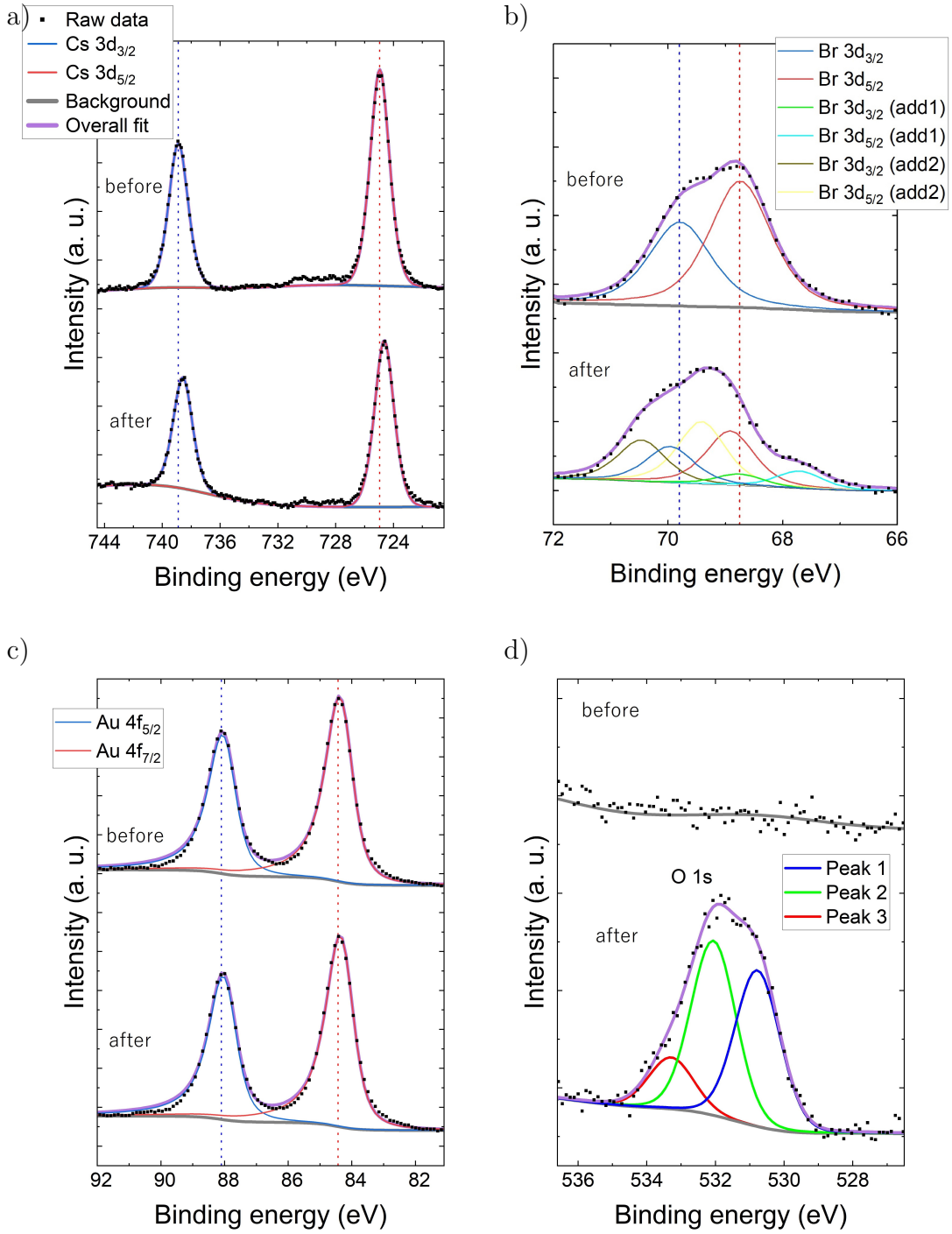


Figure 8.9: XPS data of elements on $CsSnBr_3$ with excess CsBr on Au(111). (a) Cs 3d spectrum with Cs $3d_{3/2}$ and Cs $3d_{5/2}$ peaks. Raw data (black dots), individual fits (blue and red lines), background (gray line), overall fit (purple). (b) Br 3d spectrum with Br $3d_{3/2}$ and Br $3d_{5/2}$ peaks, and additional components (cyan, red, green, blue, brown, yellow lines). (c) Au 4f spectrum with Au $4f_{5/2}$ and Au $4f_{7/2}$ peaks. Individual fits (blue and red lines). (d) O 1s spectrum showing three peaks.

Element	Area	FWHM (eV)	Position (eV)
Au $4f_{5/2}$	2613418	0.96	87.95
Au $4f_{7/2}$	3484557.4	0.96	84.28
Br $3d_{3/2}$	208079.79	1.28	69.79
Br $3d_{5/2}$	312119.53	1.28	68.74
Cs $3d_{3/2}$	1773931.9	1.57	738.92
Cs $3d_{5/2}$	2660896.6	1.57	724.98
Sn^0 $3d_{3/2}$	148962.2	1.1	493.99
Sn^0 $3d_{5/2}$	223443.19	1.1	485.58
Sn^{2+} $3d_{3/2}$	529428.89	1.1	494.91
Sn^{2+} $3d_{5/2}$	794142.94	1.1	486.5

Table 8.13: XPS data before air exposure $CsSnBr_3$ on Au(111) with excess of CsBr

Element	Area	FWHM (eV)	Position (eV)
Au $4f_{5/2}$	2720849.9	0.97	87.93
Au $4f_{7/2}$	3627799.9	0.97	84.26
Br $3d_{3/2}$ (add1)	79918.15	0.99	70.46
Br $3d_{5/2}$ (add1)	119877.16	0.99	69.41
Br $3d_{3/2}$	69673.35	0.99	69.97
Br $3d_{5/2}$	104509.97	0.99	68.92
Br $3d_{3/2}$ (add2)	22367.16	0.99	68.76
Br $3d_{5/2}$ (add2)	33550.72	0.99	67.71
Cs $3d_{3/2}$	1033588.54	1.57	738.89
Cs $3d_{5/2}$	1550382.04	1.57	724.95
O 1s (Peak 1)	137952.47	1.54	530.78
O 1s (Peak 2)	154174.21	1.54	532.06
O 1s (Peak 3)	45433.37	1.54	533.29
Sn^{2+} $3d_{3/2}$	261936.87	1.1	494.79
Sn^{2+} $3d_{5/2}$	392905.11	1.1	486.38
Sn^{4+} $3d_{3/2}$	614606.95	1.1	495.75
Sn^{4+} $3d_{5/2}$	921909.96	1.1	487.34

Table 8.14: XPS data after air exposure from on $CsSnBr_3$ with excess CsBr on Au(111).

Element	$E_{\textbf{before}} - E_{\textbf{after}}$ **(eV)**
Au $4f_{5/2}$	0.02
Au $4f_{7/2}$	0.02
Br $3d_{3/2}$	−0.18
Br $3d_{5/2}$	−0.18
Cs $3d_{3/2}$	0.03
Cs $3d_{5/2}$	0.03
Sn^{2+} $3d_{3/2}$	0.12
Sn^{2+} $3d_{5/2}$	0.12

Table 8.15: Energy differences before and after air exposure $CsSnBr_3$ on Au(111) with excess of CsBr.

Element	**Ratio Relative to Sn Before**	**Ratio Relative to Sn After**
Sn $3d_{5/2}$	1	1
Cs $3d_{5/2}$	1.66	0.75
Br $3d_{5/2}$	2.49	1.59

Table 8.16: Ratios of elements relative to Sn before and after air exposure on $CsSnBr_3$ with excess CsBr on Au(111).

The ratios of elements relative to Sn before and after air exposure are presented in Table 8.16. Notably, the ratio of Cs relative to Sn decreases from 1.66 to 0.75 after air exposure, indicating significant changes in the sample composition.

8.2.4 $CsSnBr_3$ on Au(111) with excess of $SnBr_2$

An ultrathin film was deposited via co-deposition of CsBr at 423°C and $SnBr_2$ at 175°C (increased by 5°C) onto Au(111) for 10 minutes at room temperature, resulting in an $SnBr_2$-rich film. Post-deposition LEED analysis showed faint middle spots. For $CsSnBr_3$ samples prepared with excess $SnBr_2$ on Au(111), XPS data of the Sn 3d core levels were recorded before and after air exposure. Figure 8.10 shows the XPS spectra for Sn 3d core levels, with the upper panel representing the pristine state and the lower panel showing the state after air exposure. In the pristine state, the spectra exhibited two pairs of peaks. One pair, located at 494.97 eV and 486.56 eV, corresponds to the Sn^{2+} state of Sn $3d_{3/2}$ and Sn $3d_{5/2}$, respectively. Another set of peaks at slightly lower binding energies, 493.98 eV and 485.57 eV, is attributed to metallic tin (Sn^0). The fitting parameters for the pristine state are listed in Table 8.17.

Upon air exposure, new peaks appeared at higher binding energies (495.82 eV and 487.41 eV), indicative of the Sn^{4+} state. As shown in Figure 8.10, the Sn^{4+} peak became predominant as in the previous cases, while the Sn^0 state vanished. This again indicates that Sn^{2+} was oxidized to Sn^{4+} and Sn^0 was converted to both Sn^{2+} and Sn^{4+}. The fitting parameters for the state after air exposure are detailed in Table 8.18.

The analysis of the oxygen O 1s peak after air exposure revealed three distinct peaks at 530.86 eV, 532.18 eV, and 533.18 eV (8.11), corresponding to oxygen in SnO_2 (pristine), SnO_2 (oxygen-deficient regions), and adsorbed oxygen species, respectively [97]. For Cs and Br, the XPS data showed peaks at 738.88 eV and 724.94 eV for Cs $3d_{3/2}$ and Cs $3d_{5/2}$, and at 69.78 eV and 68.73 eV for Br $3d_{3/2}$ and Br $3d_{5/2}$ before air exposure (Table 8.17), and additional peaks for Br at 70.51 eV and 69.46 eV after air exposure (Table 8.18). After air exposure, the Cs peaks shifted by 0.27 eV to lower binding energies, while additional peaks for Br appeared at 0.23 eV higher binding energy, as summarized in Table 8.20. These shifts suggest changes in the chemical environments of Cs and Br.

Initially, the elemental ratios of $CsSnBr_3$ followed the expected stoichiometry. However, after air exposure, the amounts of Cs and Br decreased significantly relative to Sn, indicating possible diffusion or evaporation. As detailed in Table 8.19, the reduction in Cs and Br content, along with an increase in overall Sn intensity, suggests that Br might form Br_2 gas and desorb, while Cs could diffuse to the interface of the adlayer with the gold surface. The more pronounced decrease in Cs compared to Br implies that metallic Cs might have evaporated. The observed decrease in Au intensity suggests the formation of an oxide layer on the top surface.

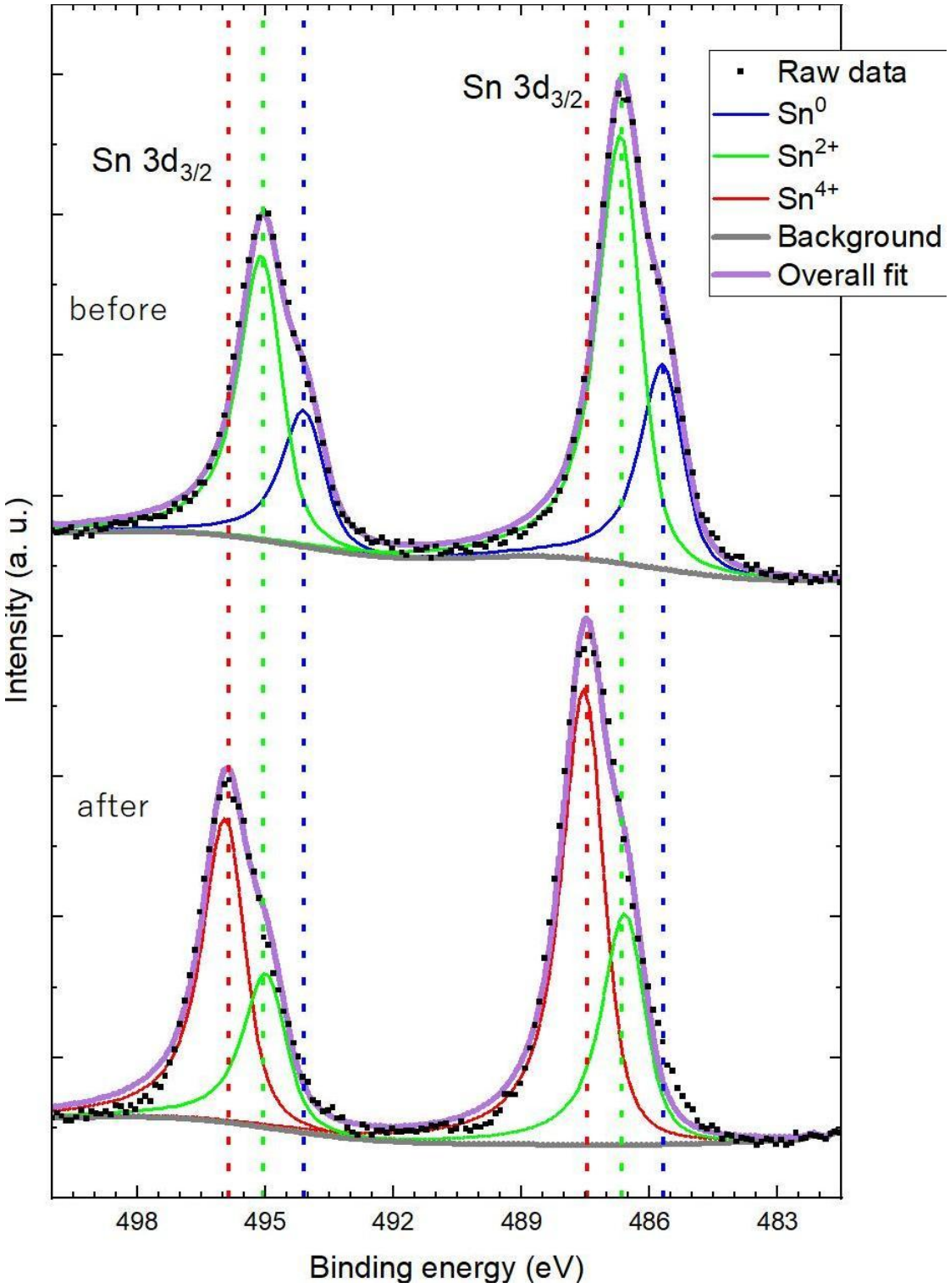


Figure 8.10: XPS data of Sn from $CsSnBr_3$ on Au(111) with $SnBr_2$ excess. Spectrum before has been shifted up for clarity. Black dots represent data points and full lines are the respective fits.

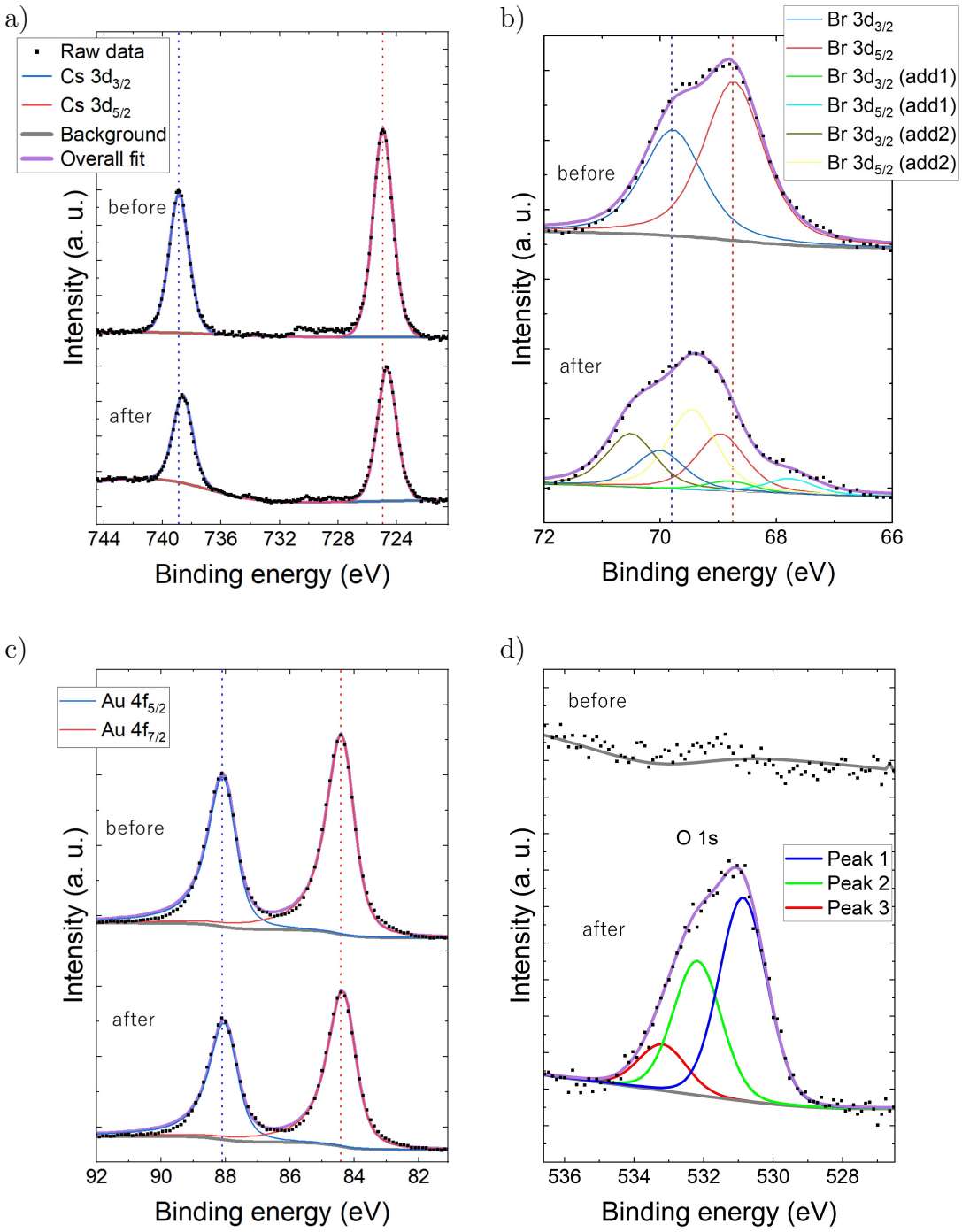


Figure 8.11: XPS data of elements on excess $SnBr_2$ $CsSnBr_3$ on Au(111). (a) Cs 3d spectrum with Cs $3d_{3/2}$ and Cs $3d_{5/2}$ peaks. Raw data (black dots), individual fits (blue and red lines), background (gray line), overall fit (purple). (b) Br 3d spectrum with Br $3d_{3/2}$ and Br $3d_{5/2}$ peaks, and additional components (cyan, red, green, blue, brown, yellow lines). (c) Au 4f spectrum with Au $4f_{5/2}$ and Au $4f_{7/2}$ peaks. Individual fits (blue and red lines). (d) O 1s spectrum showing three peaks.

Element	Area	FWHM (eV)	Position (eV)
Au $4f_{5/2}$	3112970.1	0.96	87.98
Au $4f_{7/2}$	4150626.8	0.96	84.3
Br $3d_{3/2}$	246186.79	1.22	69.78
Br $3d_{5/2}$	369280	1.22	68.73
Cs $3d_{3/2}$	1379827.9	1.57	738.88
Cs $3d_{5/2}$	2069740.8	1.57	724.94
Sn^0 $3d_{3/2}$	325739.73	1.1	493.98
Sn^0 $3d_{5/2}$	488609.35	1.1	485.57
Sn^{2+} $3d_{3/2}$	680459.46	1.1	494.97
Sn^{2+} $3d_{5/2}$	1020688.7	1.1	486.56

Table 8.17: XPS data before air exposure from $CsSnBr_3$ on Au(111) with $SnBr_2$ excess.

Element	Area	FWHM (eV)	Position (eV)
Au $4f_{5/2}$	2440226.6	0.96	87.94
Au $4f_{7/2}$	3253635.5	0.96	84.26
Br $3d_{3/2}$ (add1)	101839.92	0.99	70.51
Br $3d_{5/2}$ (add1)	152759.81	0.99	69.46
Br $3d_{3/2}$	72143.19	0.99	70.01
Br $3d_{5/2}$	108214.73	0.99	68.96
Br $3d_{3/2}$ (add2)	19130.83	0.99	68.80
Br $3d_{5/2}$ (add2)	28696.23	0.99	67.75
Cs $3d_{3/2}$	865490.15	1.55	738.61
Cs $3d_{5/2}$	1298234.6	1.55	724.67
O 1s (Peak 1)	201592.59	1.62	530.86
O 1s (Peak 2)	133086.78	1.62	532.18
O 1s (Peak 3)	45788.57	1.62	533.18
Sn^{2+} $3d_{3/2}$	369018.95	1.1	494.87
Sn^{2+} $3d_{5/2}$	553528.15	1.1	486.46
Sn^{4+} $3d_{3/2}$	725728.49	1.1	495.82
Sn^{4+} $3d_{5/2}$	1088592.2	1.1	487.41

Table 8.18: XPS data after air exposure from $CsSnBr_3$ on Au(111) with $SnBr_2$ excess.

Element	**Ratio Relative to Sn Before**	**Ratio Relative to Sn After**
Sn $3d_{5/2}$	1	1
Cs $3d_{5/2}$	0.87	0.65
Br $3d_{5/2}$	1.99	1.27

Table 8.19: Ratios of elements relative to Sn before and after air exposure from $CsSnBr_3$ on Au(111) with $SnBr_2$ excess.

Element	$E_{\mathbf{before}} - E_{\mathbf{after}}$ **(eV)**
Au $4f_{5/2}$	0.04
Au $4f_{7/2}$	0.04
Br $3d_{3/2}$	−0.23
Br $3d_{5/2}$	−0.23
Cs $3d_{3/2}$	0.27
Cs $3d_{5/2}$	0.27
Sn^{2+} $3d_{3/2}$	0.10
Sn^{2+} $3d_{5/2}$	0.10

Table 8.20: Energy differences before and after air exposure from $CsSnBr_3$ on Au(111) with $SnBr_2$ excess.

8.3 Summary of the XPS results

In this chapter, we explored the use of XPS to analyze precursor molecules in UHV and ultrathin tin halide perovskite films, both in their pristine forms and their degradation upon exposure to air.

Sample	**Br $3d_{5/2}$ (low)**	**Br $3d_{5/2}$ (mid)**	**Br $3d_{5/2}$ (high)**
CsBr on Au(111) (UHV)	67.14	68.57	
$SnBr_2$ on Au(111) (UHV)	67.06	68.49	
$CsSnBr_3$ on Au(100) (UHV)		68.76	
$CsSnBr_3$ on Au(100) (air)		68.68	69.34
$CsSnBr_3$ on Au(111) 1:1 (UHV)		68.74	
$CsSnBr_3$ on Au(111) 1:1 (air)	67.59	68.79	69.32
$CsSnBr_3$ on Au(111) CsBr (UHV)		68.74	
$CsSnBr_3$ on Au(111) CsBr (air)	67.71	68.92	69.41
$CsSnBr_3$ on Au(111) $SnBr_2$ (UHV)		68.73	
$CsSnBr_3$ on Au(111) $SnBr_2$ (air)	67.75	68.96	69.46

Table 8.21: Br $3d_{5/2}$ binding energies (eV) for all the samples.

Table 8.21 presents the Br $3d_{5/2}$ binding energies for $CsSnBr_3$ samples on Au substrates. The table helps in understanding the effects of air exposure and sample preparation considering the binding energies of bromine. The observed binding energies can be classified into three distinct ranges, each corresponding to different sample characteristics: Low binding energy values likely correspond to lower coverage on the Au surface, potentially due to partial dissociation of precursor atoms. This indicates a state where bromine atoms are not fully bound in the perovskite structure, which may result from free bromine on the surface. Mid binding energy values represent the desired perovskite structure, where Br atoms are bound within the $CsSnBr_3$ perovskite, indicating a successful formation of the perovskite phase. Samples that exhibit this energy range can be considered representative of the intended per-

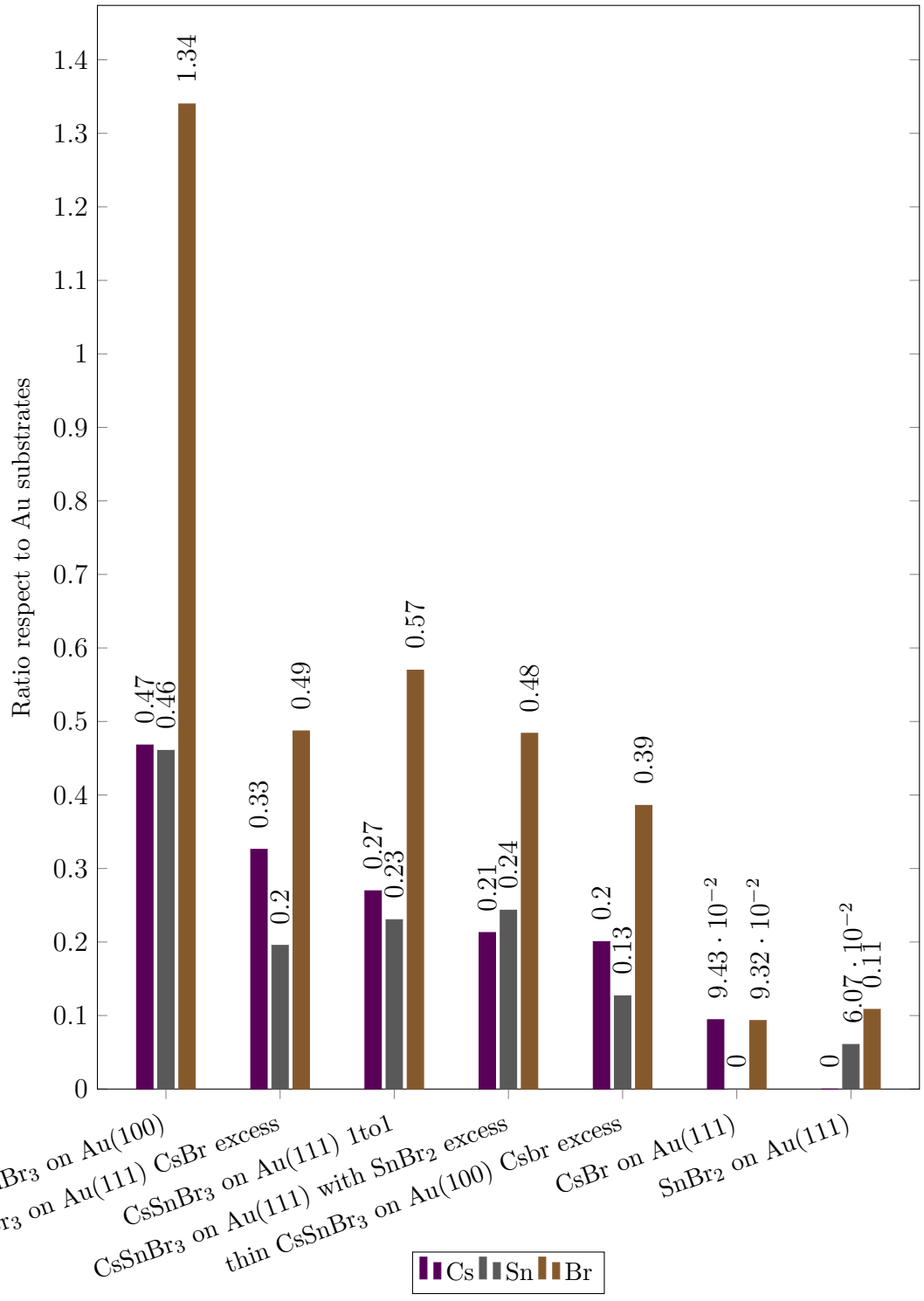


Figure 8.12: Bar chart showing the ratios of Cs, Sn, and Br with respect to Au for different depositions. The chart includes thin $CsSnBr_3$ on Au(100) with Csbr excess as well which is not mentioned in details but we put here for completeness.

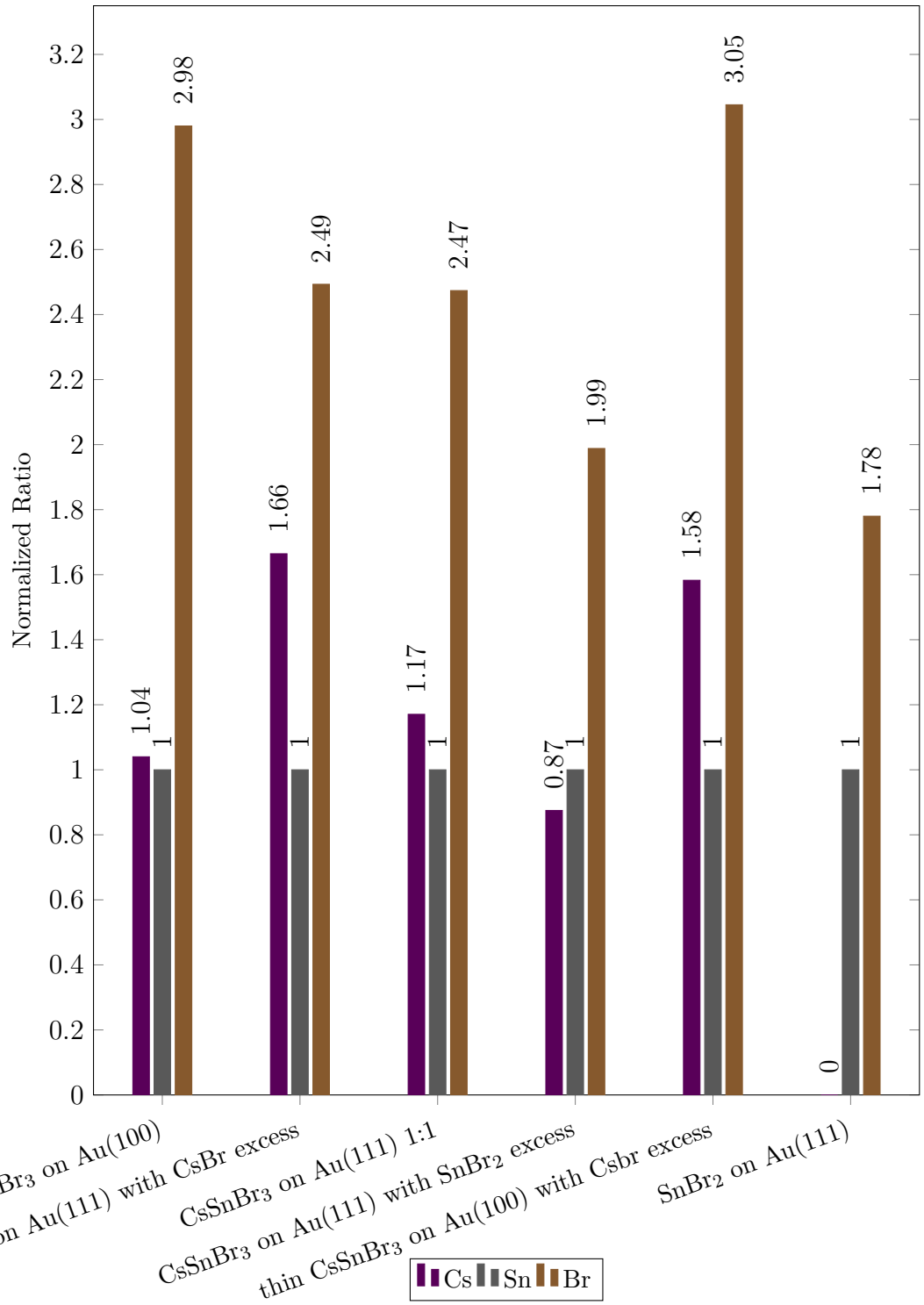


Figure 8.13: Bar chart showing the normalized ratios of Cs, Sn, and Br with respect to Sn for different depositions. The chart includes thin $CsSnBr_3$ on Au(100) with CsBr excess as well which is not mentioned in details but we put here for completeness.

ovskite material. High binding energy values appear after oxygen exposure, suggesting the degradation of the perovskite structure. This shift in binding energy is associated with the degradation products that form upon exposure to air, reflecting the instability of the perovskite when not kept in a UHV environment. By categorizing the binding energies in this way, Table 8.21 helps to interpret how variations in preparation and environmental exposure affect the stability and integrity of the bromine within $CsSnBr_3$ on Au substrates.

Figure 8.12 shows the bar chart of the ratios of Cs, Sn, and Br with respect to Au for different depositions. Notably, the $CsSnBr_3$ on Au(111) samples prepared with excess $SnBr_2$ exhibited lower ratios of Cs and Br compared to Sn, indicating also significant changes upon air exposure. The figure also helps to see the amounts of depositions comparably. The normalized ratios, as shown in Figure 8.13, further highlight the variations in elemental composition relative to Sn.

Table 8.22 presents the Cs $3d_{5/2}$ and $3d_{3/2}$ binding energies for samples on Au(111) and Au(100) before and after air exposure, highlighting slight shifts in the range of the measurement error. Additionally, the Au $4f_{7/2}$ and $4f_{5/2}$ binding energies are summarized in Table 8.23, where consistent values are observed across different samples, indicating almost the same interactions between the deposited compounds and the Au substrate. Finally, Table 8.24 provides the O 1s binding energies detected in samples after air exposure, showing distinct peaks that suggest the formation of oxygen-containing species on the surface. These tables collectively illustrate how binding energies vary with sample composition and environmental exposure, which is crucial for understanding the stability and reactivity of these materials.

Sample	**Cs $3d_{5/2}$ (eV)**	**Cs $3d_{3/2}$ (eV)**
CsBr on Au(111)	724.42	738.37
$CsSnBr_3$ on Au(100) (before air)	724.95	738.89
$CsSnBr_3$ on Au(100) (after air)	724.74	738.68
$CsSnBr_3$ on Au(111) 1:1 ratio (before air)	724.98	738.92
$CsSnBr_3$ on Au(111) 1:1 ratio (after air)	724.61	738.55
$CsSnBr_3$ on Au(111) CsBr excess (before air)	724.98	738.92
$CsSnBr_3$ on Au(111) CsBr excess (after air)	724.95	738.89
$CsSnBr_3$ on Au(111) $SnBr_2$ excess (before air)	724.94	738.88
$CsSnBr_3$ on Au(111) $SnBr_2$ excess (after air)	724.67	738.61

Table 8.22: Cs binding energies (eV) for $3d_{5/2}$ and $3d_{3/2}$ states in different samples.

For precursor molecules, XPS measurements of CsBr on Au(111) reveal distinct peaks for Cs 3d and Br 3d orbitals, with the Br 3d spectrum exhibiting additional peaks, potentially suggesting a different chemical state or surface species (Figure 8.1). The elemental ratio of Cs to Br is approximately 1:0.98, close to the expected 1:1 stoichiometry for CsBr (Table 8.2). For SnBr(2) on Au(111), XPS data show peaks for Sn 3d and Br 3d orbitals, with additional Br 3d peaks indicating different chemical states (Figure 8.2). The elemental ratio of Br to Sn is approximately 1.78:1 (Table 8.4) which indicated the dissociation of $SnBr_2$.

Sample	**Au** $4f_{7/2}$ **(eV)**	**Au** $4f_{5/2}$ **(eV)**
CsBr on Au(111)	84.23	87.91
$SnBr_2$ on Au(111)	84.28	87.96
$CsSnBr_3$ on Au(100) (before air)	84.31	87.96
$CsSnBr_3$ on Au(100) (after air)	84.25	87.93
$CsSnBr_3$ on Au(111) 1:1 ratio (before air)	84.27	87.94
$CsSnBr_3$ on Au(111) 1:1 ratio (after air)	84.25	87.93
$CsSnBr_3$ on Au(111) CsBr excess (before air)	84.28	87.95
$CsSnBr_3$ on Au(111) CsBr excess (after air)	84.26	87.93
$CsSnBr_3$ on Au(111) $SnBr_2$ excess (before air)	84.30	87.98
$CsSnBr_3$ on Au(111) $SnBr_2$ excess (after air)	84.26	87.94

Table 8.23: Au binding energies (eV) for $4f_{7/2}$ and $4f_{5/2}$ states in different samples.

Sample	**O** $1s$ **(eV)**
$CsSnBr_3$ on Au(100) (after air)	530.91, 531.98, 532.91
$CsSnBr_3$ on Au(111) 1:1 ratio (after air)	530.79, 531.97, 532.97
$CsSnBr_3$ on Au(111) CsBr excess (after air)	530.78, 532.06, 533.29
$CsSnBr_3$ on Au(111) $SnBr_2$ excess (after air)	530.86, 532.18, 533.18

Table 8.24: O $1s$ binding energies (eV) in different samples after air exposure.

For perovskite samples, XPS analysis of $CsSnBr_3$ on Au(100) before and after air exposure (Figure 8.3) reveals changes in the chemical state of Sn. Initially, both Sn^{2+} and Sn^0 are observed, but after air exposure, Sn^{4+} becomes dominant, while Sn^0 disappears (Tables 8.5 and 8.6). The ratios of Cs and Br relative to Sn decrease significantly after air exposure, indicating a reduction in these elements (Table 8.8). Similar observations were made for $CsSnBr_3$ on Au(111) with excess CsBr and excess $SnBr_2$ (Figures 8.6 and 8.10), with the Sn^{4+} state dominating after air exposure (Tables 8.14 and 8.18). The elemental ratios of Cs and Br to Sn decreased after air exposure, suggesting changes in sample composition due to oxidation and diffusion/evaporation (Tables 8.12 and 8.19).

In summary, XPS analysis provided detailed insights into the chemical states and stability of tin halide perovskites and precursor molecules, highlighting the effects of air exposure and the benefits of UHV preparation in stabilizing desired oxidation states.

Chapter 9

Conclusion and outlook

This thesis has explored the synthesis, characterization, and stability of ultrathin films of $CsSnBr_3$ perovskites on gold single crystals under ultra-high vacuum (UHV) conditions. The research aimed to address critical challenges in the field of perovskite solar cells, focusing on the need for lead-free alternatives and enhanced stability under environmental conditions.

The findings of this study contribute significantly to the growing body of knowledge on metal halide perovskites, particularly $CsSnBr_3$, by providing detailed insights into their atomic-scale structure, chemical composition, and degradation mechanisms. Through the use of advanced microscopy techniques such as scanning tunneling microscopy (STM) and low-energy electron diffraction (LEED), alongside chemical analysis using X-ray photoelectron spectroscopy (XPS), this research has elucidated the interactions between perovskite films and gold substrates, highlighting the influence of substrate symmetry on film formation and morphology.

Key achievements of this thesis include:

1. **Successful Synthesis and Characterization**: The study successfully synthesized $CsSnBr_3$ films on Au(111) and Au(100) substrates and characterized their structure and morphology at the atomic level. This detailed characterization revealed how substrate symmetry and deposition conditions affect the growth affect the growth and structure of the perovskite films. Further, the precursor molecules CsBr and $SnBr_2$ have been investigated on these gold surfaces.

2. **Degradation Mechanisms**: The research provided a comprehensive understanding of the chemical species formed during the degradation of $CsSnBr_3$ films upon exposure to air. This insight is crucial for developing strategies to enhance the stability of perovskite materials in practical applications.

3. **Lead-Free Alternatives**: By focusing on $CsSnBr_3$, a lead-free perovskite, this thesis addresses the environmental and health concerns associated with lead-based perovskites, contributing to the development of safer and more sustainable photovoltaic technologies.

The results of this study pave the way for further research into the optimization of perovskite materials for enhanced stability and performance. Future research directions include:

- **Encapsulation Techniques**: Developing effective encapsulation methods to protect perovskite films from environmental degradation without compromising their performance.
- **Compositional Engineering**: Exploring other lead-free perovskite compositions and their potential for high-efficiency solar cells.
- **Interface Modification**: Enhancing the stability and charge transport properties of perovskite solar cells through innovative interface engineering techniques.

In conclusion, this thesis provides a robust foundation for the continued advancement of perovskite solar cell technology, emphasizing the importance of material stability and environmental safety. The insights gained from this research will aid in the development of next-generation photovoltaic devices that are both efficient and sustainable.

Acknowledgements

Firstly, I would like to express my sincere gratitude to my group leader and referee, **Prof. Carsten Busse**, for his invaluable guidance and letting me conduct the research in his lab. His insights and expertise have been instrumental in shaping this work.

I am also deeply grateful to **Prof. Alex Redinger**, who is my second referee. I sincerely appreciate his valuable feedback and constructive discussions, as well as the opportunity to conduct experiments in his laboratory at the University of Luxembourg. His support has played an important role in strengthening the scientific aspects of this work.

I would like to extend my special appreciation to **Dr. Robin Ohmann**, to whom I owe all of my knowledge in STM and also other UHV equipments. His patience, expertise, positive attitude and willingness to share his experience have been invaluable in shaping my practical skills and understanding of surface science techniques. Being the head of this unique project, his guidance and encouragement played huge role in this research.

A heartfelt thanks to **Dr. Jeremy Hieulle** for conducting the XPS measurements and for his valuable corrections and suggestions regarding the XPS section of my thesis. His input has greatly improved the quality and clarity of this part of my work.

I am also grateful to **Dr. Borna Pielić, Dina Wilks, and Dr. Thais Chagas** for taking the time to proofread my thesis. Their keen attention to detail and valuable suggestions have significantly improved the clarity and readability of this work.

Special thanks to **MNaF University of Siegen**, for providing access to the glovebox used for storing the precursors. Their support in maintaining a controlled environment for sample preparation has been essential for my experiments.

I also thank the **mechanical workshop and electrical workshop of the University of Siegen** for their technical assistance and support in designing and maintaining the equipment necessary for my research. Their expertise and dedication have been invaluable in ensuring smooth experimental operations.

I would also like to thank **Dennis Rybakowski** for his technical assistance and, especially, for organizing professional musical activities where we performed together. These moments provided a much-needed creative and social outlet alongside the research work.

I generally thank all my colleagues **Alice Bremerich, Kai Mehlich and Dr. Paulus Aleksa** for their collaboration all these years, engaging discussions, and the stimulating research environment that made my journey productive. Their help, whether through scientific discussions or technical, has made this journey smoother.

Finally, I am profoundly grateful to my family for their unwavering support, patience, and belief in me throughout this process.

This work would not have been possible without the contributions and support of all those mentioned, and I sincerely appreciate their role in this journey.

Bibliography

[1] M. Grätzel. Photoelectrochemical cells. *Nature*, 414(6861):338–344, 2001. DOI: https://doi.org/10.1038/35104607.

[2] J. Bisquert. *The Physics of Solar Cells: Perovskites, Organics, and Photovoltaic Fundamentals*. CRC Press, Boca Raton, FL, 2018. DOI: https://doi.org/10.1201/b22380.

[3] A. Kojima, K. Teshima, Y. Shirai, and T. Miyasaka. Organometal halide perovskites as visible-light sensitizers for photovoltaic cells. *Journal of the American Chemical Society*, 131(17):6050–6051, 2009. DOI: https://doi.org/10.1021/ja809598r.

[4] Wikipedia contributors. Perovskite. *Wikipedia: The Free Encyclopedia*, Wikimedia Foundation, Inc. https://en.wikipedia.org/wiki/Perovskite. Accessed on May 5, 2024.

[5] Wikipedia contributors. Calcium titanate perovskite structure. *Wikipedia: The Free Encyclopedia*. https://en.wikipedia.org/wiki/Calcium_titanate#/media/File:CaTiO3_perovskite_structure.png. Accessed on May 5, 2024.

[6] C. Eames, J. M. Frost, P. R. F. Barnes, B. C. O'Regan, A. Walsh, and M. S. Islam. Ionic transport in hybrid lead iodide perovskite solar cells. *Nature Communications*, 6:7497, 2015. DOI: https://doi.org/10.1038/ncomms8497.

[7] National Renewable Energy Laboratory (NREL). The promise of perovskite solar cells. n.d. https://www.nrel.gov/research/promise-perovskite-solar-cells.html. Accessed on May 22, 2024.

[8] L. Zhang, L. Mei, K. Wang, Y. Lv, S. Zhang, Y. Lian, X. Liu, Z. Ma, G. Xiao, Q. Liu, S. Zhai, S. Zhang, G. Liu, L. Yuan, B. Guo, Z. Chen, K. Wei, A. Liu, S. Yue, G. Niu, V. Pan, J. Sun, V. Hua, W.-Q. Wu, D. Di, B. Zhao, J. Tian, Z. Wang, Y. Yang, L. Chu, M. Yuan, H. Zeng, H.-L. Yip, K. Yan, W. Xu, L. Zhu, W. Zhang, G. Xing, F. Gao, and L. Ding. Advances in the application of perovskite materials. *Nano-Micro Letters*, 15:177, 2023. DOI: https://doi.org/10.1007/s40820-023-01140-3.

[9] M. C. Weidman, M. Seitz, S. D. Stranks, and W. A. Tisdale. Highly tunable colloidal perovskite nanoplatelets through variable cation, metal, and halide composition. *ACS Nano*, 10(8):7830–7839, 2016. DOI: https://doi.org/10.1021/acsnano.6b03496.

[10] X. Liu, M. Chen, Y. Zhang, J. Xia, J. Yin, M. Li, K. G. Brooks, R. Hu, X. Gao, Y.-H. Kim, A. Züttel, J. M. Luther, S. Kinge, Y. Feng, and M. K. Nazeeruddin. High-efficiency perovskite photovoltaic modules achieved via cesium doping. *Chemical Engineering Journal*, 431(Part 4):133713, 2022. DOI: https://doi.org/10.1016/j.cej.2021.133713.

[11] P. Čulík, K. Brooks, C. Momblona, M. Adams, S. Kinge, F. Maréchal, P. J. Dyson, and M. K. Nazeeruddin. Design and cost analysis of 100 MW perovskite solar panel manufacturing process in different locations. *ACS Energy Letters*, 7:3039–3044, 2022. DOI: https://doi.org/10.1021/acsenergylett.2c01728.

[12] Z. Liang, Y. Zhang, H. Xu, W. Chen, B. Liu, J. Zhang, H. Zhang, Z. Wang, D.-H. Kang, J. Zeng, X. Gao, Q. Wang, H. Hu, H. Zhou, X. Cai, X. Tian, P. Reiss, B. Xu, T. Kirchartz, Z. Xiao, S. Dai, N.-G. Park, J. Ye, and X. Pan. Homogenizing out-of-plane cation composition in perovskite solar cells. *Nature*, 624:557–563, 2023. DOI: https://doi.org/10.1038/s41586-023-06784-0.

[13] W. Shockley and H. J. Queisser. Detailed balance limit of efficiency of p-n junction solar cells. *Journal of Applied Physics*, 32(3):510–519, 1961. DOI: https://doi.org/10.1063/1.1736034.

[14] J. Li, H.-L. Cao, W.-B. Jiao, Q. Wang, M. Wei, I. Cantone, J. Lü, and A. Abate. Biological impact of lead from halide perovskites reveals the risk of introducing a safe threshold. *Nature Communications*, 11:310, 2020. DOI: https://doi.org/10.1038/s41467-019-14240-9.

[15] L. Wang, Q. Miao, D. Wang, M. Chen, H. Bi, J. Liu, A. K. Baranwal, G. Kapil, Y. Sanehira, T. Kitamura, T. Ma, Z. Zhang, Q. Shen, and S. Hayase. 14.31% power conversion efficiency of Sn-based perovskite solar cells via efficient reduction of Sn^{4+}. *Angewandte Chemie International Edition*, 62:e202307228, 2023. DOI: https://doi.org/10.1002/anie.202307228.

[16] M. M. Byranvand, W. Zuo, R. Imani, M. Pazoki, and M. Saliba. Tin-based halide perovskite materials: Properties and applications. *Chemical Science*, 13:6766–6795, 2022. DOI: https://doi.org/10.1039/d2sc02089g.

[17] H. Liu, Z. Zhang, W. Zuo, R. Roy, M. Li, M. M. Byranvand, and M. Saliba. Pure tin halide perovskite solar cells: Focusing on preparation and strategies. *Advanced Energy Materials*, 13:2202209, 2023. DOI: https://doi.org/10.1002/aenm.202202209.

[18] L. Lanzetta, T. Webb, N. Zibouche, X. Liang, D. Ding, G. Min, R. J. E. Westbrook, B. Gaggio, T. J. Macdonald, M. S. Islam, and S. A. Haque. Degradation mechanism of hybrid tin-based perovskite solar cells and the critical role of tin (IV) iodide. *Nature Communications*, 12:2853, 2021. DOI: https://doi.org/10.1038/s41467-021-23094-x.

[19] A. Singh, J. Hieulle, J. Ferreira Machado, S. Gharabeiki, W. Zuo, M. Uzair Farooq, H. Phirke, M. Saliba, and A. Redinger. Coevaporation stabilizes tin-based perovskites in a single Sn-oxidation state. *Nano Letters*, 22(17):7112–7118, 2022. DOI: https://doi.org/10.1021/acs.nanolett.2c02204.

[20] W. Liao, D. Zhao, Y. Yu, C. R. Grice, C. Wang, A. J. Cimaroli, P. Schulz, W. Meng, K. Zhu, R.-G. Xiong, and Y. Yan. Lead-free inverted planar formamidinium tin triiodide perovskite solar cells achieving power conversion efficiencies up to 6.22%. *Advanced Materials*, 28(42):9333–9340, 2016. DOI: https://doi.org/10.1002/adma.201602992.

[21] T.B. Song, T. Yokoyama, C. C. Stoumpos, J. Logsdon, D. H. Cao, M. R. Wasielewski, S. Aramaki, and M. G. Kanatzidis. Highly efficient planar perovskite solar cells through band alignment engineering. *Journal of the American Chemical Society*, 139:836–842, 2017. DOI: https://doi.org/10.1021/jacs.6b10734.

[22] G. A. Tosado, E. Zheng, and Q. Yu. Understanding the stability of perovskite solar cells and strategies for improvement. *Materials Advances*, 1:3507–3517, 2020. DOI: https://doi.org/10.1039/d0ma00584c.

[23] J. Hieulle, S. Luo, D.-Y. Son, A. Jamshaid, C. Stecker, Z. Liu, G. Na, D. Yang, R. Ohmann, L. K. Ono, L. Zhang, and Y. Qi. Imaging of the atomic structure of all-inorganic halide perovskites. *The Journal of Physical Chemistry Letters*, 11(3):818–823, 2020. DOI: https://doi.org/10.1021/acs.jpclett.9b03738.

[24] J. Yang, M. Meissner, T. Yamaguchi, B. Xi, K. Takahashi, S. A. A. Rahman, X. Liu, H. Yoshida, M. Fahlman, and S. Kera. Temperature-dependent band structure evolution determined by surface geometry in organic halide perovskite single crystals. *Physical Review B*, 102:245101, 2020. DOI: https://doi.org/10.1103/PhysRevB.102.245101.

[25] A. Jamshaid, Z. Guo, J. Hieulle, C. Stecker, R. Ohmann, L. K. Ono, L. Qiu, G. Tong, W. Yin, and Y. B. Qi. Atomic-scale insight into the enhanced surface stability of methylammonium lead iodide perovskite by controlled deposition of lead chloride. *Energy & Environmental Science*, 14:4541–4554, 2021. DOI: https://doi.org/10.1039/d1ee01387e.

[26] A. F. Akbulatov, S. A. Tsarev, M. Elshobaki, S. Y. Luchkin, I. S. Zhidkov, E. Z. Karmaev, S. M. Aldoshin, K. J. Stevenson, and P. A. Troshin. Comparative intrinsic thermal and photochemical stability of Sn(II) complex halides as next-generation materials for lead-free perovskite solar cells. *The Journal of Physical Chemistry C*, 123(44):26862–26869, 2019. DOI: https://doi.org/10.1021/acs.jpcc.9b07930.

[27] A. Jain, S. P. Ong, G. Hautier, W. Chen, W. D. Richards, S. Dacek, S. Cholia, D. Gunter, D. Skinner, G. Ceder, and K. A. Persson. Commentary: The Materials Project: A materials genome approach to accelerating materials innovation. *APL Materials*, 1(1):011002, 2013. DOI: https://doi.org/10.1063/1.4812323.

[28] J. Hieulle, X. Wang, C. Stecker, D.-Y. Son, L. Qiu, R. Ohmann, Z. Liu, L. K. Ono, L. Zhang, and Y. Qi. Unraveling the impact of halide mixing on perovskite stability. *Journal of the American Chemical Society*, 141:3515–3523, 2019. DOI: https://doi.org/10.1021/jacs.8b11210.

[29] S. Bonomia, M. Patrinib, G. Bongiovanni, and L. Malavasi. Versatile vapor phase deposition approach to cesium tin bromide materials $CsSnBr_3$, $CsSn_2Br_5$ and Cs_2SnBr_6. *RSC Advances*, 10:28478–28482, 2020. DOI: https://doi.org/10.1039/d0ra05551d.

[30] D. E. Scaife, P. F. Weller, and W. G. Fisher. Crystal preparation and properties of cesium tin(II) trihalides. *Journal of Solid State Chemistry*, 9(3):308–314, 1974. DOI: https://doi.org/10.1016/0022-4596(74)90089-9.

[31] M. Mori and H. Saito. An X-ray study of successive phase transitions in $CsSnBr_3$. *Journal of Physics C: Solid State Physics*, 19:2391–2399, 1986. DOI: https://doi.org/10.1088/0022-3719/19/14/012.

[32] B. Li, R. Long, Y. Xia, and Q. Mi. All-inorganic perovskite CsSnBr3 as a thermally stable, free-carrier semiconductor. *Angewandte Chemie International Edition*, 57:13154–13158, 2018. DOI: https://doi.org/10.1002/anie.201807079.

[33] S. Gupta, T. Bendikov, G. Hodes, and D. Cahen. CsSnBr3, a lead-free halide perovskite for long-term solar cell application: Insights on SnF2 addition. *ACS Energy Letters*, 1:1028–1033, 2016. DOI: https://doi.org/10.1021/acsenergylett.6b00401.

[34] J. P. Correa-Baena, M. Saliba, T. Buonassisi, M. Grätzel, A. Abate, W. Tress, and A. Hagfeldt. Promises and challenges of perovskite solar cells. *Science*, 358(6364):739–744, 2017. DOI: https://doi.org/10.1126/science.aam6323.

[35] C. J. Chen. *Physics of Solar Energy*. John Wiley & Sons, Inc., 2011. DOI: https://doi.org/10.1002/9781118172841.

[36] L. Duan, S. P. Phang, D. Yan, J. Stuckelberger, D. Walter, Y. Hou, W. Wang, N. Chang, A. D. Bui, A. O. Mayon, L. Chang, D. Kang, T. Duong, R. Basnet, H. Nguyen, T. White, J. Bullock, K. Weber, D. MacDonald, K. Catchpole, and H. Shen. Over 29%-efficient, stable n-i-p monolithic perovskite/silicon tandem solar cells based on double-sided poly-Si/SiO_2 passivating contact silicon cells. *Journal of Materials Chemistry A*, 12:20006–20016, 2024. DOI: https://doi.org/10.1039/D4TA03396E.

[37] G. Binnig and H. Rohrer. Scanning tunneling microscopy—from birth to adolescence. *Reviews of Modern Physics*, 59(3):615–625, 1987. DOI: https://doi.org/10.1103/RevModPhys.59.615.

[38] NobelPrize.org. The Nobel Prize in Physics 1986. Nobel Prize Outreach AB 2023. https://www.nobelprize.org/prizes/physics/1986/summary/. Accessed on May 5, 2024.

[39] S. Lounis. Theory of scanning tunneling microscopy. *arXiv preprint arXiv:1404.0961*, 2014. https://arxiv.org/abs/1404.0961.

[40] C. J. Chen. *Introduction to Scanning Tunneling Microscopy*. Oxford University Press, 2008.

[41] R. Wiesendanger. *Scanning Probe Microscopy and Spectroscopy: Methods and Applications*. Cambridge University Press, 1994.

[42] J. Bardeen, L. N. Cooper, and J. R. Schrieffer. Theory of superconductivity. *Physical Review*, 108:1175–1204, 1957. DOI: https://doi.org/10.1103/PhysRev.108.1175.

[43] K. Oura, V. G. Lifshits, and A. A. Saranin. *Surface Science - An Introduction*. Springer, 2003.

[44] D. P. Woodruff and T. A. Delchar. *Modern Techniques of Surface Science*. Cambridge University Press, 2005. DOI: https://doi.org/10.1002/bbpc.19890930129.

[45] Wikipedia contributors. Schematic of a rear-view LEED instrument. *Wikipedia: The Free Encyclopedia*, Wikimedia Foundation, Inc. https://en.wikipedia.org/wiki/Low-energy_electron_diffraction#/media/File:Low-energy_electron_diffraction_(LEED)_instrument_-_schematic_diagram.svg.

[46] A. Einstein. Über einen die Erzeugung und Verwandlung des Lichtes betreffenden heuristischen Gesichtspunkt. *Annalen der Physik*, 322(6):132–148, 1905. DOI: https://doi.org/10.1002/andp.19053220607.

[47] R. Gross and A. Marx. *Festkörperphysik*. De Gruyter, Berlin, Boston, 2018. DOI: https://doi.org/10.1515/9783110559187.

[48] J.-Q. Zhong, M. Wang, W. H. Hoffmann, M. A. van Spronsen, D. Lu, and J. A. Boscoboinik. Synchrotron-based ambient pressure X-ray photoelectron spectroscopy of hydrogen and helium. *Applied Physics Letters*, 112(9):091602, 2018. DOI: https://doi.org/10.1063/1.5022479.

[49] P. Hohenberg and W. Kohn. Inhomogeneous electron gas. *Physical Review*, 136:B864–B871, 1964. DOI: https://doi.org/10.1103/PhysRev.136.B864.

[50] W. Kohn and L. J. Sham. Self-consistent equations including exchange and correlation effects. *Physical Review*, 140:A1133–A1138, 1965. DOI: https://doi.org/10.1103/PhysRev.140.A1133.

[51] M. Born and J. R. Oppenheimer. Zur Quantentheorie der Molekeln. *Annalen der Physik*, 389(20):457–484, 1927. DOI: https://doi.org/10.1002/andp.19273892002.

[52] L. H. Thomas. The calculation of atomic fields. *Proceedings of the Cambridge Philosophical Society*, 23(5):542–548, 1927. DOI: https://doi.org/10.1017/S0305004100011683.

[53] E. Fermi. Eine statistische Methode zur Bestimmung einiger Eigenschaften des Atoms und ihre Anwendung auf die Theorie des periodischen Systems der Elemente. *Zeitschrift für Physik*, 48:73–79, 1928. DOI: https://doi.org/10.1007/BF01351576.

[54] J. P. Perdew, K. Burke, and M. Ernzerhof. Generalized gradient approximation made simple. *Physical Review Letters*, 77:3865–3868, 1996. DOI: https://doi.org/10.1103/PhysRevLett.77.3865.

[55] A. D. Becke. Density-functional exchange-energy approximation with correct asymptotic behavior. *Physical Review A*, 38:3098–3100, 1988. DOI: https://doi.org/10.1103/PhysRevA.38.3098.

[56] M. A. L. Marques, N. T. Maitra, F. M. S. Nogueira, E. K. U. Gross, and A. Rubio, editors. *Fundamentals of Time-Dependent Density Functional Theory*, volume 837 of *Lecture Notes in Physics*. Springer, 2012. DOI: https://doi.org/10.1007/978-3-642-23518-4.

[57] A. Bremerich. *Heterojunctions of epitaxially grown transition metal dichalcogenides*. Master's thesis, University of Siegen, 2021.

[58] J. Schrage. *Test und Inbetriebnahme eines Ultrahochvakuumkoffers*. Bachelor's thesis, University of Siegen, 2020.

[59] N. Fairley, A. G. Shard, J. D. P. Counsell, I. R. Goulty, D. J. H. Cant, A. M. Ruenraroengsak, P. M. L. R. D. S. D. Jesus, C. A. Blomfield, V. Fernandez, D. O. Morgan, P. M. A. Sherwood, M. R. Linford, G. J. Leggett, D. R. Baer, and J. T. Grant. Systematic and collaborative approach to problem solving using X-ray photoelectron spectroscopy. *Applied Surface Science Advances*, 6:100112, 2021. DOI: https://doi.org/10.1016/j.apsadv.2021.100112.

[60] G. Ruano, E. Tosi, E. Sanchez, P. Abufager, M.L. Martiarena, O. Grizzi, and G. Zampieri. Stages of Se adsorption on Au(111): A combined XPS, LEED, TOF-DRS, and DFT study. *Surface Science*, 662:113–122, 2017. DOI: https://doi.org/10.1016/j.susc.2017.03.009.

[61] N. Haag, M. Laux, J. Stöckl, J. Kollamana, J. Seidel, N. Großmann, R. Fetzer, L. L. Kelly, Z. Wei, and B. Stadtmüller. Epitaxial growth of thermally stable cobalt films on Au(111). *New Journal of Physics*, 18:103054, 2016. DOI: https://doi.org/10.1088/1367-2630/18/10/103054.

[62] S. Bengió, V. Navarro, M. A. González-Barrio, R. Cortés, I. Vobornik, E. G. Michel, and A. Mascaraque. Electronic structure of reconstructed Au(100): Two-dimensional and one-dimensional surface states. *Physical Review B*, 86(4):045426, 2012. DOI: https://doi.org/10.1103/PhysRevB.86.045426.

[63] Kentax GmbH. *TCE-BSC Evaporator Manual*. https://www.kentax.de/kentax/Manual-evaporator.pdf.

[64] P. Li and F. Ding. Origin of the herringbone reconstruction of Au(111) surface at the atomic scale. *Science Advances*, 8(40):eabq2900, 2022. DOI: https://doi.org/10.1126/sciadv.abq2900.

[65] T. Giela, K. Freindl, N. Spiridis, and J. Korecki. Au(111) films on W(110) studied by STM and LEED – Uniaxial reconstruction, dislocations, and Ag nanostructures. *Applied Surface Science*, 312:91–96, 2014. DOI: https://doi.org/10.1016/j.apsusc.2014.04.115.

[66] C. S. Casari, S. Foglio, F. Siviero, A. Li Bassi, M. Passoni, and C. E. Bottani. Direct observation of the basic mechanisms of Pd island nucleation on Au(111). *Physical Review B*, 79:195402, 2009. DOI: https://doi.org/10.1103/PhysRevB.79.195402.

[67] L. G. Schulz. Polymorphism of cesium and thallium halides. *Acta Crystallographica*, 4:487–489, 1951. DOI: https://doi.org/10.1107/S0365110X51001641.

[68] S. Varshney and J. Nogami. Atomic structure of CsBr thin films on Ag (111). *Journal of Vacuum Science & Technology A*, 39(2):023203, 2021. DOI: https://doi.org/10.1116/6.0000808.

[69] T. Suzuki and R. Souda. Structure analysis of CsCl deposited on the MgO(001) surface by coaxial impact collision atom scattering spectroscopy (CAICASS). *Surface Science*, 442:283–290, 1999. DOI: https://doi.org/10.1016/S0039-6028(99)00935-8.

[70] G. Yoshikawa, M. Kiguchi, K. Ueno, A. Koma, and K. Saiki. Visible light photoemission and negative electron affinity of single-crystalline CsCl thin films. *Surface Science*, 544:220–226, 2003. DOI: https://doi.org/10.1016/j.susc.2003.08.016.

[71] W. Hebenstreit, J. Redinger, Z. Horozova, M. Schmid, R. Podloucky, and P. Varga. Atomic resolution by STM on ultra-thin films of alkali halides: Experiment and local density calculations. *Surface Science*, 424:L321–L328, 1999. DOI: https://doi.org/10.1016/S0039-6028(99)00095-3.

[72] J. Rieger. *Epitaktische anorganische Metallhalogenid-Perowskite auf Au(100)*. Dissertation, Friedrich Alexander University Erlangen-Nuremberg, 2022.

[73] Wikipedia contributors. Tin(II) bromide. *Wikipedia, The Free Encyclopedia*. https://en.wikipedia.org/wiki/Tin(II)_bromide. Last accessed November 28, 2024.

[74] J. L. Wardell. Tin: Inorganic chemistry. In R. Bruce King, editor, *Encyclopedia of Inorganic Chemistry*. John Wiley & Sons, 1994. ISBN 0-471-93620-0.

[75] K. Hilpert, M. Miller, and F. Ramondo. Thermochemistry of tetrabromoditin and bromoiodotin gaseous. *The Journal of Physical Chemistry*, 95:7261–7266, 1991. DOI: https://doi.org/10.1021/j100172a031.

[76] I. Abrahams and D. Z. Demetriou. Inert pair effects in tin and lead dihalides: Crystal structure of tin(II) bromide. *Journal of Solid State Chemistry*, 149:28–32, 2000. DOI: https://doi.org/10.1006/jssc.1999.8489.

[77] P. Eckold, W. Hügel, R. E. Dinnebier, and R. Niewa. Two modifications of tin(II) bromide. *Zeitschrift für anorganische und allgemeine Chemie*, 641(8-9):1467–1472, 2015. DOI: https://doi.org/10.1002/zaac.201500108.

[78] Y. Naik, D. Mehta, P. R. Parmar, P. H. Jariwala, and P. B. Thakor. Structural, electronic, and optical properties of $SnBr_2$ monolayer by density functional approach. *Materials Today: Proceedings*, 79(Part 2):617–621, 2023. DOI: https://doi.org/10.1016/j.matpr.2023.01.342.

[79] W. Gao, T. A. Baker, L. Zhou, D. S. Pinnaduwage, E. Kaxiras, and C. M. Friend. Chlorine adsorption on Au(111): Chlorine overlayer or surface chloride? *Journal of the American Chemical Society*, 130(11):3560–3565, 2008. DOI: https://doi.org/10.1021/ja077989a.

[80] Q.-Q. Yuan, F. Zheng, Z.-Q. Shi, Q.-Y. Li, Y.-Y. Lv, Y. Chen, P. Zhang, and S.-C. Li. Direct growth of van der Waals tin diiodide monolayers. *Advanced Science*, 8:2100009, 2021. DOI: https://doi.org/10.1002/advs.202100009.

[81] L. A. Meier, D. R. Salinas, J. M. Feliu, and S. G. García. Spontaneous deposition of Sn on Au(111). An in situ STM study. *Electrochemistry Communications*, 10:1583–1586, 2008. DOI: https://doi.org/10.1016/j.elecom.2008.08.013.

[82] E. R. Jette and F. Foote. Precision determination of lattice constants. *The Journal of Chemical Physics*, 3:605–616, 1935. DOI: https://doi.org/10.1063/1.1749562.

[83] A. R. Sandy, S. G. J. Mochrie, and D. M. Zehner. Structure and stability of the Au(111) surface: A synchrotron x-ray study. *Physical Review B*, 43(6):4667–4681, 1991. DOI: https://doi.org/10.1103/PhysRevB.43.4667.

[84] F. Ercolessi, E. Tosatti, and M. Parrinello. Au(100) surface reconstruction. *Physical Review Letters*, 57:719, 1986. DOI: https://doi.org/10.1103/PhysRevLett.57.719.

[85] K. Zhou, B. Qi, Z. Liu, X. Wang, Y. Sun, and L. Zhang. Advanced Organic–Inorganic Hybrid Materials for Optoelectronic Applications. *Advanced Functional Materials*, 2024. DOI: https://doi.org/10.1002/adfm.202411671.

[86] H. Zhou, Q. Chen, G. Li, S. Luo, T.-b. Song, H.-S. Duan, Z.-h. Hong, J.-b. You, Y. Liu, and Y. Yang. Interface engineering of highly efficient perovskite solar cells. *Science*, 345(6196):542–546, 2014. DOI: https://doi.org/10.1126/science.1254050.

[87] J. M. Ball and A. Petrozza. Defects in perovskite-halides and their effects in solar cells. *Nature Energy*, 1:16149, 2016. DOI: https://doi.org/10.1038/nenergy.2016.149.

[88] S. Bera, A. Saha, S. Mondal, A. Biswas, S. Mallick, R. Chatterjee, and S. Roy. Review of defect engineering in perovskites for photovoltaic application. *Materials Advances*, 3:5234–5269, 2022. DOI: https://doi.org/10.1039/d2ma00058f.

[89] R. Ohmann, L. K. Ono, H.-S. Kim, H. Lin, M. V. Lee, Y. Li, N.-G. Park, and Y. Qi. Real-space imaging of the atomic structure of organic-inorganic perovskite. *Journal of the American Chemical Society*, 137(48):16049–16054, 2015. DOI: https://doi.org/10.1021/jacs.5b08227.

[90] Y. Liu, K. Palotas, X. Yuan, T. Hou, H. Lin, Y. Li, and S.-T. Lee. Atomistic origins of surface defects in $CH_3NH_3PbBr_3$ perovskite and their electronic structures. *ACS Nano*, 11:2060–2065, 2017. DOI: https://doi.org/10.1021/acsnano.6b08260.

[91] L. She, Z. Shen, and D. Zhong. Surface structures of $CsSnI_3(001)$ films on Au(111). *The Journal of Physical Chemistry C*, 127:20101–20105, 2023. DOI: https://doi.org/10.1021/acs.jpcc.3c04884.

[92] J. Hieulle, D.-Y. Son, A. Jamshaid, X. Meng, C. Stecker, R. Ohmann, Z. Liu, L. K. Ono, and Y. B. Qi. Metal halide perovskites surfaces with mixed A-site cations: Atomic structure and device stability. *Advanced Functional Materials*, 33(9):2211097, 2023. DOI: https://doi.org/10.1002/adfm.202211097.

[93] Y. Jiang, X. Liang, S. Ren, C.-L. Chen, L.-J. Fan, Y.-W. Yang, J.-M. Tang, and D.-A. Luh. The growth of sulfur adlayers on Au(100). *The Journal of Chemical Physics*, 142(6):064708, 2015. DOI: https://doi.org/10.1063/1.4907789.

[94] CasaXPS. Line shapes. In *CasaXPS Manual*. Available at http://www.casaxps.com/help_manual/line_shapes.htm.

[95] J. F. Moulder, W. F. Stickle, P. E. Sobol, and K. D. Bomben. *Handbook of X-ray Photoelectron Spectroscopy*. Perkin-Elmer Corp, Eden Prairie, MN, 1992. Available at https://www.hic.ch.ntu.edu.tw/PES/file/%E5%8F%83%E8%80%83%E8%B3%87%E6%96%99/XPS%20handbook.pdf.

[96] J. H. Scofield. Hartree-Slater subshell photoionization cross-sections at 1254 and 1487 eV. *Journal of Electron Spectroscopy and Related Phenomena*, 8(2):129–137, 1976. DOI: https://doi.org/10.1016/0368-2048(76)80015-1.

[97] P. G. Choi, N. Izu, N. Shirahata, and Y. Masuda. SnO2 nanosheets for selective alkene gas sensing. *ACS Applied Nano Materials*, 2:1820–1827, 2019. DOI: https://doi.org/10.1021/acsanm.8b01945.

[98] R. C. E. Hamlyn, M. Mahapatra, I. Orozco, I. Waluyo, A. Hunt, J. A. Rodriguez, M. G. White, and S. D. Senanayake. Structure and chemical state of cesium on well-defined Cu(111) and Cu_2O/Cu(111) surfaces. *The Journal of Physical Chemistry C*, 124(3):1997–2007, 2020. DOI: https://doi.org/10.1021/acs.jpcc.9b10608.

[99] A. R. Kirmani, A. E. Mansour, C. Yang, R. Munir, A. M. El-Zohry, O. F. Mohammed, and A. Amassian. Facile and noninvasive passivation, doping and chemical tuning of macroscopic hybrid perovskite crystals. *PLoS ONE*, 15(3):e0230540, 2020. DOI: https://doi.org/10.1371/journal.pone.0230540.

[100] M. Bick and H. C. Prinz. Cesium and cesium compounds. In *Ullmann's Encyclopedia of Industrial Chemistry*. Wiley-VCH, Weinheim, 2005. DOI: https://doi.org/10.1002/14356007.a06_153.pub2.

[101] D. Fröhlich, R. Kenklies, and R. Helbig. Band-gap assignment in SnO_2 by two-photon spectroscopy. *Physical Review Letters*, 41(25):1750–1751, 1978. DOI: https://doi.org/10.1103/PhysRevLett.41.1750.

[102] A. Schleife, J. B. Varley, F. Fuchs, C. Rödl, F. Bechstedt, P. Rinke, A. Janotti, and C. G. Van de Walle. Tin dioxide from first principles: Quasiparticle electronic states and optical properties. *Physical Review B*, 83:035116, 2011. DOI: https://doi.org/10.1103/PhysRevB.83.035116.

[103] X. Cai, P. Zhang, and S.-H. Wei. Revisit of the band gaps of rutile SnO_2 and TiO_2: A first-principles study. *Journal of Semiconductors*, 40(9):092101, 2019. DOI: https://doi.org/10.1088/1674-4926/40/9/092101.

[104] J.-W. Lee, S.-H. Bae, N. De Marco, Y.-T. Hsieh, Z. Dai, and Y. Yang. The role of grain boundaries in perovskite solar cells. *Materials Today Energy*, 7:149–160, 2018. DOI: https://doi.org/10.1016/j.mtener.2017.07.014.

[105] J. Zhang, S. Tang, M. Zhu, Z. Li, Z. Cheng, S. Xiang, and Z. Zhang. The role of grain boundaries in organic–inorganic hybrid perovskite solar cells and its current enhancement strategies: A review. *Energy and Environmental Materials*, 7(2):e12696, 2024. DOI: https://doi.org/10.1002/eem2.12696. (Updated volume/issue)

[106] C. Davisson and L. H. Germer. Diffraction of electrons by a crystal of nickel. *Physical Review*, 30:705–740, 1927. DOI: https://doi.org/10.1103/PhysRev.30.705.

[107] W. Zhang, L. K. Ono, J. Xue, and Y. Qi. Atomic Level Insights into Metal Halide Perovskite Materials by Scanning Tunneling Microscopy and Spectroscopy. *Angewandte Chemie International Edition*, 2021. DOI: https://doi.org/10.1002/anie.202112352.

[108] G. Kresse and D. Joubert. From ultrasoft pseudopotentials to the projector augmented-wave method. *Physical Review B*, 59:1758–1775, 1999. DOI: https://doi.org/10.1103/PhysRevB.59.1758.

[109] J. Rieger, T. Kißlinger, A. Raabgrund, J. Hauner, D. Niesner, M. A. Schneider, and T. Fauster. Epitaxial inorganic metal-halide perovskite films with controlled surface terminations. *Physical Review Materials*, 7:035403, 2023. DOI: https://doi.org/10.1103/PhysRevMaterials.7.035403.

[110] T. Fauster, L. Hammer, K. Heinz, and M. A. Schneider. *Surface Physics: Fundamentals and Methods*. De Gruyter Oldenbourg, Berlin, Boston, 2020. DOI: https://doi.org/10.1515/9783110636697.

[111] R. Avci and C. P. Flynn. Charge transfer and percolation in alkali-metal alloys. *Physical Review B*, 19(12):5967–5980, 1979. DOI: https://doi.org/10.1103/PhysRevB.19.5967.

[112] M. T. E. Halliday, A. G. Joly, W. P. Hess, and A. L. Shluger. Photoinduced Br desorption from CsBr thin films grown on Cu(100). *The Journal of Physical Chemistry C*, 119(42):24036–24045, 2015. DOI: https://doi.org/10.1021/acs.jpcc.5b08275.

[113] J. P. Perdew, A. Ruzsinszky, G. I. Csonka, O. A. Vydrov, G. E. Scuseria, L. A. Constantin, X. Zhou, and K. Burke. Prescription for the design and selection of density functional approximations: More constraint satisfaction with fewer fits. *The Journal of Chemical Physics*, 123(6):062201, 2005. DOI: https://doi.org/10.1063/1.1904565.

[114] V. N. Staroverov, G. E. Scuseria, J. Tao, and J. P. Perdew. Comparing density functionals: Inflection points on the adiabatic connection. *Physical Review B*, 69:075102, 2004. DOI: https://doi.org/10.1103/PhysRevB.69.075102.

[115] C. Lee, W. Yang, and R. G. Parr. Development of the Colle-Salvetti correlation-energy formula into a functional of the electron density. *Physical Review B*, 37:785–789, 1988. DOI: https://doi.org/10.1103/PhysRevB.37.785.

[116] A. D. Becke. Density-functional thermochemistry. III. The role of exact exchange. *The Journal of Chemical Physics*, 98:5648–5652, 1993. DOI: https://doi.org/10.1063/1.464913.

[117] M. Abbasli, J. Hieulle, J. Schrage, D. Wilks, A. Samad, U. Schwingenschlögl, A. Redinger, C. Busse, and R. Ohmann. Tin halide perovskite epitaxial films on gold surfaces: Atomic structure and stability. *Advanced Functional Materials*, 2403680, First published May 6, 2024. DOI: https://doi.org/10.1002/adfm.202403680.

[118] S. Ghosal, J. C. Hemminger, H. Bluhm, B. S. Mun, E. L. D. Hebenstreit, G. Ketteler, D. F. Ogletree, F. G. Requejo, and M. Salmeron. Electron spectroscopy of aqueous solution interfaces reveals surface enhancement of halides. *Science*, 307(5709):563–566, 2005. DOI: https://doi.org/10.1126/science.1106525.

[119] A. J. Ramadan, M. Ralaiarisoa, F. Zu, L. A. Rochford, B. Wenger, N. Koch, and H. J. Snaith. Revealing the stoichiometric tolerance of lead trihalide perovskite thin films.

Chemistry of Materials, 32(1):114–120, 2020. DOI: https://doi.org/10.1021/acs.chemmater.9b02639.

[120] R. E. Watson, J. W. Davenport, M. L. Perlman, and T. K. Sham. Madelung effects at crystal surfaces: Implications for photoemission. *Physical Review B*, 24(4):1791–1797, 1981. DOI: https://doi.org/10.1103/PhysRevB.24.1791.

[121] P. S. Bagus, E. S. Ilton, and C. J. Nelin. The interpretation of XPS spectra: Insights into materials properties. *Surface Science Reports*, 68(2):273–304, 2013. DOI: https://doi.org/10.1016/j.surfrep.2013.03.001.

[122] T. C. Taucher, I. Hehn, O. T. Hofmann, M. Zharnikov, and E. Zojer. Understanding chemical versus electrostatic shifts in X-ray photoelectron spectra of organic self-assembled monolayers. *The Journal of Physical Chemistry C*, 120(6):3428–3437, 2016. DOI: https://doi.org/10.1021/acs.jpcc.5b11906.

[123] P. Docampo and T. Bein. A long-term view on perovskite optoelectronics. *Accounts of Chemical Research*, 49:339–346, 2016. DOI: https://doi.org/10.1021/acs.accounts.5b00465.

[124] M. Saliba, T. Matsui, J.-Y. Seo, K. Domanski, J.-P. Correa-Baena, M. K. Nazeeruddin, S. M. Zakeeruddin, W. Tress, A. Abate, A. Hagfeldt, and M. Grätzel. Cesium-containing triple cation perovskite solar cells: Improved stability, reproducibility and high efficiency. *Energy & Environmental Science*, 9:1989–1997, 2016. DOI: https://doi.org/10.1039/C5EE03874J.

[125] L. N. Quan, Y. Zhao, F. P. García de Arquer, R. Sabatini, G. Walters, O. Voznyy, R. Comin, Y. Li, J. Z. Fan, H. Tan, M. Yuan, O. M. Bakr, Z.-H. Lu, D. H. Kim, and E. H. Sargent. Tailoring the energy landscape in quasi-2D halide perovskites enables efficient green-light emission. *Nano Letters*, 17:3701–3709, 2017. DOI: https://doi.org/10.1021/acs.nanolett.7b00976.

[126] Z.-K. Tan, R. S. Moghaddam, M. L. Lai, P. Docampo, R. Higler, F. Deschler, M. Price, A. Sadhanala, L. M. Pazos, D. Credgington, F. Hanusch, T. Bein, H. J. Snaith, and R. H. Friend. Bright light-emitting diodes based on organometal halide perovskite. *Nature Nanotechnology*, 9:687–692, 2014. DOI: https://doi.org/10.1038/nnano.2014.149.

[127] Y. Ling, L. Tan, X. Wang, Y. Zhou, Y. Xin, B. Ma, T. Shi, Y. Li, and Z. Zou. Composite perovskites of cesium lead bromide for optimized photoluminescence. *The Journal of Physical Chemistry Letters*, 8:3266–3271, 2017. DOI: https://doi.org/10.1021/acs.jpclett.7b01302.

[128] Y. Ling, Y. Tian, X. Wang, J. C. Wang, J. M. Knox, F. Perez-Orive, Y. Du, L. Tan, K. Hanson, B. Ma, and H. Gao. Enhanced optical and electrical properties of polymer-assisted all-inorganic perovskites for light-emitting diodes. *Advanced Materials*, 28:8983–8989, 2016. DOI: https://doi.org/10.1002/adma.201602513.

[129] B. Saparov and D. B. Mitzi. Organic–inorganic perovskites: Structural versatility for functional materials design. *Chemical Reviews*, 116:4558–4596, 2016. DOI: https://doi.org/10.1021/acs.chemrev.5b00715.

[130] M. M. Muhammed and J. H. Mokkath. Electric field hotspots of all-inorganic off-stoichiometric $APbX_3$ (A = Cs, Rb and X = Cl, Br, I) perovskite quantum dots. *Physica E: Low-dimensional Systems and Nanostructures*, 113:65–71, 2019. DOI: https://doi.org/10.1016/j.physe.2019.04.027.

[131] J. Berry, T. Buonassisi, D. A. Egger, G. Hodes, L. Kronik, Y.-L. Loo, I. Lubomirsky, S. R. Marder, Y. Mastai, J. S. Miller, D. B. Mitzi, Y. Paz, A. M. Rappe, I. Riess, B. Rybtchinski, O. Stafsudd, V. Stevanovic, M. F. Toney, D. Zitoun, A. Kahn, D. Ginley, and D. Cahen. Hybrid organic–inorganic perovskites (HOIPs): Opportunities and challenges. *Advanced Materials*, 27:5102–5112, 2015. DOI: https://doi.org/10.1002/adma.201502294.

[132] H. Cho, S.-H. Jeong, M.-H. Park, Y.-H. Kim, C. Wolf, C.-L. Lee, J. H. Heo, A. Sadhanala, N. Myoung, S. Yoo, S. H. Im, R. H. Friend, and T.-W. Lee. Overcoming the electroluminescence efficiency limitations of perovskite light-emitting diodes. *Science*, 350:1222–1225, 2015. DOI: https://doi.org/10.1126/science.aad1818.

[133] M. Isarov, L. Z. Tan, M. I. Bodnarchuk, M. V. Kovalenko, A. M. Rappe, and E. Lifshitz. Rashba effect in a single colloidal $CsPbBr_3$ perovskite nanocrystal detected by magneto-optical measurements. *Nano Letters*, 17:5020–5026, 2017. DOI: https://doi.org/10.1021/acs.nanolett.7b02248.

[134] L. She, M. Liu, and D. Zhong. Atomic structures of $CH3NH3PbI_3$ (001) surfaces. *ACS Nano*, 10:1126–1131, 2016. DOI: https://doi.org/10.1021/acsnano.5b06420.

[135] D. Luo, Q. Chen, Y. Qiu, M. Zhang, and B. Liu. Device engineering for all-inorganic perovskite light-emitting diodes. *Nanomaterials*, 9(7):1007, 2019. DOI: https://doi.org/10.3390/nano9071007.

[136] M. Kepenekian, R. Robles, C. Katan, D. Sapori, L. Pedesseau, and J. Even. Rashba and Dresselhaus effects in hybrid organic–inorganic perovskites: From basics to devices. *ACS Nano*, 9:11557–11567, 2015. DOI: https://doi.org/10.1021/acsnano.5b04409.

[137] L. Protesescu, S. Yakunin, M. I. Bodnarchuk, F. Krieg, R. Caputo, C. H. Hendon, R. X. Yang, A. Walsh, and M. V. Kovalenko. Nanocrystals of cesium lead halide perovskites ($CsPbX_3$, X = Cl, Br, and I): Novel optoelectronic materials showing bright emission with wide color gamut. *Nano Letters*, 15:3692–3696, 2015. DOI: https://doi.org/10.1021/nl5048779.

[138] A. Perumal, S. Shendre, M. Li, Y. K. E. Tay, V. K. Sharma, S. Chen, Z. Wei, Q. Liu, Y. Gao, P. L. H. K. T. C. K. Sum, and H. V. Demir. High brightness formamidinium

lead bromide perovskite nanocrystal light emitting devices. *Scientific Reports*, 6:36733, 2016. DOI: https://doi.org/10.1038/srep36733.

[139] A. Swarnkar, A. R. Marshall, E. M. Sanehira, B. D. Chernomordik, D. T. Moore, J. A. Christians, T. Chakrabarti, and J. M. Luther. Quantum dot–induced phase stabilization of α-$CsPbI_3$ perovskite for high-efficiency photovoltaics. *Science*, 354:92–95, 2016. DOI: https://doi.org/10.1126/science.aag2700.

[140] R. Xiao, Y. Hou, Y. Fu, X. Peng, Q. Wang, E. Gonzalez, S. T. Omelchenko, B. M. Savoie, Y. Zhou, Y. Lin, G. C. Bazan, Z. L. Wang, W. A. Goddard III, M. A. Ratner, and Y. Yang. Photocurrent mapping in single-crystal methylammonium lead iodide perovskite nanostructures. *Nano Letters*, 16:7710–7717, 2016. DOI: https://doi.org/10.1021/acs.nanolett.6b03782.

[141] D. P. Woodruff. Low energy electron diffraction. In *Reference Module in Materials Science and Materials Engineering*. Elsevier, 2016. DOI: https://doi.org/10.1016/B978-0-12-803581-8.03400-7.

[142] L. El-Kareh, G. Bihlmayer, A. Buchter, H. Bentmann, S. Blügel, F. Reinert, D. Menzel, U. Heinzmann, M. Dähne, Z. S. Majzik, M. R. Rybkovskiy, A. M. Shikin, and A. Varykhalov. A combined experimental and theoretical study of Rashba-split surface states on the $(\sqrt{3}\times\sqrt{3})$ Pb/Ag(111)$R30°$ surface. *New Journal of Physics*, 16:045017, 2014. DOI: https://doi.org/10.1088/1367-2630/16/4/045017.

[143] L. Qian, Y. Zheng, J. Xue, and P. H. Holloway. Stable and efficient quantum-dot light-emitting diodes based on solution-processed multilayer structures. *Nature Photonics*, 5:543–548, 2011. DOI: https://doi.org/10.1038/nphoton.2011.171.

[144] R. E. Beal, D. J. Slotcavage, T. Leijtens, A. R. Bowring, R. A. Belisle, W. H. Nguyen, G. F. Burkhard, E. T. Hoke, and M. D. McGehee. Cesium lead halide perovskites with improved stability for tandem solar cells. *The Journal of Physical Chemistry Letters*, 7:746–751, 2016. DOI: https://doi.org/10.1021/acs.jpclett.6b00002.

[145] R. Ben Aich, I. Saïdi, S. Ben Radhia, K. Boujdaria, T. Barisien, L. Legrand, F. Bernardot, C. Testelin, B. Eble, and M. Chamarro. Bright-exciton splittings in inorganic cesium lead halide perovskite nanocrystals. *Physical Review Applied*, 11:034042, 2019. DOI: https://doi.org/10.1103/PhysRevApplied.11.034042.

[146] D. N. Dirin, I. Cherniukh, S. Yakunin, Y. Shynkarenko, and M. V. Kovalenko. Solution-grown $CsPbBr_3$ perovskite single crystals for photon detection. *Chemistry of Materials*, 28:8470–8474, 2016. DOI: https://doi.org/10.1021/acs.chemmater.6b04298.

[147] Y. Gao, Y. Wu, H. Lu, C. Chen, Y. Liu, X. Bai, Z. Li, H. Zhu, K. Wang, J. Bian, and S. Jin. $CsPbBr_3$ perovskite nanoparticles as additive for environmentally stable perovskite solar cells with 20.46% efficiency. *Nano Energy*, 59:517–526, 2019. DOI: https://doi.org/10.1016/j.nanoen.2019.02.075.

[148] Q. A. Akkerman, V. D'Innocenzo, S. Accornero, A. Scarpellini, A. Petrozza, M. Prato, and L. Manna. Tuning the optical properties of cesium lead halide perovskite nanocrystals by anion exchange reactions. *Journal of the American Chemical Society*, 137:10276–10281, 2015. DOI: https://doi.org/10.1021/jacs.5b05602.

[149] C. Dong, X. Han, W. Li, Q. Qiu, and J. Wang. Anti-solvent assisted multi-step deposition for efficient and stable carbon-based Cs PbI_2Br all-inorganic perovskite solar cell. *Nano Energy*, 59:553–559, 2019. DOI: https://doi.org/10.1016/j.nanoen.2019.02.075.

[150] Y. Rakita, N. Kedem, S. Gupta, A. Sadhanala, V. Kalchenko, M. L. Böhm, S. Rybak, D. Oron, R. H. Friend, D. Cahen, and G. Hodes. Low-temperature solution-grown $CsPbBr_3$ single crystals and their characterization. *Crystal Growth & Design*, 16:5717–5725, 2016. DOI: https://doi.org/10.1021/acs.cgd.6b00764.

[151] Z. Ahmad and A. Mishra. Growth of $PbBr_2$ microrods with unique structure and surface morphology. *Journal of Materials Science: Materials in Electronics*, 31:4672–4676, 2020. DOI: https://doi.org/10.1007/s10854-020-03019-0.

[152] A. Alberti, C. Bongiorno, E. Smecca, I. Deretzis, A. La Magna, and C. Spinella. Pb clustering and PbI_2 nanofragmentation during methylammonium lead iodide perovskite degradation. *Nature Communications*, 10:2196, 2019. DOI: https://doi.org/10.1038/s41467-019-09909-0.

[153] F. Palazon, Y. El Ajjouri, P. Sebastia-Luna, S. Lauciello, L. Manna, and H. J. Bolink. Mechanochemical synthesis of inorganic halide perovskites: Evolution of phase-purity, morphology, and photoluminescence. *Journal of Materials Chemistry C*, 7:11406–11410, 2019. DOI: https://doi.org/10.1039/C9TC03778K.

[154] H. Yu, G. Tian, W. Xu, S. Wang, H. Zhang, J. Niu, L. Zhang, J. Zhang, Y. Zhang, Y. Fan, J. Li, Y. Li, F. Meng, Z. Ma, J. Li, J. Zhang, Y. Zhao, Y. Liu, Z. An, and C. Wang. Green light-emitting devices based on perovskite $CsPbBr_3$ quantum dots. *Frontiers in Chemistry*, 6:381, 2018. DOI: https://doi.org/10.3389/fchem.2018.00381.

[155] P. Shukrynau, V. Dudr, M. Švec, M. Vondráček, P. Mutombo, T. Skála, V. Cháb, and J. Mašek. Core level photoemission and STM characterization of Ta/Si(111)-7×7 interfaces. *Surface Science*, 603:469–476, 2009. DOI: https://doi.org/10.1016/j.susc.2008.12.003.

[156] X. Sun, M. P. Felicissimo, P. Rudolf, and F. Silly. NaCl multi-layer islands grown on Au(111)-$(22 \times \sqrt{3})$ probed by scanning tunneling microscopy. *Nanotechnology*, 19:495307, 2008. DOI: https://doi.org/10.1088/0957-4484/19/49/495307.

[157] X. Liu, X. Tan, Z. Liu, H. Ye, B. Sun, T. Shi, Z. Tang, and G. Han. Boosting the efficiency of carbon-based planar $CsPbBr_3$ perovskite solar cells by a modified multistep

spin-coating technique and interface engineering. *Nano Energy*, 56:184–195, 2019. DOI: https://doi.org/10.1016/j.nanoen.2018.11.053.

[158] X. Zhang, H.-C. Wang, A.-C. Tang, S.-Y. Lin, H.-C. Tong, C.-Y. Chen, Y.-C. Lee, T.-L. Tsai, G.-R. Liu, J.-K. Wang, S.-M. Liu, W.-G. Diau, and R.-S. Liu. Robust and stable narrow-band green emitter: An option for advanced wide-color-gamut backlight display. *Chemistry of Materials*, 28:8493–8497, 2016. DOI: https://doi.org/10.1021/acs.chemmater.6b04107.

[159] S. Grimme. Semiempirical GGA-type density functional constructed with a long-range dispersion correction. *Journal of Computational Chemistry*, 27:1787–1799, 2006. DOI: https://doi.org/10.1002/jcc.20495.

[160] M. Becker and R. Berndt. Conductance of atom-sized Pb contacts. *New Journal of Physics*, 12:113010, 2010. DOI: https://doi.org/10.1088/1367-2630/12/11/113010.

[161] J. Tersoff and D. R. Hamann. Theory of the scanning tunneling microscope. *Physical Review B*, 31:805–813, 1985. DOI: https://doi.org/10.1103/PhysRevB.31.805.

[162] Q. A. Akkerman, S. G. Motti, A. R. Srimath Kandada, E. Mosconi, V. D'Innocenzo, G. Bertoni, S. Marras, B. A. Kamino, L. Miranda, F. De Angelis, A. Petrozza, M. Prato, and L. Manna. Solution synthesis approach to colloidal cesium lead halide perovskite nanoplatelets with monolayer-level thickness control. *Journal of the American Chemical Society*, 138:1010–1016, 2016. DOI: https://doi.org/10.1021/jacs.5b12124.

[163] Z.-G. Yu. Rashba effect and carrier mobility in hybrid organic–inorganic perovskites. *The Journal of Physical Chemistry Letters*, 7:3078–3083, 2016. DOI: https://doi.org/10.1021/acs.jpclett.6b01404.

[164] C. Stecker, K. Liu, J. Hieulle, R. Ohmann, Z. Liu, L. K. Ono, and Y. Qi. Surface defect dynamics in organic–inorganic hybrid perovskites: From mechanism to interfacial properties. *ACS Nano*, 13:12127–12136, 2019. DOI: https://doi.org/10.1021/acsnano.9b06585.

[165] F. Liu, Y. Zhang, C. Ding, S. Kobayashi, T. Izuishi, N. Nakazawa, T. Toyoda, T. Ohta, S. Hayase, M. Minemoto, K. Yoshino, and Q. Shen. Highly luminescent phase-stable $CsPbI_3$ perovskite quantum dots achieving near 100% absolute photoluminescence quantum yield. *ACS Nano*, 11:10373–10383, 2017. DOI: https://doi.org/10.1021/acsnano.7b05442.

[166] J. E. Ortega, G. Vasseur, I. Piquero-Zulaica, S. Matencio, M. A. Valbuena, J. E. Rault, M. G. Garnier, N. C. Plumb, M. Shi, M. Hoesch, W. Auwärter, and J. Lobo-Checa. Structure and electronic states of vicinal Ag(111) surfaces with densely kinked steps. *New Journal of Physics*, 20:073010, 2018. DOI: https://doi.org/10.1088/1367-2630/aacbb7.

[167] S. Y. Girgis and K. A. Mady. Electrical conductivity of vacuum-deposited lead bromide layers. *Journal of Materials Science Letters*, 5:1091–1094, 1986. DOI: https://doi.org/10.1007/BF01742208.

[168] M. M. Lee, J. Teuscher, T. Miyasaka, T. N. Murakami, and H. J. Snaith. Efficient hybrid solar cells based on meso-superstructured organometal halide perovskites. *Science*, 338:643–647, 2012. DOI: https://doi.org/10.1126/science.1228604.

[169] L. N. Quan, R. Quintero-Bermudez, O. Voznyy, G. Walters, A. Jain, J. Z. Fan, X. Zheng, Z. Yang, and E. H. Sargent. Highly emissive green perovskite nanocrystals in a solid state crystalline matrix. *Advanced Materials*, 29:1605945, 2017. DOI: https://doi.org/10.1002/adma.201605945.

[170] J. Deng, J. Li, Z. Yang, and M. Wang. All-inorganic lead halide perovskites: A promising choice for photovoltaics and detectors. *Journal of Materials Chemistry C*, 7:12415–12440, 2019. DOI: https://doi.org/10.1039/C9TC04164H.

[171] J. S. van der Burgt, J. J. Geuchies, B. van der Meer, H. Vanrompay, D. Zanaga, Y. Zhang, C. Delerue, D. Vanmaekelbergh, G. Van Tendeloo, A. J. Houtepen, and S. Bals. Cuboidal supraparticles self-assembled from cubic $CsPbBr_3$ perovskite nanocrystals. *The Journal of Physical Chemistry C*, 122:15706–15712, 2018. DOI: https://doi.org/10.1021/acs.jpcc.8b02699.

[172] D. Luo, X. Li, A. Dumont, H. Yu, and Z.-H. Lu. Recent progress on perovskite surfaces and interfaces in optoelectronic devices. *Advanced Materials*, 33:2006004, 2021. DOI: https://doi.org/10.1002/adma.202006004.

[173] S. Varshney, L. Chi, C. V. Singh, and J. Nogami. Atomic structure of $PbBr_2$ thin films on Ag (111). *Solid State Communications*, 343:114651, 2022. DOI: https://doi.org/10.1016/j.ssc.2022.114651.

[174] H. J. Jung, C. C. Stompus, M. G. Kanatzidis, and V. P. Dravid. Self-passivation of 2D Ruddlesden–Popper perovskite by polytypic surface PbI_2 encapsulation. *Nano Letters*, 19:6109–6117, 2019. DOI: https://doi.org/10.1021/acs.nanolett.9b02069.

[175] J. P. Perdew, K. Burke, and M. Ernzerhof. Perdew, Burke, and Ernzerhof reply. *Physical Review Letters*, 80:891, 1998. DOI: https://doi.org/10.1103/PhysRevLett.80.891.

[176] S. Ullah, J. Wang, P. Yang, L. Liu, S.-E. Yang, T. Xia, Y. Zou, D. Liu, W. Zhang, and C. Cao. All-inorganic $CsPbBr_3$ perovskite: A promising choice for photovoltaics. *Materials Advances*, 2:646–683, 2021. DOI: https://doi.org/10.1039/D0MA00866D.

[177] J. Feng, S. R. Wagner, and P. Zhang. Interfacial coupling and electronic structure of two-dimensional silicon grown on the Ag(111) surface at high temperature. *Scientific Reports*, 5:10310, 2015. DOI: https://doi.org/10.1038/srep10310.

[178] Z. Xiao, R. A. Kerner, L. Zhao, N. L. Tran, K. M. Lee, T.-W. Koh, G. D. Scholes, and B. P. Rand. Efficient perovskite light-emitting diodes featuring nanometre-sized crystallites. *Nature Photonics*, 11:108–115, 2017. DOI: https://doi.org/10.1038/nphoton.2016.269.

[179] G. Rainò, G. Nedelcu, L. Protesescu, M. I. Bodnarchuk, M. V. Kovalenko, R. F. Mahrt, and T. Stöferle. Single cesium lead halide perovskite nanocrystals at low temperature: Fast single-Photon emission, reduced blinking, and exciton fine structure. *ACS Nano*, 10:2485–2490, 2016. DOI: https://doi.org/10.1021/acsnano.5b07328.

[180] J. Song, J. Li, X. Li, L. Xu, Y. Dong, and H. Zeng. Quantum dot light-emitting diodes based on inorganic perovskite cesium lead halides ($CsPbX_3$). *Advanced Materials*, 27:7162–7167, 2015. DOI: https://doi.org/10.1002/adma.201502567.

[181] M. Zhang, Z. Zheng, Q. Fu, Z. Chen, J. He, S. Zhang, K. L. Woon, and S. F. Liu. Growth and characterization of all-inorganic lead halide perovskite semiconductor $CsPbBr_3$ single crystals. *CrystEngComm*, 19:6797–6803, 2017. DOI: https://doi.org/10.1039/C7CE01709J.

[182] G. Kresse and J. Furthmüller. Efficient iterative schemes for ab initio total-energy calculations using a plane-wave basis set. *Physical Review B*, 54:11169–11186, 1996. DOI: https://doi.org/10.1103/PhysRevB.54.11169.

[183] C. Nagl, E. Platzgummer, O. Haller, M. Schmid, and P. Varga. Surface alloying and superstructures of Pb on Cu(100). *Surface Science*, 331-333:831–837, 1995. DOI: https://doi.org/10.1016/0039-6028(95)00387-8.

[184] F. E. Olsson, M. Persson, J. Repp, and G. Meyer. Scanning tunneling microscopy and spectroscopy of NaCl overlayers on the stepped Cu(311) surface: Experimental and theoretical study. *Physical Review B*, 71:075419, 2005. DOI: https://doi.org/10.1103/PhysRevB.71.075419.

[185] K. Quertite, H. Enriquez, N. Trcera, Y. Tong, A. Bendounan, A. J. Mayne, G. Dujardin, and A. Ouerghi. Silicene nanoribbons on an insulating thin film. *Advanced Functional Materials*, 31:2007013, 2021. DOI: https://doi.org/10.1002/adfm.202007013.

[186] Q. Ren, L.-Y. Ding, F.-S. Chen, R.-P. Cheng, and D. Xu. The optical properties of lead bromide crystals. *Journal of Materials Science Letters*, 16:1247–1248, 1997. DOI: https://doi.org/10.1023/A:1018554303822.

[187] S. Masada, T. Yamada, H. Tahara, H. Hirori, M. Saruyama, T. Kawawaki, Y. Kanemitsu, and T. Teranishi. Effect of A-site cation on photoluminescence spectra of single lead bromide perovskite nanocrystals. *Nano Letters*, 20:4022–4028, 2020. DOI: https://doi.org/10.1021/acs.nanolett.0c01417.

[188] C. Liu, W. Li, J. Chen, J. Fan, Y. Mai, and R. E. I. Schropp. Ultra-thin MoOx as cathode buffer layer for the improvement of all-inorganic $CsPbIBr_2$ perovskite solar cells. *Nano Energy*, 41:75–83, 2017. DOI: https://doi.org/10.1016/j.nanoen.2017.08.048.

[189] C. A. López, C. Abia, M. C. Alvarez-Galván, B.-K. Hong, M. V. Martínez-Huerta, F. Serrano-Sánchez, J. A. Alonso, and J. L. G. Fierro. Crystal structure features of $CsPbBr_3$ perovskite prepared by mechanochemical synthesis. *ACS Omega*, 5:5931–5938, 2020. DOI: https://doi.org/10.1021/acsomega.9b04248.

[190] C. R. Ast, D. Pacilé, M. Papagno, T. Gloor, F. Mila, S. Fedrigo, K. Kern, J. H. Dil, and L. Patthey. Orbital selective overlayer-substrate hybridization in a Pb monolayer on Ag(111). *Physical Review B*, 73:245428, 2006. DOI: https://doi.org/10.1103/PhysRevB.73.245428.

[191] M. I. Saidaminov, A. L. Abdelhady, G. Maculan, and O. M. Bakr. Retrograde solubility of formamidinium and methylammonium lead halide perovskites enabling rapid single crystal growth. *Chemical Communications*, 51:17658–17661, 2015. DOI: https://doi.org/10.1039/C5CC06916E.

[192] U. Müller, D. Carnal, H. Siegenthaler, E. Schmidt, W. J. Lorenz, W. Obretenov, U. Schmidt, G. Staikov, and E. Budevski. Superstructures of Pb monolayers electrochemically deposited on Ag(111). *Physical Review B*, 46:12899–12901, 1992. DOI: https://doi.org/10.1103/physrevb.46.12899.

[193] D. Pacilé, C. R. Ast, M. Papagno, C. Da Silva, L. Moreschini, M. Falub, A. P. Seitsonen, and M. Grioni. Electronic structure of an ordered Pb/Ag(111) surface alloy: Theory and experiment. *Physical Review B*, 73:245429, 2006. DOI: https://doi.org/10.1103/PhysRevB.73.245429.

[194] Y. Hu, Q. Wang, Y.-L. Shi, M. Li, L. Zhang, Z.-K. Wang, L.-S. Liao, and J. Yao. Vacuum-evaporated all-inorganic cesium lead bromine perovskites for high-performance light-emitting diodes. *Journal of Materials Chemistry C*, 5:8144–8149, 2017. DOI: https://doi.org/10.1039/C7TC02477K.

Scientific Contributions

- Publications:
  - Madad Abbasli, Jeremy Hieulle, Jenny Schrage, Dina Wilks, Abdus Samad, Udo Schwingenschlögl, Alex Redinger, Carsten Busse, Robin Ohmann. "Tin Halide Perovskite Epitaxial Films on Gold Surfaces: Atomic Structure and Stability." *Advanced Functional Materials* (2024). `https://doi.org/10.1002/adfm.202403680`.
  - Robin Ohmann, Madad Abbasli, Jeremy Hieulle, Collin Stecker, Luis K. Ono, Carsten Busse, Yabing Qi. "Atomic and Electronic Structure of Lead Bromide on Metal Interfaces" (In preparation).
- Conference Talks:
  - "Mobility of electrons in a semiconductor quantum well with the modified Pöschl-Teller confining potential" - Conference at Baku State University, 2019.
  - "Mobility of electrons in a semiconductor quantum well with the modified Pöschl-Teller confining potential" - University of Siegen, November 28th, 2019.
  - "$CsSnBr_3$ on Gold Surfaces" - University of Luxembourg, 2021.
  - "Atomic structure determination of epitaxially grown tin perovskite $CsSnBr_3$ on gold surfaces" - DPG meeting, Regensburg, Germany, September 7th, 2022.
- Workshops and Poster Contributions:
  - Kickoff Workshop - SPP 2196 Perovskite semiconductors: From fundamental properties to devices, Potsdam, Germany, March 2020 [Participation].
  - Online Workshop March 2021 - SPP 2196 Perovskite semiconductors: From fundamental properties to devices [Poster].
  - "Epitaxially grown tin perovskite on gold surfaces" - 35th European Conference on Surface Science (ECOSS35), University of Luxembourg, 2022 [Contributed to the Talk as a coauthor].
  - On-surface fabrication of cesium tin halide nanostructures deviating from the perovskite ABX_3 Structure — Madad Abbasli, Dina Wilks, Carsten Busse, and Robin Ohmann —- DPG meeting, Regensburg 2025, Germany [coauthor] (submitted).

Eigenständigkeitserklärung

Hiermit erkläre ich, Madad Abbasli, dass ich die vorliegende Dissertation mit dem Titel *"Ultrathin Films of Tin Halide Perovskite on Gold Single Crystals"* selbstständig, ohne fremde Hilfe und in eigenen Worten niedergeschrieben habe. Ich versichere insbesondere, dass ich alle wörtlichen und sinngemäßen Übernahmen aus Quellen und anderen Ergebnissen als solche gekennzeichnet sowie vollständig aufgeführt habe.

Ort, Datum	Unterschrift